

UC San Diego

UC San Diego Electronic Theses and Dissertations

Title

AFM-based Enabling Nanotechnology for Membrane-Protein Interface and Their Application to Alzheimer's Disease.

Permalink

<https://escholarship.org/uc/item/9jp619nt>

Author

Lee, Joon

Publication Date

2017

Peer reviewed|Thesis/dissertation

UNIVERSITY OF CALIFORNIA, SAN DIEGO

**AFM-based Enabling Nanotechnology for Membrane-Protein Interface and Their
Application to Alzheimer's Disease.**

A Dissertation submitted in partial satisfaction of the
requirements for the degree
Doctor of Philosophy

in

Materials Science and Engineering

by

Joon Lee

Committee in charge:

Ratneshwar Lal, Chair
Bruce L. Kagan
Vlado A. Lubarda
Robert A. Rissman
Donald J. Sirbuly
Jerry Yang

2017

Copyright
Joon Lee, 2017
All rights reserved.

The Dissertation of Joon Lee is approved, and it is acceptable in quality and form for publication on microfilm and electronically:

Chair

University of California, San Diego

2017

DEDICATION

To all of my family members especially my wife and my grandmother..

EPIGRAPH

*Education must inspire the faith that
each of us has both the power and the responsibility
to effect positive change on a global scale.*

—Daisaku Ikeda

TABLE OF CONTENTS

Signature Page	iii
Dedication	iv
Epigraph	v
Table of Contents	vi
List of Figures	ix
List of Tables	xi
Acknowledgements	xii
Vita	xvi
Abstract of the Dissertation	xviii
Chapter 1 Introduction	1
1.1 What is Alzheimer’s disease?	1
1.2 Major hypothesis	2
1.3 Ion channel hypothesis	3
1.4 Other hypotheses	4
1.5 Production and molecular properties of Amyloid β	5
1.6 Atomic Force Microscopy	5
1.7 Black lipid membrane	8
1.8 Summary of dissertation	9
Chapter 2 Role of the Fast Kinetics of Pyroglutamate-Modified Amyloid- β Oligomers in Membrane Binding and Membrane Permeability	16
2.1 Abstract	16
2.2 Introduction	17
2.3 Materials and Methods	19
2.3.1 Peptide Handling	19
2.3.2 Thioflavin-T (ThT) Assays	20
2.3.3 Lipid Bilayer Preparation for AFM Imaging	20
2.3.4 AFM Imaging	21
2.3.5 AFM Force Mapping	23
2.3.6 Planar Lipid Bilayer Electrical Recording	23
2.4 Results	24
2.4.1 Kinetics of $A\beta_{pE3-42}$ Self-Assembly in Solution.	24
2.4.2 Membrane-Adsorbed $A\beta_{pE3-42}$ Oligomers	25

	2.4.3	Membrane-Inserted A β_{pE3-42} Oligomers.	26
	2.5	Discussion	28
	2.6	Conclusion	32
	2.7	Acknowledgements	33
Chapter 3		Amyloid β ion channels in a membrane comprising of brain total lipid extracts	41
	3.1	Abstract	41
	3.2	Introduction	42
	3.3	Results and Discussion	45
	3.3.1	Interaction with BTLE or DOPS/POPE liposomes facili- tate the self-assembly behavior of A β	45
	3.3.2	Distribution of A β_{1-42} oligomer structures on DOPS/POPE and BTLE membranes	47
	3.3.3	Pore structures of A β_{1-42} in BTLE and DOPS/POPE membranes	48
	3.3.4	Ion Conducting Activity of A β_{1-42} in DOPS/POPE and BTLE membranes	50
	3.4	Conclusions	56
	3.5	Materials and Methods	57
	3.5.1	Peptide preparation	57
	3.5.2	Thioflavin T Assays	57
	3.5.3	Proteoliposome preparation for AFM imaging	58
	3.5.4	Formation of Planar Lipid Bilayers for BLM experiments	59
	3.5.5	BLM Measurements of A β s	59
	3.6	Acknowledgements	61
Chapter 4		The diphenylpyrazol compound anle138b blocks A β channels and rescues disease phenotypes in a mouse model for amyloid pathology	70
	4.1	Abstract	70
	4.2	Introduction	71
	4.3	Results	72
	4.3.1	Synaptic plasticity and memory function in a mouse model for deposition of amyloid β after oral treatment with anle138b	72
	4.3.2	Anle138b reinstate transcriptional homeostasis and ame- liorates amyloid pathology	75
	4.3.3	Biophysical characterization of A β in the presence of anle138b	77
	4.3.4	Discussion	78
	4.3.5	Conclusion	81
	4.4	Materials and Methods	82
	4.4.1	Mouse Experiments	82
	4.4.2	Electrophysiology on hippocampal slices	84

	4.4.3	Biophysical characterization on $A\beta_{1-42}$	86
	4.4.4	Cell Membrane Integrity and viability	89
	4.5	Acknowledgements	90
Chapter 5		Nanofiber optic force transducers with sub-piconewton resolution via near-field plasmon-dielectric interactions.	97
	5.1	Abstract	97
	5.2	Introduction	98
	5.3	Results	99
	5.4	Conclusion	102
	5.5	Methods	103
	5.5.1	Integrated AFM/Optical Setup	103
	5.5.2	Optical setup for the measurement of bacteria motion force	103
	5.5.3	Optical setup for the measurement of cell beating frequency	104
	5.5.4	Tin dioxide (SnO_2) nanofiber chip preparation	104
	5.5.5	Alexander-de Gennes force model	105
	5.5.6	Preparation of <i>H. pylori</i> bacteria	106
	5.5.7	Statistical analysis of scattering intensity	107
	5.5.8	Number of bacteria (N) directly interacting with nanopar- ticle per second	107
	5.5.9	Force detection with a free-standing AFM cantilever	108
	5.5.10	Average stress applied on NP_{sensor} and AFM cantilever	108
	5.5.11	Sound pressure level estimation using an oscillating AFM tip	109
	5.5.12	Cardiomyocytes sample preparation Gelatin	109
	5.6	Acknowledgements	111
Bibliography		121

LIST OF FIGURES

Figure 1.1:	Percentage changes in selected causes of death (all ages) between 2000 and 2010.	11
Figure 1.2:	Production and molecular properties of Amyloid β	12
Figure 1.3:	Lennard-Jones potential curve.	13
Figure 1.4:	Schematics of atomic force microscopy.	14
Figure 1.5:	Schematics of black lipid membrane setup.	15
Figure 2.1:	Self-assembly kinetics of $A\beta_{1-42}$ and $A\beta_{pE3-42}$ measured by thioflavin-T (ThT) fluorescence at 25 °C	34
Figure 2.2:	AFM images of (A) $A\beta_{pE3-42}$ and (B) $A\beta_{1-42}$ aggregated peptides after different periods of incubation	35
Figure 2.3:	AFM height and amplitude images of $A\beta_{pE3-42}$ fibrils formed on supported DOPS/POPE (1:1) lipid membrane after incubation for 38 hours at room temperature.	36
Figure 2.4:	AFM images of $A\beta_{pE3-42}$ and $A\beta_{1-42}$ oligomers and membrane defects induced by the oligomers in a DOPS/POPE (1:1) lipid bilayer.	36
Figure 2.5:	Diameter and height histograms of inserted and adsorbed oligomers	37
Figure 2.6:	AFM image of $A\beta_{pE3-42}$ oligomers inserted in a DOPS/POPE (1:1) membrane and electrical recording data demonstrating the activity induced by $A\beta_{pE3-42}$ pore-forming oligomers.	38
Figure 2.7:	AFM force measurements demonstrating the effect of membrane-inserted $A\beta_{pE3-42}$ oligomers on the mechanical properties of DOPS/POPE membranes	39
Figure 2.8:	Schematics of supported membrane (SM) formation via proteoliposome (PL) rupture and fusion	40
Figure 3.1:	Self-assembly of $A\beta_{1-42}$ in the presence of BTLE and DOPS/POPE (1:1, wt/wt) liposomes monitored by ThT fluorescence.	62
Figure 3.2:	AFM images of reconstituted $A\beta_{1-42}$ oligomers in BTLE or DOPS/POPE supported lipid membranes on mica.	63
Figure 3.3:	$A\beta_{1-42}$ channel structures embedded in the DOPS/POPE lipid bilayer and the BTLE bilayer.	64
Figure 3.4:	Representative electrical recordings of $A\beta_{1-42}$ in BTLE and DOPS/POPE (1:1, wt/wt) membranes.	65
Figure 3.5:	Histograms of frequency vs. conductance of ion current fluctuations of $A\beta_{1-42}$	66
Figure 3.6:	Quantification of ion influx through $A\beta_{1-42}$ and p3 using the total transported charge	67
Figure 3.7:	Representative electrical recordings of p3 in BTLE and DOPS/POPE (1:1, wt/wt) membranes.	68
Figure 3.8:	Representative current vs. time traces of $A\beta_{1-42}$ in a DOPS/DOPE (1:1, wt/wt) membrane.	69

Figure 4.1:	Anle138b rescues hippocampal LTP deficits spatial memory in the pre-plaque group.	91
Figure 4.2:	Anle138b rescues hippocampal LTP deficits spatial memory in the post-plaque group.	92
Figure 4.3:	Hippocampal gene-expression in anle138b treated mice.	93
Figure 4.4:	Amyloid plaque pathology is ameliorated by anle138b treatment in the pre-plaque (A) and post-plaque (B) groups.	94
Figure 4.5:	Anle138b ameliorates A β ₁₋₄₂ induced membrane integrity.	95
Figure 4.6:	Observation of A β pores by AFM in anle138b-doped membranes.	96
Figure 5.1:	Nanofiber optic force transducer calibration.	113
Figure 5.2:	Force detection from bacteria motion	114
Figure 5.3:	Acoustic frequency detection	115
Figure 5.4:	Force curves of a PEG monolayer in PBS buffer grown on a silicon substrate. The mechanical stability of the PEG monolayer tracked over two weeks.	116
Figure 5.5:	A force mapping image of a nanofiber with NP _{sensor} linked on top of a PEG monolayer and a time-course of the optical scattering intensity during the force mapping.	116
Figure 5.6:	Optical image of a bare AFM tip (red outline) indenting on a SnO ₂ nanofiber and the scattering intensity of a NP _{sensor} on the nanofiber and the AFM tip region during indentation.	117
Figure 5.7:	Scattering intensities of two NP _{sensor} (black and blue traces) measured simultaneous while a nanoparticle-modified AFM tip (red trace) is indented onto a nanofiber waveguide.	117
Figure 5.8:	Representative force curve of a PEG film using a gold nanoparticle attached to an AFM tip.	118
Figure 5.9:	Dark-field optical image of a NOFT suspended across a trench.	118
Figure 5.10:	Relationship between the coefficient of variation (σ/μ) and the average intensity (μ) in PBS for the dead bacteria.	119
Figure 5.11:	Representative force curve of a PEG film on the WG using an AFM tip at a frequency of 2 Hz.	119
Figure 5.12:	Scattering image of NP _{sensor} and end facet when AFM is running force mapping indentation.	120
Figure 5.13:	Fourier transforms taken from the end facet of the NOFT with the cardiomyocyte cluster after \sim 30 minutes at room temperature.	120

LIST OF TABLES

Table 2.1:	Heights (h), Widths (W), and Diameters (D) for the globular and annular oligomers of $A\beta_{1-42}$ and $A\beta_{pE3-42}$ shown in Figure 2.2 at the indicated times ($n = 28$ for all entries) ^a	34
Table 2.2:	Density, n_O , of membrane-associated oligomers (inserted and adsorbed) as well as measured widths, diameters and heights of inserted, W_I, D_I, h_I , and adsorbed, W_A, D_A, h_A of $A\beta_{1-42}$ and $A\beta_{pE3-42}$ oligomers, respectively.	35
Table 2.3:	Comparison of pore diameters for $A\beta_{pE3-42}$, $A\beta_{1-42}$ and $A\beta_{17-42}$ obtained from eq. 3.3, MD simulations and AFM.	38
Table 3.1:	Composition of brain total lipid extract provided by Avanti Polar Lipids.	62

ACKNOWLEDGEMENTS

First and foremost, I would like to thank my advisor, Professor Ratnesh Lal. I appreciate all his contributions of time, ideas, and funding to make my Ph.D. experience productive. Ratnesh has given me the freedom to pursue various projects without objection and connected me with various researchers in the world. His selfless time and care were sometimes all that kept me going even during tough times in the Ph.D. pursuit.

I would like to thank all of my dissertation committee members: Professors Bruce L. Kagan, Vlado A. Lubarda, Robert A. Rissman, Donald J. Sirbuly, Jerry Yang for providing valuable insight to this dissertation. Particularly, I would like to thank Professor Yang from the Department of Chemistry at UCSD for his comments on scientific writing as well as career advice, Professor Sirbuly from the Department of the Nanoengineering at UCSD for being supportive and patient during our long collaboration for nanofiber optic force transducer project, and Professor Kagan from the Department of Psychiatry at UCLA for giving valuable research advice on amyloid projects. I would like to thank Professor Lubarda for teaching me thermodynamics and greeting me whenever we saw each other at the coffee shops.

The members of the Lal lab have contributed enormously to my personal and professional time at UCSD. Dr. Fernando Arce and Dr. Srinu Ramachandran have showed me a great mentorship and trained me how to conduct research projects and experiments in detail. I am thankful to my lab mates, Dr. Alan Gillman, Dr. Brian Meckes, Dr. Jeanie Meckes, Dr. and Alexander Mo, who were the first generation of the Lal lab at UCSD for sharing my Ph.D. journey with me. I really enjoyed the time we spent together in the lab as well as outside of the lab talking about all the fun things and creative research idea. I am grateful for Michael Hwang who is graduating with me. We worked together on DNA

projects and I appreciated his enthusiasm on his work. I would like to acknowledge other past and present group members that I have had the pleasure to work with or alongside of: Dr. Karla Santacruz Gomez, Dr. Preston Landon, Nirav Petel, Qingqing Yang, Juan Yberra, Yushuang Liu, Vrinda Sant, Dr. Dependra Kumar Ban, Prof. Rongzhang Hao, Grace Jang, Abhijith Karkisaval, Nathan Khosla, Jay Sheth, Alice Yepremyan, Prof. Feng Zhang, Prof. Liping Wang, and Leif Antonschmidt. I will miss hanging out with them and all the Chinese, Mexican, and Korean food that we had together. I would like to thank Dr. Jessica Cifelli (and Christian) and Dr. Kevin Cao from the Yang group for being my friends, giving me valuable advice on amyloid projects and taking care of Young.

I would like to thank Dr. Hyunbum Jang and Dr. Ruth Nussinov from the National Cancer Institute at Frederick for performing all atom molecular dynamics simulation on the amyloid β pore structures in lipid membranes discussed in this dissertation as well as for their comments on amyloid projects.

I would like to also thank Dr. Christian Greisinger from Max Planck Institute for Biophysical Chemistry. Christian showed me how to be a pleasant scientist with a sense of humor during our skype meeting. The study of amyloid beta protein with anle138b compound discussed in this dissertation would not have been done without his leadership and collaboration with many other groups.

The nanofiber optic force transducer work discussed in this dissertation would not have been possible without patient and faithful collaborator, Dr. Qian Huang from Sirbulu group. Qian always wanted to be clear with everything so at times I got too many questions. I learned a lot from her well organized experiment plans. I will miss all the days that we spent all day in the dark room of the basement without knowing how many hours had passed as well as all the late night food we shared together. I also thankful for Dr. Ilsun Yoon who

initially helped me and Qian for conducting this project. I appreciate the help from Yuesong Shi for conducting the experiments for the revision of the NOFT paper after Qian left.

I gratefully acknowledge the Frontiers of Innovation Scholars Program, UCSD for funding me one year and the National Health Institute for supporting my research. I would like to thank my amazing lab manager of the classes that I have involved as a TA for five years, Nick Busan. Nick taught me how to manage the class and how to be neat and organized. I appreciate his valuable life advice as well as career advice. I will miss those funny jokes during his introduction in the lab. I would like to also thank Greg Specht for supporting all TA/readers and making the atmosphere delightful. I really enjoyed interacting with students in the class and being a head TA of the class. I am thankful to have a TA like Rahul (who was the previous head TA of MAE170 before me), Gilbert, Raj, Jeff, Rich, Keyur, Fatih, Ajay, Maria, Brandon, Roger, Tiantian and Carson for their awesome work.

Lastly, I would like to thank my family for all their love and encouragement. I would like to thank my parents who always believed in me no matter what I did. I cannot thank more for their support. Also, I would like to thank my grandmother who gave me a big smile whenever I saw her through video calls even though she has been fighting with her disease for so many years. I am thankful to my brother, Hun, who always chanted for me. I greatly thankful to my mother in law for her tremendous belief in me and Young throughout the journey. I am grateful to my brother in law who is taking care of my mother in law. I would like to thank my loving, encouraging, and patient wife, Young Hun who supported me faithfully the whole time during my Ph.D. years. She was always there for me as my lovely wife, my collaborator, and my best friend. Her contribution on studying amyloid beta protein in a membrane comprising brain total lipid extracts discussed in this dissertation greatly improved our knowledge of understanding the characteristics of the protein. She

definitely made my journey to Ph.D. so much happy and enjoyable.

Chapter 2, in part, is a reprint of the material as it appears in Lee, J.; Gillman, A. L.; Jang, H.; Ramachandran, S.; Kagan, B. L.; Nussinov, R.; Teran Arce, F. Role of the Fast Kinetics of Pyroglutamate-Modified Amyloid- β Oligomers in Membrane Binding and Membrane Permeability. *Biochemistry* **2014**, *53*, 4704–4714. The dissertation author was the primary author of this paper.

Chapter 3, in part, is a reprint of the material as it appears in Lee, J.; Kim, Y. H.; T. Arce, F.; Gillman, A. L.; Jang, H.; Kagan, B. L.; Nussinov, R.; Yang, J.; Lal, R. Amyloid Ion Channels in a Membrane Comprising Brain Total Lipid Extracts. *ACS Chem. Neurosci.* **2017**, acschemneuro.7b00006. The dissertation author was the primary author of this paper.

Chapter 4, in part, has been submitted for publication of the material as it may appear in Hernandez Martinez, A., Urbanke, H., Gillman, A.L., Lee, J., Ryazanov, S., Agbemenyah, H.Y., Li, Q., Rezaei-Ghaleh, N., Wilken P., Bartels, C., Leonov, A, Leonov, A., Lal, R., Benz, R., Zweckstetter, M., Giese A., Schneider A., Korete, M., Griesinger, C., Arce, FT., Eichele, G., Fischer, A. The diphenylpyrazol compound anle138b blocks A β channels and rescues disease phenotypes in a mouse model for amyloid pathology. 2017 (*under revision*). The dissertation author was the primary author of this paper.

Chapter 5, in part, is a reprint of the material as it appears in Lee, J.*, Huang, Q.*; Arce FT.*; Yoon, I.; Angsantikul, P.; Liu, J.; Shi, Y.; Villanueva, J.; Thamphiwatana, S.; Ma, X.; Zhang, L.; Chen, S.; Lal, R.; Sirbuluy, DJ. Nanofibre optic force transducers with sub-piconewton resolution via near-field plasmon-dielectric interactions. *Nature Photonics* **2017** doi:10.1038/nphoton.2017.74 The dissertation author was the primary author of this paper.

VITA

- 2009 B. S. in Chemistry, Yonsei University, Seoul, Korea
- 2011 M. S. in Chemistry, Yonsei University, Seoul, Korea
- 2012-2017 Teaching Assistant, Department of Mechanical Engineering
University of California, San Diego
- 2017 Ph. D. in Materials Science and Engineering Program, University of
California, San Diego

PUBLICATIONS

Hernandez Martinez, A., Urbanke, H., Gillman, A.L., **Lee, J.**, Ryazanov, S., Agbemenyah, H.Y., Li, Q., Rezaei-Ghaleh, N., Wilken P., Bartels, C., Leonov, A., Leonov, A., Lal, R., Benz, R., Zweckstetter, M., Giese A., Schneider A., Korete, M., Griesinger, C., Arce, FT., Eichele, G., Fischer, A. The diphenylpyrazol compound anle138b blocks A β channels and rescues disease phenotypes in a mouse model for amyloid pathology. 2017 (*under revision*)

Li, N., Jang, H., Yuan, M., Li, W., Yun, X., **Lee, J.**, Du, Q., Nussinov, R., Hou, J., Lal R., Zhang, F. Graphite-Templated Amyloid Nanostructures Formed by A Potential Pentapeptide Inhibitor for Alzheimers disease: A Combined Study of Real-Time Atomic Force Microscopy and Molecular Dynamics Simulations. *Langmuir* 2017, doi: 10.1021/acs.langmuir.7b00414

Liu, M.* , Li, Q.* , Liang, L., Li, J., Wang, K., Li, J., Lv, M., Chen, N., Song, H., **Lee, J.**, Shi, J., Wang, L., Lal, R., Fan, C. Real-time visualization of clustering and intracellular transport of gold nanoparticles by correlative imaging. *Nature Communication* 2017, doi:10.1038/ncomms15646

Huang, Q.* , **Lee, J.*** , Arce FT.* , Yoon, I., Angsantikul, P., Liu, J., Shi, Y., Villanueva, J., Thamphiwatana, S., Ma, X., Zhang, L., Chen, S., Lal, R., Sirbuly, DJ. Nanofibre optic force transducers with sub-piconewton resolution via near-field plasmon-dielectric interactions. *empfNature Photonics* 2017, doi:10.1038/nphoton.2017.74

Lee, J.* , Kim, Y. H.* , T. Arce, F.* , Gillman, A. L., Jang, H., Kagan, B. L., Nussinov, R., Yang, J., Lal, R. Amyloid Ion Channels in a Membrane Comprising Brain Total Lipid Extracts. *ACS Chem. Neurosci.* 2017, acschemneuro.7b00006.

Huang, Q., Arce, F., **Lee, J.**, Yoon, I., Villanueva, J., Lal, R., Sirbuly, DJ. Gap controlled plasmon-dielectric coupling effects investigated with single nanoparticle-terminated atomic force microscope probes. *Nanoscale* 2016, 8, 17102.

Gillman, A.L., **Lee, J.**, Ramachandran, S., Capone, R., Gonzalez, T., Wolf, W., Masliah, E., and Lal, R. Small Molecule NPT-440-1 Inhibits Ionic Flux through A β ₁₋₄₂ Pores: Potential Role of β -Sheet Content Modulation for Alzheimers Disease Therapeutics. *Nanomedicine Nanotechnology, Biol. Med.* 2016 12, 2331-2340

Hwang, M. T.* , Landon, P. B.* , **Lee, J.**, Choi, D., Mo, A. H., Glinsky, G., Lal, R. Highly Specific SNP Detection Using 2D Graphene Electronics and DNA Strand Displacement. *Proc. Natl. Acad. Sci.* 2016, 113, 7088.

Jang, H., Arce, F.T., **Lee, J.**, Gillman, A.L., Ramachandran, S., Kagan, B.L., Lal, R., and Nussinov, R. Computational Methods for Structural and Functional Studies of Alzheimer's Amyloid Ion Channels. In *Protein Amyloid Aggregation: Methods and Protocols*, Eliezer, D., Ed., Springer New York: New York, NY, 2016, pp. 251-268.

Mo, A. H.* , Landon, P.* , Santacruz Gomez*, K., Kang, H., **Lee, J.**, Zhang, C., Janetanakit, W., Sant, V., Lu, T., Colburn, D. A., Akkiraju, S., Dossou, S., Cao, Y., Lee, K., Varghese, S., Glinsky, G., Lal, R. Magnetically-Responsive Silica-Gold Nanobowls for Targeted Delivery and SERS-Based Sensing. *Nanoscale* 2016, 8, 11840.

Hwang, M. T., Landon, P. B., **Lee, J.**, Mo, A., Meckes, B., Glinsky, G., and Lal, R. DNA Nano-Carrier for Repeatable Capture and Release of Biomolecules. *Nanoscale* 2015 7, 17397-17403

Landon, P.B.* , **Lee, J.***, Hwang, M.T., Mo, A.H., Zhang, C., Neuberger, A., Meckes, B., Gutierrez, J.J., Glinsky, G., and Lal, R. Energetically Biased DNA Motor Containing a Thermodynamically Stable Partial Strand Displacement State. *Langmuir* 2014 30 (1), 14073-14078

Lee, J., Gillman, A.L., Jang, H., Ramachandran, S., Kagan, B.L., Nussinov, R., and Arce, F.T. Role of the Fast Kinetics of Pyroglutamate-Modified Amyloid- β Oligomers in Membrane Binding and Membrane Permeability. *Biochemistry* 2014 53 (28), 4704-4714

Gillman, A.L.* , Jang, H.* , **Lee, J.**, Ramachandran, S., Kagan, B.L., Nussinov, R., and Arce, FT. Activity and Architecture of Pyroglutamate-Modified Amyloid- β (A β _{pE3-42}) Pores. *J. Phys. Chem. B* 2014 118 (26), 7335-7344

* Denotes equal authorship

ABSTRACT OF THE DISSERTATION

AFM-based Enabling Nanotechnology for Membrane-Protein Interface and Their Application to Alzheimer's Disease.

by

Joon Lee

Doctor of Philosophy in Materials Science and Engineering

University of California, San Diego, 2017

Ratneshwar Lal, Chair

Alzheimer's disease (AD) is the most common type of dementia affecting more than 44 million patients worldwide. AD accounts for 60 to 80 percent of dementia cases. AD is characterized by the progressive loss of memory and cognition. The pathological hallmark of AD is the deposition of fibrillar amyloid plaques in the brains of AD patients. Amyloid beta ($A\beta$) proteins, the major constituents of these plaques, are derived by enzymatic cleavage from the transmembrane amyloid precursor protein (APP). Although accumulation of $A\beta$ plaques in AD brains was believed to be directly correlated to the disease, increasing evidence indicates that small $A\beta$ oligomers are the main toxic species. However, the

exact disease mechanism has not yet been fully elucidated. A prevailing mechanism of AD pathology postulates that A β oligomers negatively affect neuronal function and survival by forming ion permeable pores, resulting in the destabilization of cell ionic homeostasis. This dissertation investigates the structures and ion conducting properties of A β oligomers in lipid membranes as well as develops new techniques that can be applied to elucidate the mechanism of unknown disease pathologies. In chapter 2, I present the biophysical characterizations of two most abundant A β proteins (A β_{1-42} and A β_{pE3-42}) in lipid membranes using AFM and Black Lipid Membrane (BLM) techniques to give insight toward finding the disease mechanisms. In chapter 3, I show the structures and ion conducting properties of A β_{1-42} and A β_{17-42} (or p3) in membranes comprised of natural brain total lipid extract and compare the results from other model lipid membranes. In chapter 4, I show the effect of an AD therapeutic candidate molecule on A β structures and ion conducting activities. In chapter 5, I show the development of new technique called Nanofiber optical force transducer. This new technique can measure sub pN force from living organisms. This multiscale study of structure-function relationship in A β proteins provides insight into AD mechanism and specific targets for the development of therapeutic strategies for the treatment AD.

Chapter 1

Introduction

1.1 What is Alzheimer's disease?

Alzheimer's disease (AD) is the most common type of dementia and it is found primarily in elderly individuals over 65 years of age. AD is a devastating neurodegenerative disease with a progression that develops over a long course of time prior to the emergence of obvious clinical symptoms. The most commonly associated symptoms of AD are difficulty in remembering things and cognitive impairment. Clinically, AD is diagnosed by progressive cognitive and memory deficit which results from fewer synapses and neurons, as well as a decrease in brain volume.[1] In addition, two types of plaques are found in postmortem autopsy of AD brains: amyloid plaques and neurofibrillary tangles. Identification of these plaques in the brain was first reported by Dr. Alois Alzheimer in 1901. Later the main constituents of the amyloid plaques and neurofibrillary tangles were found to be amyloid beta ($A\beta$) proteins and tau proteins, respectively.[2, 3]

AD is ranked as the sixth leading cause of death in United States and, as of 2013, one of top 5 leading cause of death in many countries around the world.[4] An estimated 5.3

million Americans suffer from AD and more than 96% of them are older than 65 years. In contrast to nearly all other major causes of death in the United States, the prevalence of AD continues to rise at an alarming rate. Between 2000 and 2010 (Figure 1.1), deaths resulting from heart disease, stroke and prostate cancer decreased 14%, 23%, and 11% respectively, while deaths from AD increased 71%. [5] Since age is the single greatest risk factor for AD, and human life span continues to extend with advances in modern medicine, this type of disease is expected to become even more prevalent. Recent estimates predict that AD will soon be the third leading cause of death for older people, following heart disease and cancer. By 2050, the number of AD patients is projected to grow nearly 10 million. [5]

The social impact of AD, as well as economic burden to society, are also significant. In 2015, more than 15 million family members and unpaid caregivers provided an estimated 18.1 billion hours of care to people with AD and other dementias, a contribution valued at more than \$221 billion. [5]

1.2 Major hypothesis

Numerous research groups and pharmaceutical companies have tried to elucidate the cause of AD pathology, yet there is no clear understanding of the ultimate cause of AD. The exact identity of the toxic species and the mechanisms by which they act remain unsolved. Over time, two major hypotheses have emerged to explain the AD mechanism: the amyloid hypothesis and the tau hypothesis.

The amyloid hypothesis states that the deposition of A β amyloid in the brain causes a cascade of harmful events that lead to progressive symptoms of AD. [6, 7] It was originally believed that amyloid plaques cause the disease by damaging neurons and blocking synapse signaling between neurons. Many studies focused on the amyloid plaques as a main toxic

component and specifically on the toxicity of amyloid fibrils. However, amyloid plaques do not always correlate in number, or spatial distribution with neurodegeneration or clinical dementia.[8] For example, amyloid plaques are often found at a distance from sites of neuron loss. Cognitively normal individuals, with no symptom of AD, have also shown deposition of amyloid plaques in postmortem analysis.

The amyloid plaques are mainly composed of A β proteins has 40-42 amino acids and high propensity for self-aggregation. Small A β oligomers are formed during the initial stages of the aggregation process. These small oligomers further aggregate to form fibrils, and eventually amyloid plaques. The small oligomers were found to cause synaptic loss in neuronal cells.[9] Over the years a multitude of evidence has suggested that amyloid plaques or amyloid fibrils are not the main toxic constituent but it is the small A β oligomers that are most toxic to neurons.[9, 10, 11]

In contrast to the amyloid hypothesis, the tau hypothesis states that tau protein is the primary cause of AD instead of A β protein.[12] Tau protein is mainly located in the axonal compartment of neurons and is known to stabilize microtubule structures. By a still unknown trigger and mechanism, tau proteins become hyper-phosphorylated. When the tau protein is phosphorylated, the protein detaches from the microtubule and starts to aggregate resulting in the neurofibrillary tangles.[13] These tangles then cause the neurodysfunction.

1.3 Ion channel hypothesis

The ion channel hypothesis builds upon the central premise of the amyloid hypothesis and states that A β oligomers form ion channels in neuronal membranes which disturb the ionic homeostasis in neurons. Loss of ionic balance leads to neurotoxicity and results in AD. Although it is not clear how A β protein induces neuronal loss and tangle formation,

the protein is known to disrupt calcium homeostasis and increase intraneuronal calcium concentrations.[7] Arispe *et al.* reported that A β proteins form cation-selective ion channels in black lipid membranes (BLM) in electrophysiological studies in 1993.[14] Unlike conventional ion channel proteins, A β ion channels show heterogeneous ion conducting activities in BLM with multiple conductance levels. It was also reported that A β induces ion flux in cellular membranes including liposomes, neurons, oocytes, and endothelial cells.[15] This ion conducting activity could be blocked by Zn²⁺ and Congo red.[16] These reports support the hypothesis that A β forms ion channels in biological membranes. In addition to the electrophysiology data, pore-like structures of A β oligomers were seen by using atomic force microscopy (AFM) and electron microscopy (EM). The first AFM study reported channel-like structures of A β oligomers consist of tetra to hexameric subunits with outer diameter of 8-12 nm in Asolection lipid membranes.[17] EM images of A β oligomers isolated from AD patients show annular structures of A β oligomers with variable diameters of 6-9 nm in outer diameter.[18] Molecular dynamic (MD) simulation also supports the formation of A β ion channels. Jang *et al.* demonstrated the stable A β pores consisting β -barrel structures in lipid membranes. The studies show that the pore structure contains 16 to 24 A β monomers and the dimensions are in good agreement with experimental results.[19, 20, 21]

1.4 Other hypotheses

Besides all the hypotheses mentioned above, many other mechanisms explaining the toxic behavior of A β proteins in neuronal cell membranes have been proposed. One of them is that A β proteins disrupt cell membrane by thinning the membrane and induce non-specific leakage of ions rather than formation of A β ion channels.[22] The study pointed out that the area compressibility of the lipid has a large effect in planar lipid membrane experiments

and showed that membranes formed by using decane as solvent didn't show leakage current. Other researchers proposed that A β protein induces reactive oxidative stress in neurons and results in cytoskeleton disruption.[23]

1.5 Production and molecular properties of Amyloid β

A β protein consists of up to 42 amino acid residues and is produced by sequential cleavage of a transmembrane protein called amyloid precursor protein (APP) by multiple enzymes. (Figure 2) In the amyloidogenic pathway, A $\beta_{1-40/42}$ protein is produced via cleavage of APP by β - and γ - secretases. In the nonamyloidogenic pathway, other enzymes such as β' - or α - secretase in combination with γ -secretase produce shorter A β peptides, A $\beta_{11-40/42}$ or A $\beta_{17-40/42}$. [24] As shown in Figure 2, the charged amino acid residues are mostly located near the N terminal region whereas the hydrophobic amino acid residues are located in the C terminal region. For example, A β_{1-42} has 6 negatively charged residues, 6 positively charged residues, and 20 hydrophobic residues.[25] Due to this unique sequence, A β monomers tend to self-assemble and aggregate with each other to form fibrillar structures.

1.6 Atomic Force Microscopy

Atomic force microscopy (AFM) is one of the most versatile and powerful microscopy technologies for studying samples at nanoscale. AFM can image three dimensional topography with sub-nanometer height information as well as measure functionality of various samples. AFM is especially useful for studying biosamples in physiological conditions. AFM was invented by Gerd Binnig, a German physicist, shortly after he was awarded the 1986 Nobel Prize in Physics for the design of the scanning tunneling microscope (STM).[26]

AFM is a type of scanning probe microscopy (SPM) that raster scans a sample using a sharp tip located on the end of the cantilever. One analogy of AFM scanning would be touching a sample using a fingertip. The radius of an AFM tip can be as small as 1 nm. AFM cantilevers are typically made of flexible silicon nitride with spring constant as low as 0.01 N/m. AFM makes use of the interaction force between a tip and a sample. When the AFM tip is approaching a sample surface, attraction forces appear due to the long range Van der Waals force. When the distance between the tip and the sample surface become very close, repulsive force starts to dominate. This interaction potential can be simply described by the Lennard-Jones potential which includes both attractive and repulsive forces (Figure 3). Depending on the interaction forces, AFM cantilever experiences deflection. This deflection can be monitored by using a laser beam that reflects from the cantilever to a quadruple photodetector (Figure 4). Thus by using a Hooke's law, $F = -k \cdot x$, force can be calculated where F is the applied force, k is the spring constant of the cantilever, and x is the deflection of the cantilever in distance. During AFM imaging, the deflection of the cantilever, and thus the force between a tip and a sample, is maintained constant. The deflection of the cantilever due to the changes in either force or height is measured by monitoring the position of the laser light in the quadruple detector and further goes through a feedback loop to adjust the force or height. The first AFM showed a lateral resolution of 30 Å and a vertical resolution less than 1 Å.[26]

There are many advantages of AFM when compared with other imaging techniques. A significant advantage of AFM over optical microscopy techniques is its high spatial resolution that is not limited by the diffraction limit of the wavelength of light. The diffraction limit (d) can be simply calculated by the equation, $d = \lambda / 2 \cdot n \cdot \sin\theta$ where λ is the wavelength of light, n is the refractive index of the medium and θ is the half angle of the

two discernible spots. When using 500 nm visible light (typically ranges from 400 ~ 700 nm), the diffraction limit is ~ 250 nm. This means that the light cannot resolve a sample smaller than 250 nm. However, it should be noted that recent emergence of super resolution microscopy greatly improved the spatial resolution beyond the diffraction limit. Unlike optical microscopy techniques, AFM uses a physical interaction between a tip and a sample. The spatial resolution of AFM is typically in the ~ 1 nanometer range, easily exceeding the diffraction limit.[27]

Another great advantage of AFM is that there is no sample preparation requirement. For instance, electron microscopy requires conductive coating unless the sample itself is conductive. Fluorescence microscopy requires samples to be fluorescently labeled. All of these requirements may alter the native structures of the samples. AFM can image samples in their native conditions. This advantage is ideal for imaging biological samples as AFM offers imaging these samples in their physiological environments whether it is in air or in fluid.[28, 29, 30]

In addition to the advanced imaging capability of AFM, the technique offers additional functionality that is useful in the field of nanobiotechnology. AFM probes can be utilized as a nanoscale manipulator that can manipulate a sample surface or chemical functional groups. Using this nano-manipulator, the mechanisms of molecular recognition and protein folding, the local elasticity, chemical groups and dynamics of receptor–ligand interactions in live cells can be studied. AFM cantilever can also be utilized as a sensor that detects bioanalytes using the sensitive deflection of the cantilever.[31]

Despite the advantages, there are a few challenges in using AFM. First, AFM imaging is relatively slower than optical microscopy techniques because of its innate reliance on raster scanning. Thus, imaging a large sample area can be very time consuming. However, the

speed of AFM imaging has been much improved and it can now achieve tens of frames per second when scan size is in a few hundred nanometer range.[32, 33] Second, since AFM uses a tip for imaging samples, the quality of AFM image is dependent on the quality of the tip. AFM tips may pick up small particles during the imaging process and this may result artifacts that could easily misrepresent the native structures of the sample. Therefore, interpretation of AFM images should be carefully done and control measurements are essential. Also, in order to prevent any physisorption on the tip, chemical functional groups can be introduced on the AFM that makes the tip either hydrophobic or hydrophilic.[27, 34, 35, 36]

1.7 Black lipid membrane

A cell utilizes ion channel proteins in a membrane to maintain ionic homeostasis. Across this membrane, an electrical potential difference exists between the intracellular and extracellular membrane which typically is -70 mV for neurons. Black lipid membrane (BLM) is a model lipid bilayer that mimics the cellular membrane. BLM can be formed around a micron size aperture as shown in the Figure 5. The size of a micro aperture typically ranges from $100\ \mu\text{m}$ to $300\ \mu\text{m}$. This aperture is located in the center of a partition, made from a hydrophobic material such as Teflon, which divides two liquid filled chambers. An electrode is placed in each chamber and an electrical potential can be applied. BLM can be formed in various manners. One method, the “painting” method, utilizes lipids dissolved in an organic solvent which are painted near the micro pore using a brush, syringe, or glass pipette. When the bilayer is formed, the electrical current that could flow through the micro pore is blocked and the two chambers are electrically isolated. Normally, the bilayer has a large resistance ($>G\Omega$) and a large capacitance ($\sim 2\ \text{F}/\text{cm}^2$). Capacitance (C) is a measure of how much charge (Q) can be stored on the membrane for a given potential difference (ΔV)

and is defined as $C = Q/\Delta V$. C depends on the dielectric constant of the lipid molecule (ϵ), surface area (A), and thickness (d) of the membrane and it's defined as $C = \epsilon \cdot \epsilon_0 \cdot A/d$ where ϵ_0 is the electric constant of free space ($8.8542 \times 10^{-12} \text{ F}\cdot\text{m}^{-1}$). Capacitance of a membrane is an important quantity that determines the stability of the membrane. By measuring the capacitance of a lipid membrane, we can estimate the thickness of the membrane. An ion channel protein can be reconstituted in this planar lipid bilayer and the incorporation is recognized by a flow of ionic currents across the membrane. This is typically observed as a stepwise deviation from baseline in a current vs. time trace as ions are transported through the ion channel. The ability of transporting ions through ion channels under an electrical potential difference can be measured as conductance. Conductance (G) is written as the reciprocal of resistance (R). Thus by using an Ohm's law, $\Delta V = I \cdot R$ where ΔV is the potential difference, I is the current, and R is the resistance, G can be derived from the slope of IV curve ($I = G \cdot \Delta V$).

The greatest advantage of using BLM electrical recording setup is that the setup has a resolution to measure single ion channel conductivity. Since the BLM setup can measure currents with pA resolution, study of ion channel activities in various conditions such as pH, lipid composition, and ionic composition is possible.

1.8 Summary of dissertation

This dissertation consists of two main parts. The first part of the dissertation focuses on the characterizations of various A β s in lipid membranes using AFM and BLM techniques to give insights toward finding the disease mechanisms of AD. The second part of the dissertation describes newly developed techniques that can be utilized to study the role of A β proteins in AD as well as other unanswered biological questions. In chapter 2, I

show the biophysical characterizations of two most abundant A β s in the brains of AD patients, A β_{1-42} and A β_{pE3-42} , in anionic model lipid membranes. In chapter 3, I show the structures and ion conducting properties of A β_{1-42} and A β_{17-42} (or p3) in brain total lipid extract membranes and compare the results with the other model lipid membranes. In chapter 4, I show the effect of an AD therapeutic candidate molecule on A β structures and ion conducting activities. In chapter 5, I show the development of new technique, Nanofiber based optical force transducer, that can measure sub pN force from living organisms.

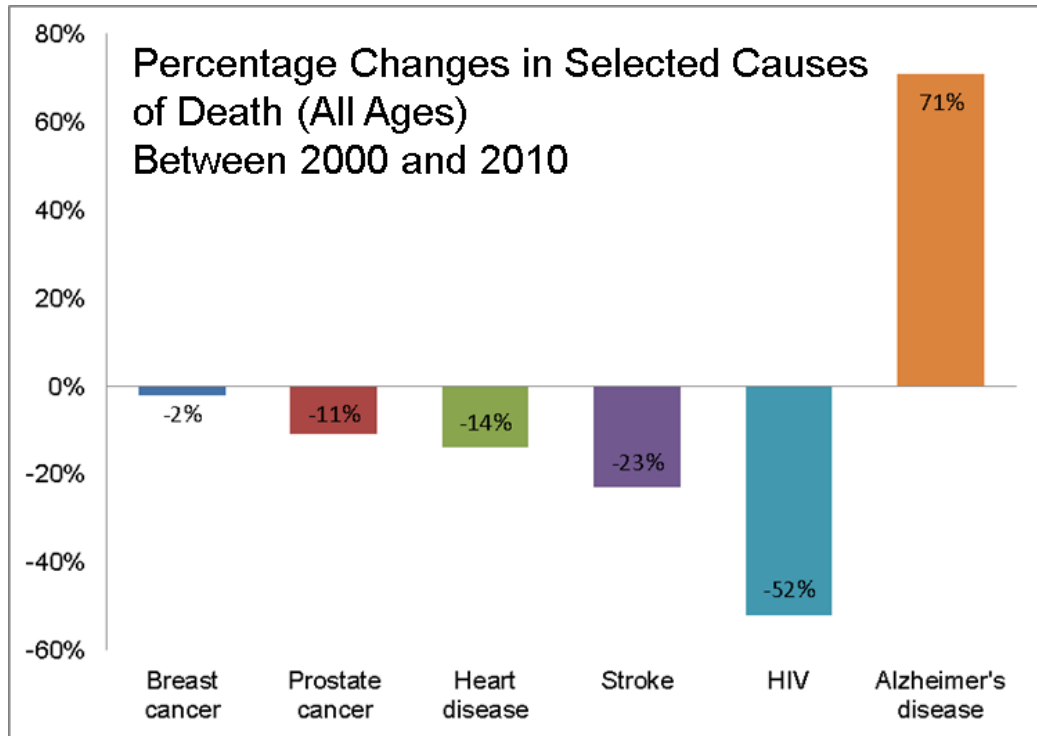


Figure 1.1: Percentage changes in selected causes of death (all ages) between 2000 and 2010.[5]

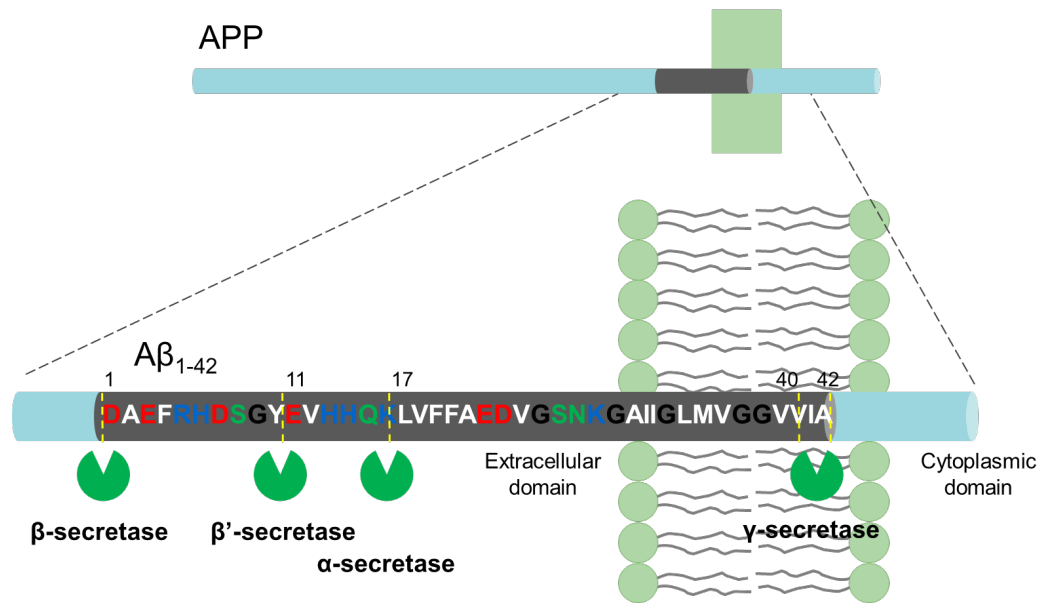


Figure 1.2: Production and molecular properties of Amyloid β . APP (shown in light blue) can be cleaved by several enzymes shown in green shape. Amino acids (aa) of $A\beta_{1-42}$ protein are color coded (blue: positive aa, red: negative aa, green: polar aa, black: non polar aa, white: hydrophobic aa).

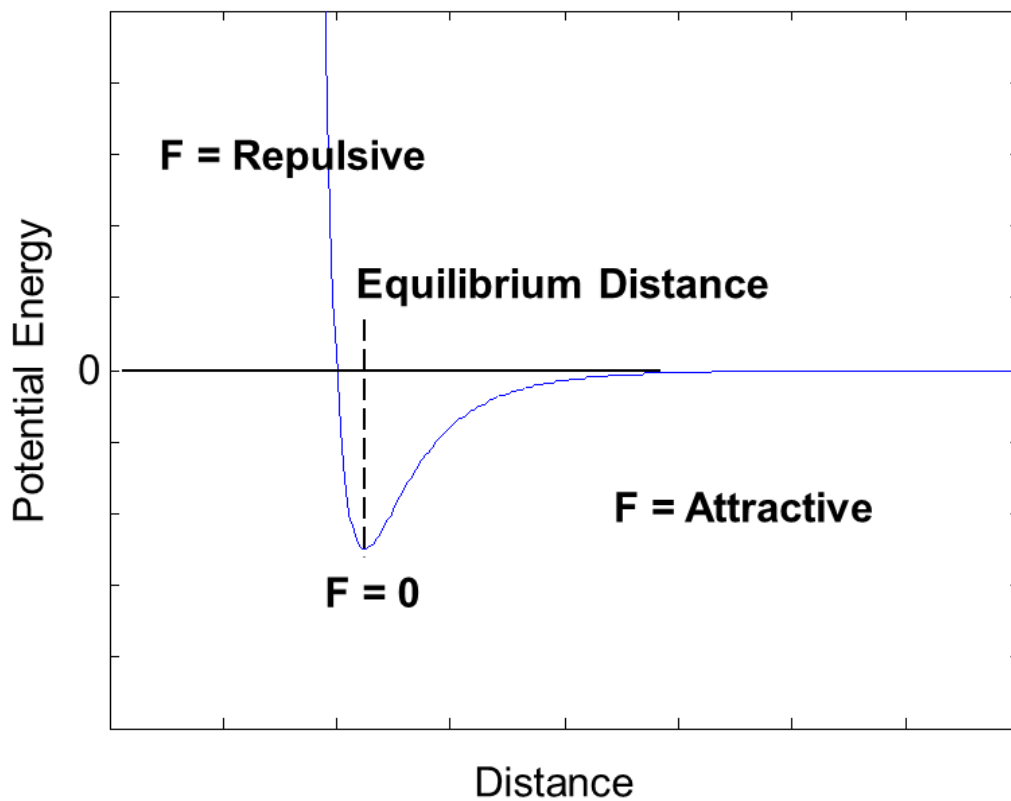


Figure 1.3: Lennard-Jones potential curve. As the interatomic distance decrease from far distance, initial attractive force is experienced. When the distance becomes shorter than the equilibrium distance, repulsive force is experienced.

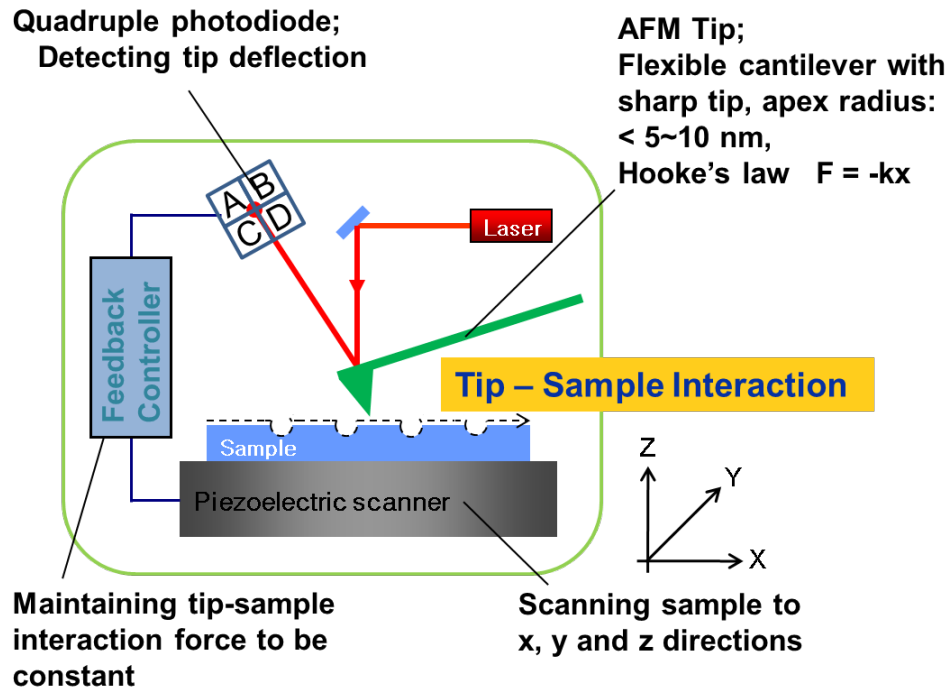


Figure 1.4: Schematics of atomic force microscopy. AFM uses a AFM tip attached at the end of flexible cantilever. Topography of sample can be imaged by raster scanning the sample using a piezoelectric scanner. Depending on the sample height, AFM tip experiences either low or high interaction force as the cantilever is deflected. This interaction force is monitored by a laser aligned on a cantilever and the deflection of the cantilever is measured using quadruple photodiode. Using a feedback controller, the interaction force is set to be constant.

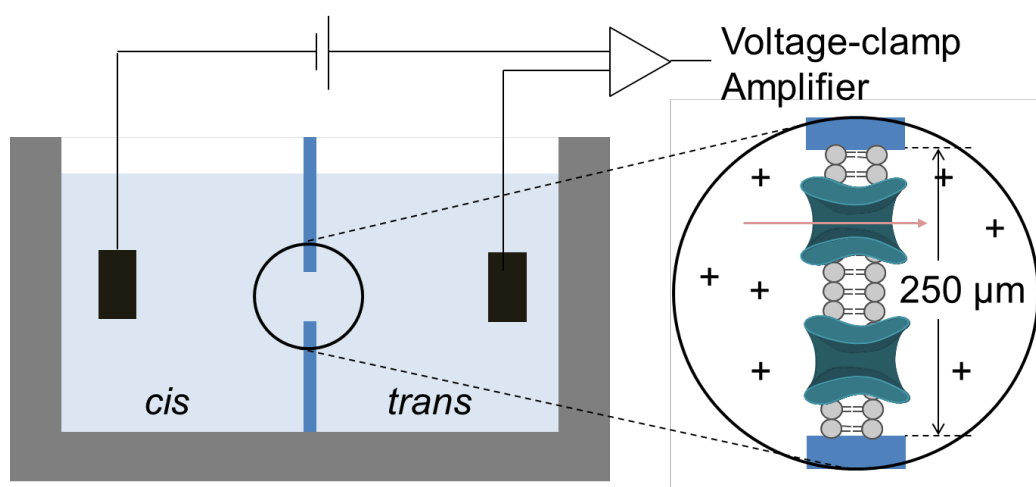


Figure 1.5: Schematics of black lipid membrane setup. Two Ag/AgCl electrodes are immersed in each chamber separated by a micron size aperture ($250\ \mu\text{m}$). Planar lipid bilayer can be formed around the aperture using a painting method. Any leakage current can be measured by using voltage-clamp amplifier.

Chapter 2

Role of the Fast Kinetics of Pyroglutamate-Modified Amyloid- β Oligomers in Membrane Binding and Membrane Permeability

2.1 Abstract

Membrane permeability to ions and small molecules is believed to be a critical step in the pathology of Alzheimer's disease (AD). Interactions of oligomers formed by amyloid- β (A β) peptides with the plasma cell membrane are believed to play a fundamental role in the processes leading to membrane permeability. Among the family of A β s, pyroglutamate (pE)-modified A β peptides constitute the most abundant oligomeric species in the brains of AD patients. Although membrane permeability mechanisms have been studied for full-length A $\beta_{1-40/42}$ peptides, these have not been sufficiently characterized for the more

abundant $A\beta_{pE3-42}$ fragment. Here we have compared the adsorbed and membrane inserted oligomeric species of $A\beta_{pE3-42}$ and $A\beta_{1-42}$ peptides. We find lower concentrations and larger dimensions for both species of membrane-associated $A\beta_{pE3-42}$ oligomers. The larger dimensions are attributed to the faster self-assembly kinetics of $A\beta_{pE3-42}$ and the lower concentrations are attributed to weaker interactions with zwitterionic lipid head groups. While adsorbed oligomers produced little or no significant membrane structural damage, membrane permeabilization to ionic species is understood in terms of enlarged membrane-inserted oligomers having the capability to induce increased pore activity. Membrane-inserted $A\beta_{pE3-42}$ oligomers were also found to modify the mechanical properties of the membrane. Taken together, our results suggest that membrane-inserted oligomers are the primary species responsible for membrane permeability.

2.2 Introduction

Amyloid- β ($A\beta$) peptides play a fundamental role in Alzheimersdisease (AD).[6, 3] They are formed by enzymatic cleavage of the amyloid precursor protein (APP).[37] Although amyloid fibrils were originally believed to be the cytotoxic species in AD,[38] the emphasis has shifted toward smaller oligomers,[39, 40, 2, 41, 42, 19, 43, 18, 17, 44, 45] and a growing body of evidence indicates that intermediate $A\beta$ oligomers are the toxic species while fibrils appear not to be involved in cytotoxicity.[46, 47, 48, 49, 25, 1] Among the family of $A\beta$ peptides, oligomers composed of pyroglutamate (pE)-modified $A\beta$ s appear to be intimately involved in AD,[48, 50, 51, 52] as they constitute the most abundant oligomeric species in the brains of AD patients, but their amount is significantly smaller in brains of age-matched individuals with normal cognition.[48, 50, 51, 52] One of the most abundant species, the $A\beta_{pE3-42}$ fragment, is generated by cleavage of the first two amino acids at the

N-terminus of $A\beta_{1-42}$, leaving a glutamate (E) residue in position 3. The pyroglutamate (pE) residue is subsequently generated by intramolecular dehydration.[48, 52] Self-assembly of $A\beta$ peptides into polymorphic structures and their binding to lipid membranes are key processes in the pathogenesis of AD.[47, 53, 54, 55, 56] Although the exact molecular mechanisms of cell dysfunction are insufficiently understood, they involve the interaction of oligomeric species with the plasma cell membrane.[47, 53, 54, 57, 58, 59] Depending on lipid composition, membranes can promote the conformational changes of $A\beta$ s that lead to the formation of toxic β -sheet structures and serve as nucleation sites for faster self-assembly. In addition, ganglioside-containing membranes have been found to play a role in altering the aggregation pathways of $A\beta$. [60] On the other hand, $A\beta$ oligomers can induce permeabilization of the membrane to unregulated passage of small molecules and ions.[3, 47, 54, 61, 62] Potential mechanisms of membrane permeabilization include carpeting, pore formation, and the detergent effect.[47, 61, 62, 63, 64] Also, recent solid state nuclear magnetic resonance (NMR) studies of $A\beta$ and the islet amyloid polypeptide (IAPP) peptides have shown similarities between the modes of membrane permeabilization of these amyloid peptides and those of the better studied antimicrobial peptides (AMPs).[65, 66] Permeabilization mechanisms appear not to be mutually exclusive; for instance, pore formation appears to occur prior to membrane fragmentation.[21] All permeabilization mechanisms ultimately lead to changes in the cellular ionic concentration, producing a loss of cell homeostasis and subsequent cell death. These processes have been characterized for full-length $A\beta_{1-40/42}$, but similar studies are missing for the $A\beta_{pE3-42}$ fragment. $A\beta_{pE3-42}$ is more hydrophobic than $A\beta_{1-42}$ because of the loss of negative charges from residues Asp1 and Glu3 and the formation of the lactam ring in the pE residue. This increased hydrophobicity affects the kinetics of self-assembly, as well as the interactions of the peptide with the membrane lipids.

Here, we examine different mechanisms of membrane permeability induced by $A\beta_{pE3-42}$ peptides. We compare the kinetics of self-assembly for $A\beta_{pE3-42}$ and $A\beta_{1-42}$ and examine the relationship between self-assembly and membrane binding. We used a mixture of phosphoethanolamine (PE) and phosphoserine (PS) lipid headgroups because these are dominant lipid components in the brains of the elderly,[21] and these levels have been found to change in AD brains.[67] We find lower concentrations of $A\beta_{pE3-42}$ oligomers adsorbed on membrane surfaces, likely reflecting the weaker interactions between the more hydrophobic $A\beta_{pE3-42}$ peptides and the lipid heads. The faster kinetics of $A\beta_{pE3-42}$ self-assembly leads to larger dimensions of the adsorbed $A\beta_{pE3-42}$ oligomers. These adsorbed oligomers produced little or no significant damage to the membrane. Membrane permeabilization to ionic species was observed as pore activity and can be understood as a result of oligomers inserted into the membrane.

2.3 Materials and Methods

2.3.1 Peptide Handling

Both $A\beta_{1-42}$ and $A\beta_{pE3-42}$ with $> 90\%$ purity as provided by the manufacturer (Bachem, Torrance, CA) were first dissolved in 1% ammonium hydroxide until the peptides were completely dissolved. They were subsequently sonicated for approximately 2 min. The desired amount of peptide was aliquoted and lyophilized using a lyophilizer (Labconco FreeZone 2.5 Plus, Kansas City, KS). The aliquots were stored at $-80\text{ }^{\circ}\text{C}$ for a maximum period of 3 months until used. For every experiment, aliquoted peptides were taken from $-80\text{ }^{\circ}\text{C}$ and hydrated in Tris (pH 7.4) or HEPES (pH 7.0) buffer solutions. The peptide concentration was measured using the 280 nm UV absorbance ($\epsilon = 1490\text{ M}^{-1}\bullet\text{cm}^{-1}$).

2.3.2 Thioflavin-T (ThT) Assays

A stock solution of 500 μM ThT in water was prepared and 2 μL were added to 100 μL of 10 mM HEPES (20 mM MgCl_2 , 150 mM NaCl, pH 7.0) buffer in 96-well black-walled plates (Nuncatom, Denmark) to make 10 μM ThT solutions. For peptides, 20 mM NaOH was used to dissolve lyophilized aliquot peptides and prevented from aggregation. After that, the peptide solution was diluted with HEPES to its final peptide concentration in the plate well and the content of NaOH was maintained less than 10% of total volume. ThT fluorescence (450 nm excitation, 490 nm emission) was monitored every 5 min at 25 ° C for the indicated times using a SPECTRAMax Gemini EM fluorescent plate reader (Molecular Devices, Sunnyvale, CA). The obtained curves were fitted using sigmoidal curve in eq. 2.1 below,[66]

$$F = F_0 + \frac{a}{1 + e^{-k(t-t_{1/2})}} \quad (2.1)$$

where t is time, $t_{1/2}$ is the time to reach half-maximum of ThT fluorescence, F_0 is the initial fluorescence intensity, a is the amplitude of the maximum intensity, and k is the rate constant. The lag phase time was calculated from the fitting parameters obtained above, using:

$$t_{\text{lag}} = t_{1/2} - \frac{2}{k} \quad (2.2)$$

2.3.3 Lipid Bilayer Preparation for AFM Imaging

For liposome preparation, 1-palmitoyl-2-oleoyl-sn-glycero-3-phosphoethanolamine (POPE) and 1,2-dioleoyl-sn-glycero-3-phospho-L-serine (DOPS) lipids were used in a 1:1 ratio (both purchased from Avanti Polar Lipids, Alabaster, Al). Liposomes were prepared by mixing 20 μL of each lipid (5 mg/mL) dissolved in chloroform and allowed to dry overnight

in vacuum. The dried lipid film was hydrated with peptide solution to facilitate peptide incorporation in the lipid bilayer, resulting in proteoliposome formation. For preparation of control liposomes, 200 μL of 25 mM Tris buffer (300 mM NaCl, pH 7.4) were used. The resulting liposome and proteoliposome suspensions were vortexed occasionally for approximately an hour for better hydration. The large multilamellar vesicles formed with this procedure were sonicated for 5 min. These suspensions were subsequently extruded using 100 nm filters to produce small unilamellar vesicles. Supported lipid bilayers were formed by (proteo)liposome rupture and fusion on the mica substrate.[17, 44, 63, 64, 65, 66]

Lipid concentrations of 0.1~1 mg/mL were deposited on freshly cleaved mica and incubated for ~ 10 min on a hot plate above the lipid transition temperature to facilitate fusion of the ruptured proteoliposomes on the mica surface. As a last step, samples were rinsed with buffer to remove unruptured proteoliposomes still in solution. For incubation of $\text{A}\beta_{pE3-42}$ on preformed lipid bilayer experiments, liposomes were allowed to form supported lipid bilayers on mica. The formation of bilayer patches was verified by AFM before incubation in peptide solutions. $\text{A}\beta_{pE3-42}$ was injected in a buffer solution at the final concentration of 20 μM for a given time at room temperature.

2.3.4 AFM Imaging

Topographic images were acquired using a Multimode AFM equipped with a Nanoscope V controller (Bruker, Santa Barbara, CA). Silicon cantilevers with spring constant of 48 N/m (NSC11, JPK) were used for imaging in air using tapping mode. Silicon Nitride cantilevers with spring constants of 0.08 N/m (OMCL-TR400, Olympus) were employed for imaging in fluid using tapping mode. Resonance frequencies of ~ 8 kHz and drive amplitudes under 100 mV were used.

The Nanoscope software was used for analyzing imaging data. Particle analysis was used for measuring the number of membrane-associated oligomers. Section analysis was used for measuring widths and heights of membrane-associated oligomers. Oligomer widths were measured as full widths at half the maximum height (FWHM) in section profiles and these values were corrected to take tip widening effects into account. Based on previous models,[21, 68, 69] tip widening of the oligomer structures was corrected by modeling the tip as a sphere of radius, R , imaging a spherical cap of radius, r , protruding a height, h above the surface of the lipid bilayer (eqs. 2.3-2.4).

$$D=2\sqrt{\left(rh - \frac{h^2}{4}\right)} \quad (2.3)$$

$$r = \frac{x^2 - 2Rh + h^2}{2h} \quad (2.4)$$

where D is the corrected oligomer diameter and $w = 2x$ is the measured width at half-height. Similarly, tip widening of the adsorbed oligomers was modeled as a spherical tip of radius R in contact with another sphere of radius r located on a surface.

$$y = r - R + \sqrt{(R+r)^2 - x^2} \quad (2.5)$$

where y is the height of the tip above the surface and $w = 2x$ is the measured width at height y . Because widths were measured at half the measured oligomer height, we set y equal to r . Origin software (OriginLab Corporation, Northampton, MA) was used to generate histograms and fitting curves in this and all other sections.

2.3.5 AFM Force Mapping

For force mapping experiments, the AFM was changed to force volume mode after imaging an area of interest. Forces of less than 12 nN and tip velocities of 800 nm/s were used. Force curves were acquired point by point in each point of a 32 x 32 array (force map). Data processing for force mapping data was done by using custom-made MATLAB (Natick, MA) program. Breakthrough forces were measured with this program by detecting the force discontinuity during a breakthrough event. When no event was detected, the breakthrough force was set to zero and no further analysis was performed on that curve. Statistical distributions of breakthrough forces were fitted with Gaussian functions. All experiments were performed at room temperature. Actual spring constants were measured using the thermal tune method before the experiments.[70]

2.3.6 Planar Lipid Bilayer Electrical Recording

For electrical Recording experiments with planar lipid bilayers (known as BLM for Black Lipid Membranes because they appear “black” when viewed by reflected light),[71, 72] A β_{pE3-42} peptides were dissolved in Milli-Q water to a concentration of 1 mg/mL and subsequently used a single time. Membranes were composed of DOPS and POPE mixtures (1:1 by weight) in heptane at a total lipid concentration of 20 mg/mL. For membrane formation, lipid was added directly over a hole ($\sim 250 \mu\text{m}$ diameter) in a Delrin septum (Warner Instruments, Delrin perfusion cup, volume 1 mL). As electrolyte, we used 150 mM KCl, 10 mM HEPES (pH 7.4), and 1 mM MgCl₂. Before data acquisition, we verified that the bilayer was stable for several minutes with low conductance ($< 10 \text{ pS}$) across $\pm 100 \text{ mV}$ applied voltage and that the system capacitance was $> 110 \text{ pF}$. When both criteria were met, peptide solution was added to one of the compartments of the bilayer chamber (*cis* side),

reaching a final concentration of $\sim 10 \mu\text{M}$. The solution was stirred for 5 min before data acquisition. Bilayer stability was monitored by periodic capacitance measurements.

All traces were recorded in voltage clamp mode using the 2 kHz built-in filter cutoff of our BC-535 amplifier (Warner Instruments, Hamden, CT). A sampling frequency of 15 kHz was used for data acquisition. We used a custom-made LabVIEW (National Instruments, Austin, TX) program to record the current and Clampfit 10.2 (Molecular Devices, Sunnyvale, CA) to analyze traces. For representation in figures, time traces were filtered with a digital Gaussian low-pass filter with a cutoff frequency of 50 Hz.

2.4 Results

2.4.1 Kinetics of $\text{A}\beta_{pE3-42}$ Self-Assembly in Solution.

The ThT fluorescence was used to compare the kinetics of fibril self-assembly for $\text{A}\beta_{1-42}$ and $\text{A}\beta_{pE3-42}$ peptides (Figure 2.1). $\text{A}\beta_{pE3-42}$ peptides have faster self-assembly kinetics, indicated by a considerably shorter lag phase and a faster elongation phase (Figure 2.1A). The lag phase for $\text{A}\beta_{pE3-42}$ becomes visible only at the lower concentrations (Figure 2.1B). Their lag phase times and rate constants using eqs 1 and 2 are as follows: $t_{lag} = 1.14$ h and $k = 0.51 \text{ h}^{-1}$ for the $5 \mu\text{M}$ solution, and $t_{lag} = 2.01$ h and $k = 0.31 \text{ h}^{-1}$ for the $2.5 \mu\text{M}$ solution. From the fitted curves in Figure 2.1A, we obtained a t_{lag} of 13.51 h and a k of 0.46 h^{-1} for $\text{A}\beta_{1-42}$.

Our results are in good agreement with previous results for $\text{A}\beta_{1-40}$ and $\text{A}\beta_{pE3-40}$,^[73] although those lag phase times are considerably longer. This is possibly due to the two additional hydrophobic residues (Ile41 and Ala42) at the C-terminus of the $\text{A}\beta_{1-42}$ and $\text{A}\beta_{pE3-42}$ peptides. AFM was used to characterize the morphology of the self-assembled

species. Only globular and small linear oligomers were seen in the initial state of the freshly prepared $A\beta_{pE3-42}$ and $A\beta_{1-42}$ oligomers (Figure 2.2). While annular $A\beta_{pE3-42}$ protofibrils were already seen after incubation for 30 min at room temperature (Figure 2.2A), globular $A\beta_{1-42}$ oligomers were still found even after incubation for 14 h (Figure 2.2B). The diameters of $A\beta_{pE3-42}$ oligomers changed significantly after 0.5 h, whereas the diameters of $A\beta_{1-42}$ oligomers remained approximately constant after 14 h (Table 2.1). The heights changed by a factor of ~ 2 for both peptides (Table 2.1). As regions with high concentrations of $A\beta_{pE3-42}$ fibrils were already seen after 48 h (Figure 2.2A), only protofibrils and large quantities of $A\beta_{1-42}$ oligomers were observed (Figure 2.2B). $A\beta_{1-42}$ fibrils were found only after incubation for several days. These results correlate well with the ThT data discussed above (Figure 2.1A).

2.4.2 Membrane-Adsorbed $A\beta_{pE3-42}$ Oligomers

We used AFM to characterize the morphology of $A\beta$ oligomers adsorbed on anionic membranes and the loss of membrane integrity induced by these oligomers. We attempted to monitor the adsorption of $A\beta_{pE3-42}$ oligomers when they were allowed to interact with preformed supported lipid bilayers. We did not observe oligomer adsorption even after incubation for several hours in the AFM liquid cell. Instead, fibrils were observed on membrane regions after ex situ incubation for 38 h (Figure 2.3). Significantly, membrane patches appeared to be intact without a substantial number of adsorbed $A\beta_{pE3-42}$ oligomers or apparent defects in the lipid bilayer. These results suggest weak interactions between $A\beta_{pE3-42}$ oligomers and headgroups in the lipid membrane. In comparison, oligomeric and fibrillar self-assembled structures of full-length $A\beta$ s were found to form on different supported membranes.[74, 75, 76, 77, 78]

To increase the probability of A β peptides interacting with membrane lipids, lipids were hydrated into liposomes in the presence of peptides, subsequently sonicated together, and finally extruded to form unilamellar proteoliposomes. Following this method, large quantities of A β_{pE3-42} oligomers adsorbed on a seemingly flat membrane were seen (Figure 2.4A). The adsorbed A β_{pE3-42} oligomers (green circles) have typical diameters in the range of 30-40 nm and heights of 2-10 nm (Figures 2.4A and 2.5A,C and 2.1). In addition, bilayer deep (~ 5 nm) gaps separating regions of seemingly intact patches are observed. Smaller structures (≤ 2 nm in height) are found in these flatter regions, suggesting the presence of membrane-inserted oligomers.

We compared the density and dimensions of adsorbed A β_{pE3-42} oligomers with those of A β_{1-42} oligomers. The A β_{1-42} oligomers have higher concentrations (~ 200 oligomers/ μm) and smaller dimensions compared to those of the A β_{pE3-42} oligomers even though their heights are similar (Figures 2.4B and 2.5A,C and Table 2.2). In addition, a large surface density of membrane defects with depths of one bilayer (dark spots) is observed. At lower peptide:lipid ratios (Figure 2.4C), the number of these defects was no longer significant and most of the observed structures protruded ≤ 2 nm from the bilayer plane, suggesting a majority of inserted oligomers.

2.4.3 Membrane-Inserted A β_{pE3-42} Oligomers.

In addition to the adsorbed oligomers discussed above, we observed numerous smaller structures protruding < 2 nm from the membrane plane (red circles in Figures 2.4A,B). These structures are attributed to populations of oligomers inserted into the membrane. Similar to the membrane-adsorbed oligomers, the inserted A β_{1-42} oligomers have higher concentrations and smaller dimensions compared to those of the A β_{pE3-42} oligomers

(Figures 2.4A,B and 2.5B,D and Table 2.2). Most of these oligomers have a globular appearance (Figure 2.6A), although a smaller subpopulation of pore-forming oligomers was also found (inset). Their electrophysiological activity is indicated by discrete features in the ionic current passing through the lipid membrane (Figure 2.6B), with pore conductances of <0.7 nS.[79] From these data, the pore diameters can be roughly approximated (Figure 2.6C) using eq. 2.6:[80, 81]

$$r = r_0 \left[1 + \left(1 + \left(\frac{4L}{\pi r_0} \right)^{1/2} \right) \right] \quad (2.6)$$

with r is the pore radius, $r_0 = G/4\sigma$, G is the single-pore conductance, σ is the solution conductivity (~ 1.5 S/m for 150 mM KCl), and L is the pore length (~ 6 nm). After longer recording times (~ 20 min following the first activity) and in approximately 50% of our experiments, an exponential-like phase was observed before the saturation current of the amplifier was reached.[79] We conducted force measurements on membrane patches with inserted $A\beta_{pE3-42}$ oligomers. We characterized the mechanical properties of these membranes by measuring the breakthrough force seen in indentation curves. These curves show that lipid membranes are first deformed elastically by the AFM tip (O- F_B region in Figure 2.7A). At the critical breakthrough force, marked by a discontinuity in the curve, the membrane undergoes an irreversible (plastic) deformation. The breakthrough force has been characterized for different lipid membranes and found to be sensitive to lipid composition, ionic strength, and temperature.60-69 We measured a value of 1.31 ± 0.22 nN (mean value \pm the half-width at half-maximum) for the breakthrough force of DOPS/POPE membranes. Insertion of $A\beta_{pE3-42}$ oligomers significantly increased this value by $\sim 40\%$ (Figure 2.7B-D).

2.5 Discussion

Using ThT fluorescence, we have found that self-assembly of $A\beta_{pE3-42}$ oligomers into fibrils has faster kinetics than that of $A\beta_{1-42}$ (Figure 2.1). During the first phase, the lag phase, monomers and small oligomers nucleate with very slow kinetics into β -structured oligomers serving as nucleation seeds. In the second phase, these seeds elongate into amyloid fibrils at a much faster rate as more peptides are incorporated into the preformed seeds. Hydrophobic interactions and hydrogen bonding are the driving forces behind the self-assembly processes leading to amyloid fibril formation.[82] A recent ^{19}F NMR study has reported multiple oligomeric species in the lag phase, including α -helix and reversible β -sheet oligomers.[83] In addition, it has been reported that $A\beta_{1-40}$ adopts a compact, partially folded structure, forming a 310-helix in the H13-D23 central hydrophobic region,[84] and that these helical intermediates are crucial intermediates in amyloid self-assembly.

Annular protofibrils with polygonal appearances and diameters of 8-25 nm have been observed by transmission electron microscopy (TEM) for $A\beta_{1-42}$ as a product of their aggregation process.[85] The diameters of the $A\beta_{pE3-42}$ annular protofibrils we found (Figure 2.2A) are significantly larger, ranging from 80 to 200 nm. The shapes we observed agree with the TEM observations for $A\beta_{1-42}$; thus, they cannot be attributed to AFM imaging artifacts. Although annular protofibrils have been reported for many different amyloids,[18, 86, 87, 88] their structures, interrelationships, and contributions to disease pathogenesis are not entirely clear.[85]

We have considered mechanisms of membrane permeability and loss of membrane structural integrity induced by $A\beta_{pE3-42}$ oligomers (i) adsorbed on the membrane and (ii) inserted into the membrane. We observed a higher surface density of adsorbed $A\beta_{pE3-42}$ oligomers when they were allowed to interact with lipids during lipid hydration and lipid self-

assembly into liposomes (method 1) than when the oligomers were injected on preformed supported bilayers (method 2). This observation suggests that the former oligomers have a different, more favorable membrane-binding conformation than the latter. The additional energy necessary for oligomers to acquire this conformation might be provided during the sonication step in method 1. The higher fluidity of the liposome membrane might also facilitate rearrangement of the peptide in method 1, compared to the surface-supported membrane of method 2.

We found significantly larger dimensions and lower densities for membrane-adsorbed and membrane-inserted $A\beta_{pE3-42}$ oligomers than for $A\beta_{1-42}$ oligomers (Figures 2.4 and 2.5 and 2.1). The larger size of $A\beta_{pE3-42}$ oligomers is attributed to their faster kinetics of self-assembly (Figures 2.1 and 2.2). The higher density of $A\beta_{1-42}$ oligomers appears to be counterintuitive because of the repulsion expected between the negatively charged Asp1 and Glu3 residues of $A\beta_{1-42}$, with the also negatively charged PS headgroups in the membrane. However, this higher density of $A\beta_{1-42}$ oligomers is understandable if we hypothesize that PE-rich domains are induced by $A\beta_{1-42}$ oligomers due to attractive charge-dipole interactions between the negatively charged residues and the zwitterionic PE headgroups (Figure 2.8), thus leading to formation of PE-rich proteoliposomes during lipid hydration in our proteoliposome preparation protocol (method 1). In addition, the larger size of $A\beta_{pE3-42}$ oligomers would increase the barrier for membrane insertion leading to lower densities of inserted $A\beta_{pE3-42}$ oligomers. However, once the peptide is inserted, the stronger interactions of the more hydrophobic $A\beta_{pE3-42}$ with the lipid tails would lead to a more stable conformation in the hydrophobic lipid core.

We interpret the high level of fragmentation of supported membranes formed from $A\beta_{1-42}$ proteoliposomes (Figure 2.4B) to be due to insufficient vesicle fusion induced by

the high concentration and steric repulsion of membrane-inserted $A\beta_{1-42}$ oligomers (Figure 2.8). The larger dimensions of inserted and adsorbed $A\beta_{pE3-42}$ oligomers (Figure 2.5 and Table 2.2) are attributed to their faster kinetics of self-assembly (Figures 2.1 and 2.2 and Table 2.1). We believe that even relatively low concentrations of $A\beta_{pE3-42}$ oligomers can produce high cytotoxicity because of higher level of pore formation and higher stability in the membrane. Our BLM results indicating a larger populations of high-conductance $A\beta_{pE3-42}$ pores as well as our molecular dynamics (MD) simulations indicating a more stable stable membrane conformation of inserted $A\beta_{pE3-42}$ pore structures lead to a similar conclusion.[79]

Among the populations of membrane-inserted oligomers, pore structures are observed less frequently than globular structures, suggesting that the former structures represent a minority population in the membrane. This is partly due to experimental difficulties in achieving a sufficiently high resolution by AFM, including the inability of broad tips to resolve pore features and the potential distortion of pore structures induced by tip-sample interactions. It should be noted, however, that even small pore populations have the ability to produce high cytotoxicity. It was estimated that a single pore with a 4 nS conductance would produce a loss of cell homeostasis in seconds.[89, 90] A group of pores with the conductances observed in our data (≤ 0.7 nS) would lead to a similar result.

Because of the different sensitivities between AFM imaging and BLM, higher pore concentrations are required for AFM imaging. For BLM, the opening of a single pore can produce a detectable increase in the current across the bilayer. As bilayer areas have typical dimensions of $\sim 10^4 \mu m^2$, pore densities of $\sim 10^{-4}$ pores/ μm^2 can be detected by BLM. However, pore densities of $\sim 10^2$ - 10^3 pores/ μm^2 are necessary for optimal AFM imaging (1-10 pores for 100 nm \times 100 nm imaging areas). Therefore, BLM provides information about

early stages of pore formation when pore densities are low, while AFM gives information about later stages when the concentration of membrane-inserted oligomers is higher.

The pore diameters found using eq. 2.6 (Figure 2.5C) are in general smaller than those predicted in MD simulations and seen by AFM imaging (Table 2.3). The relation in eq. 2.6 assumes a cylindrical geometry with no charge along the length of the pore, while A β pores have a charged surface and a nonuniform geometry. As a result, the relation provides only a very rough estimate of pore diameter that is used as a ballpark figure. With this in mind, the calculated diameters compare reasonably well with the inner diameters of A β pores found using MD simulations and AFM imaging (\sim 1.5-2.5 nm). The structures of these membrane-embedded pores have been well characterized by AFM for full-length A β s,[17, 44, 21] A β ₁₋₄₂ point substitutions,[90] A β fragments,[51, 91] and other amyloidogenic proteins.[44, 92] Here, they were not investigated in detail. The pore diameters for 18-mers of A β _{pE3-42} found using atomistic MD simulations were 1.9 and 2.2 nm for two different A β conformers.[79]

We measured a 40% increase in the breakthrough force of membranes allowed to interact with A β _{pE3-42} oligomers using method 1 of sample preparation. For these experiments, we used a 1:10 peptide:lipid ratio. At this ratio, we observed a sizable population of inserted A β _{pE3-42} oligomers (Figure 2.6), but not many adsorbed oligomers. In the presence of the latter population, the mechanical response measured by the tip likely would have been dominated by the adsorbed oligomers directly under the tip, not by their influence on the mechanical properties of the membrane. Therefore, our results indicate that the population of inserted oligomers induces a significant modification of the mechanical properties of the membrane.

The higher breakthrough force measured for membranes with inserted A β _{pE3-42}

oligomers would suggest (i) the presence of local populations of rigid β -sheet oligomers, leading to increased local stiffness, or (ii) an increased global ordering of the membrane lipids induced by the $A\beta_{pE3-42}$ oligomers, thus leading to a global increase in the stiffness of the membrane, similar to the modulation of membrane stiffness induced by cholesterol molecules.[93, 94, 95, 96, 97, 98, 99, 100] From our measurements, we cannot discriminate which mechanism is predominant. Both stiffer and more flexible membranes could lead to higher membrane permeability, although by different mechanisms. A membrane hole would likely heal slower for stiffer membranes, thus enhancing permeability, and a more flexible hole would decrease the membrane thickness, also leading to increased permeability. Previous results found the breakthrough force of POPC/POPS membranes to increase when they were allowed to interact with $A\beta_{1-40}$ oligomers and to be dependent on the aggregation state of the peptide.[101] Significantly, $A\beta_{1-42}$ oligomers induced a decrease in the breakthrough force of supported membranes.[102] Some variability in the results is not surprising, as the free energy landscape of $A\beta$ s has been found to be highly dependent on the exact experimental conditions.[51, 52, 82]

2.6 Conclusion

We have examined the effect of $A\beta_{pE3-42}$ oligomers on the ion permeability and the structural and mechanical properties of anionic lipid membranes. We have found lower concentrations and larger dimensions for the adsorbed and membrane-inserted $A\beta_{pE3-42}$ oligomers compared to those of $A\beta_{1-42}$. The larger sizes of $A\beta_{pE3-42}$ oligomers are attributed to their faster kinetics of self-assembly. The lower concentrations are attributed to their weaker interactions with the membrane lipids. However, once inserted into the membrane, these larger $A\beta_{pE3-42}$ oligomers induce considerable ion permeability through

the membrane and are stable in the lipid core of the membrane because of their increased hydrophobicity. The adsorbed $A\beta_{pE3-42}$ oligomers appeared to have little effect on the structural integrity of the membrane. Membrane permeabilization can be understood more easily as a result of the membrane oligomers. These oligomers also produced a change in the mechanical properties of the membrane, suggesting a reordering of membrane structure.

2.7 Acknowledgements

Chapter 2, in part, is a reprint of the material as it appears in Lee, J.; Gillman, A. L.; Jang, H.; Ramachandran, S.; Kagan, B. L.; Nussinov, R.; Teran Arce, F. Role of the Fast Kinetics of Pyroglutamate-Modified Amyloid- β Oligomers in Membrane Binding and Membrane Permeability. *Biochemistry* **2014**, *53*, 4704–4714. The dissertation author was the primary author of this paper.

Support by the National Institutes of Health (R01AG028709) is acknowledged. This project has been funded in whole or in part with Federal funds from the Frederick National Laboratory for Cancer Research, National Institutes of Health (NIH), under Contract HHSN261200800001E. This research was supported, in part, by the Intramural Research Program of the NIH, Frederick National Lab, Center for Cancer Research.

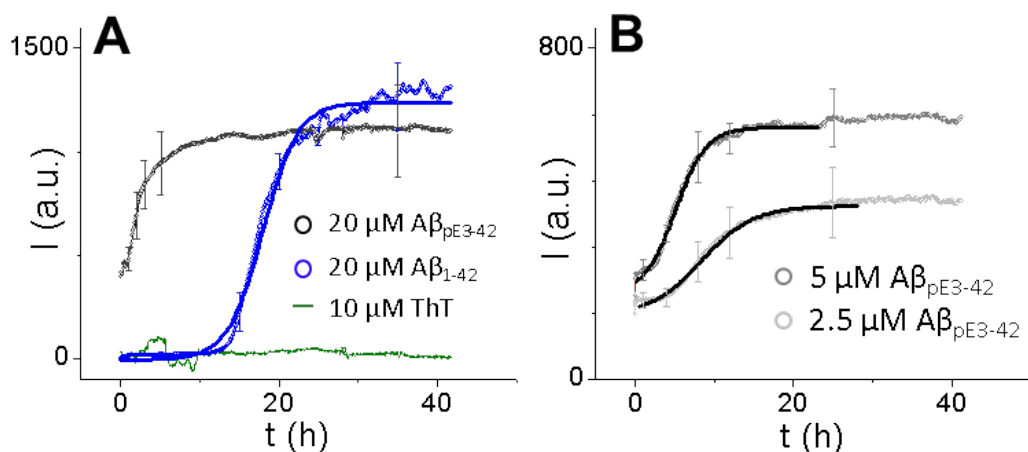


Figure 2.1: Self-assembly kinetics of Aβ₁₋₄₂ and Aβ_{pE3-42} measured by thioflavin-T (ThT) fluorescence at 25 °C. The ThT intensity (I) was monitored as a function of time (t) for (A) Aβ_{pE3-42} (black) and Aβ₁₋₄₂ (blue) solutions (fitted curve shown with a solid blue line) with 20 μM concentrations (a.u., arbitrary units) and (B) 5 μM (dark gray) and 2.5 μM (light gray) solutions of Aβ_{pE3-42}. Fitted curves are shown with black lines. t_{lag} and k were obtained from the fitted curves using eqs 1 and 2.

Table 2.1: Heights (h), Widths (W), and Diameters (D) for the globular and annular oligomers of Aβ₁₋₄₂ and Aβ_{pE3-42} shown in Figure 2.2 at the indicated times (n = 28 for all entries)^a

	Aβ ₁₋₄₂ (t = 0 h) ^b	Aβ _{pE3-42} (t = 0 h) ^b	Aβ ₁₋₄₂ (t = 14 h) ^b	Aβ _{pE3-42} (t = 0.5 h) ^b
<i>h</i> (nm)	1.7 ± 0.7	1.1 ± 0.6	3.9 ± 1.6	2.3 ± 0.9
<i>W</i> (nm)	18.3 ± 4.4	22.1 ± 6.4	19.0 ± 4.4	136.4 ± 33.8 ^c
<i>D</i> (nm)	7.3 ± 3.1	10.1 ± 5.0	7.7 ± 3.1	136.4 ± 33.8 ^c

^a The tip widening effect was considered for *D* using eq 2.5. ^b Values are presented as averages ± the standard deviation. ^c The peak-peak distance (not affected by tip widening) was measured.

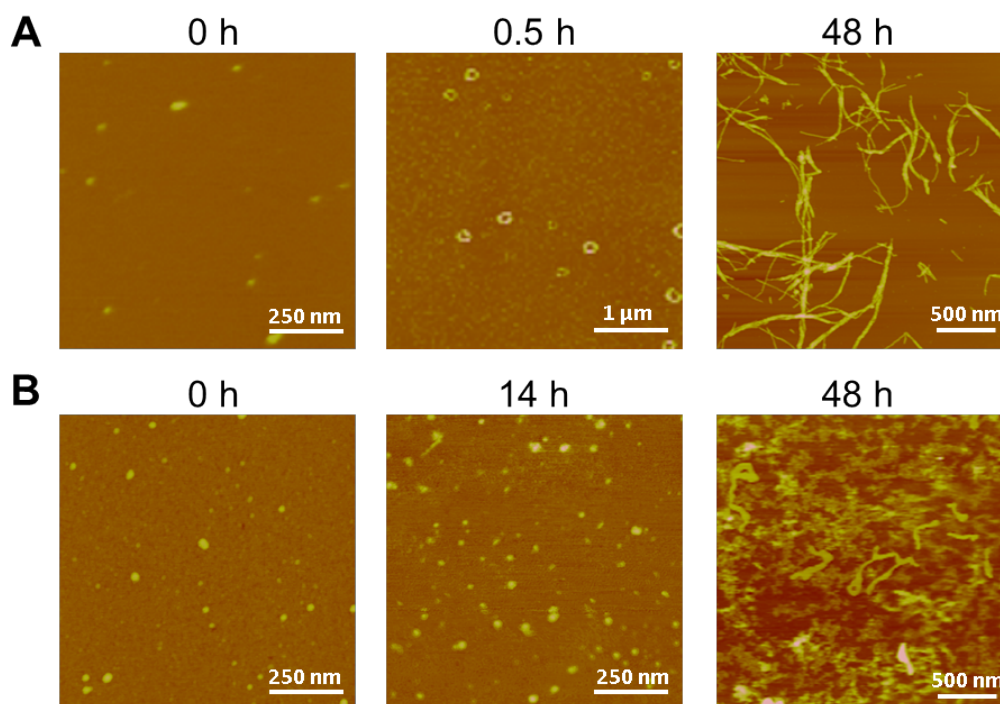


Figure 2.2: AFM images of (A) $A\beta_{pE3-42}$ and (B) $A\beta_{1-42}$ aggregated peptides after different periods of incubation. Images were acquired in air for samples deposited on a mica surface. The lateral scale bar is 250 nm for all images and the vertical color-coded scale is 10 nm everywhere except for the 48 hour images, where it is 50 nm. A few double tip artifacts along the x-axis can be seen for the 48 hour image in (A).

Table 2.2: Density, n_O , of membrane-associated oligomers (inserted and adsorbed) as well as measured widths, diameters and heights of inserted, W_I , D_I , h_I , and adsorbed, W_A , D_A , h_A of $A\beta_{1-42}$ and $A\beta_{pE3-42}$ oligomers, respectively.

Peptide	n_O (μm^{-2})	W_I (nm) ^a	W_A (nm) ^a	D_I (nm) ^{a,b}	D_A (nm) ^{a,b}	h_I (nm) ^a	h_A (nm) ^a
$A\beta_{pE3-42}$	43	38.19 ± 6.85	62.16 ± 12.52	23.59 ± 4.23	41.11 ± 8.32	1.38 ± 0.24	5.67 ± 1.48
$A\beta_{1-42}$	195	22.74 ± 6.74	33.53 ± 5.73	13.97 ± 5.72	23.59 ± 4.23	1.79 ± 0.44	6.20 ± 2.39

^a Values are represented as peak center \pm HWHM from the Gaussian fitting. ^b Diameters were obtained from the measured widths by taking into account eq. 2.3 for tip deconvolution.

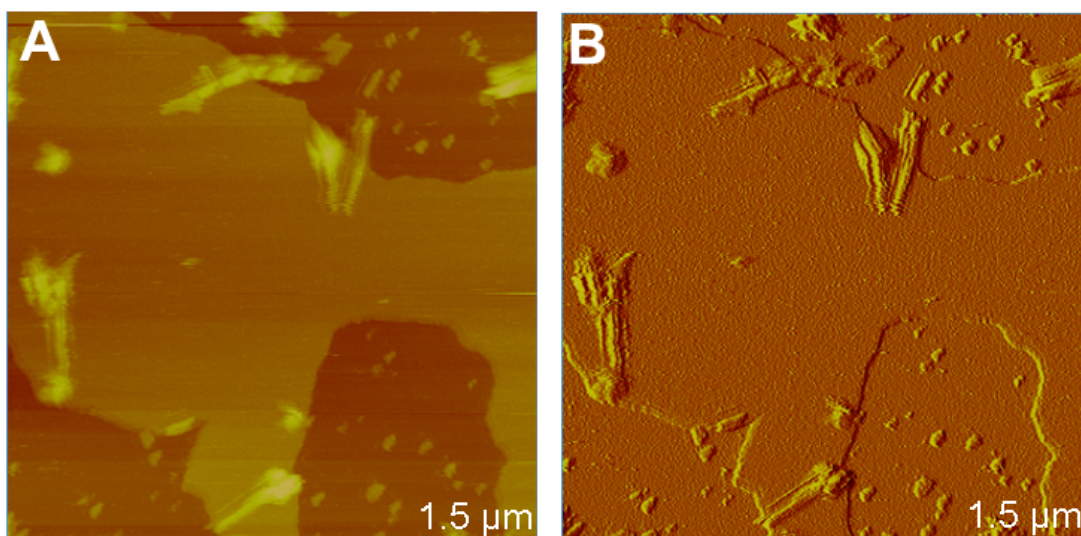


Figure 2.3: AFM (A) height and (B) amplitude images of $A\beta_{pE3-42}$ fibrils formed on supported DOPS/POPE (1:1) lipid membrane after incubation for 38 hours at room temperature. Fibril structures on a seemingly membrane intact are observed. The vertical scale is 25 nm for (A).

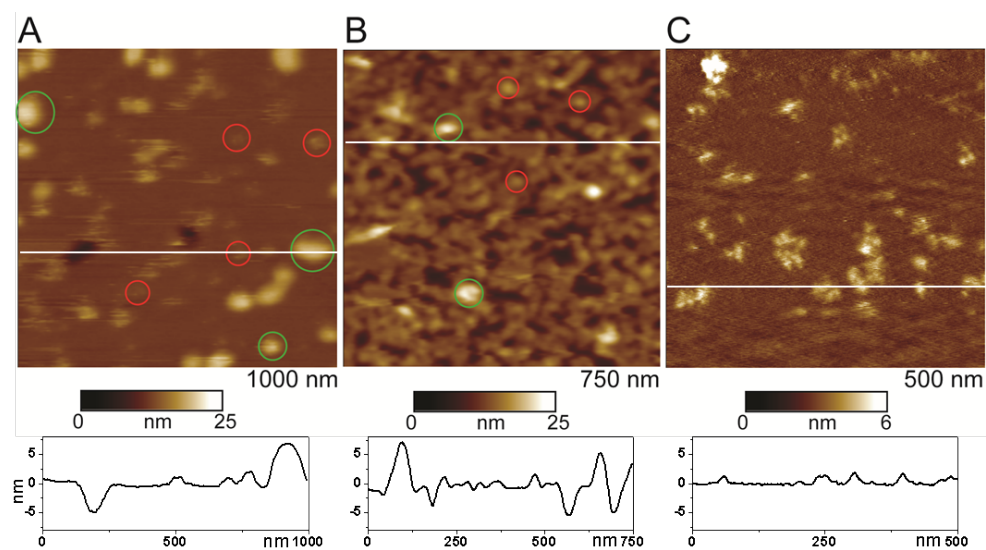


Figure 2.4: AFM images of (A) $A\beta_{pE3-42}$ oligomers and membrane defects induced by the oligomers in a DOPS/POPE (1:1) lipid bilayer. (B) $A\beta_{1-42}$ oligomers adsorbed on a lipid bilayer with the same composition as above. Peptide/lipid mass ratios are 1:2 in (A)-(B) and 1:10 in (C).

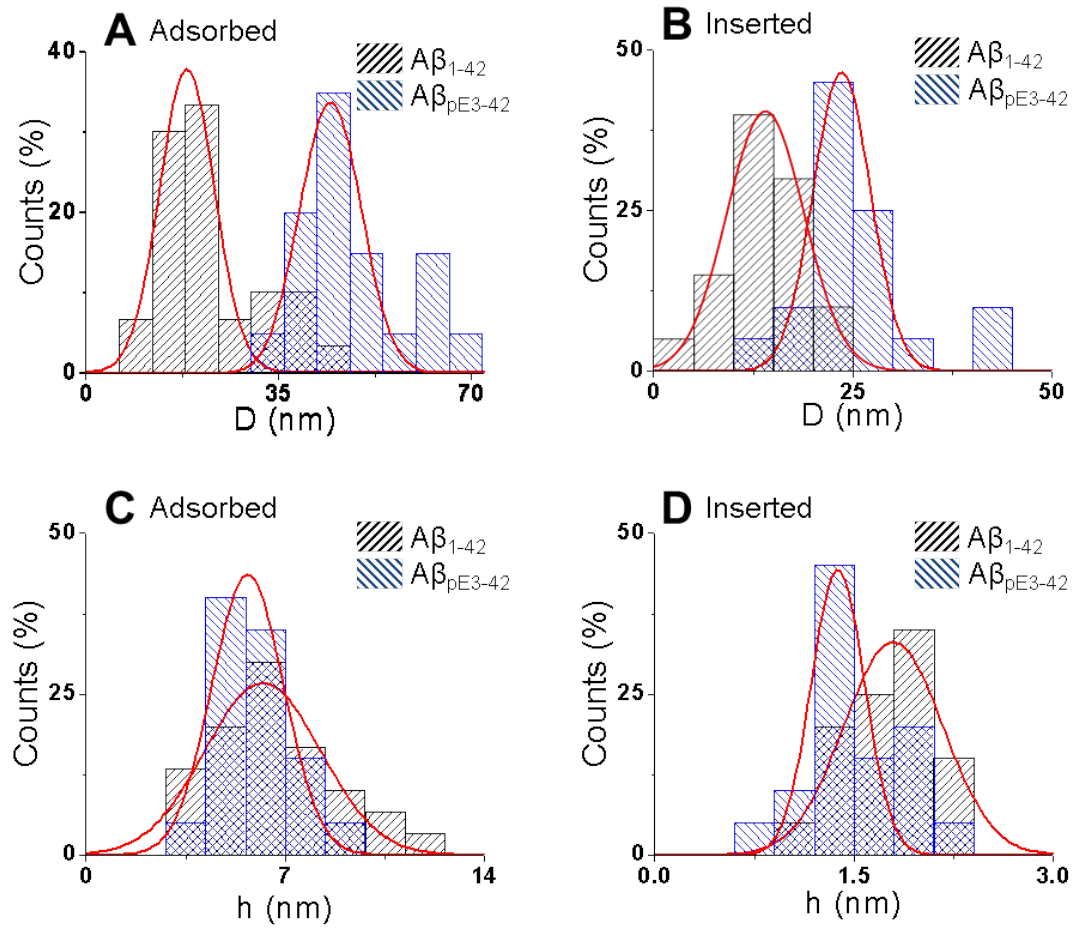


Figure 2.5: Diameter and height histograms of inserted and adsorbed oligomers obtained from AFM images similar to Fig. 2.4. (A) Diameter, D , histograms for membrane-adsorbed oligomers of $A\beta_{pE3-42}$ (blue) and $A\beta_{1-42}$ (black). $A\beta_{pE3-42}$ oligomers have a diameter $D_A(A\beta_{pE3-42}) = 43.77 \pm 7.59$ nm, while $D_A(A\beta_{1-42}) = 21.47 \pm 7.55$ nm for $A\beta_{1-42}$ oligomers. (B) Diameter histograms for inserted oligomers. Inserted $A\beta_{pE3-42}$ oligomers (blue) have a diameter $D_I(A\beta_{pE3-42}) = 26.00 \pm 7.08$ nm, whereas $D_I(A\beta_{1-42}) = 13.83 \pm 4.77$ nm for $A\beta_{1-42}$ oligomers (black). Diameters are given as widths of oligomer features at half maximum. (C) Height, h , histograms for membrane-adsorbed oligomers of $A\beta_{pE3-42}$ (blue) and $A\beta_{1-42}$ (black). $A\beta_{pE3-42}$ oligomers have a height $h_A(A\beta_{pE3-42}) = 5.67 \pm 1.48$ nm, while $h_A(A\beta_{1-42}) = 6.20 \pm 2.39$ nm for $A\beta_{1-42}$ oligomers. (D) Height histograms for inserted oligomers of $A\beta_{pE3-42}$ (blue) and $A\beta_{1-42}$ (black). $A\beta_{pE3-42}$ oligomers have a height $h_I(A\beta_{pE3-42}) = 1.38 \pm 0.24$ nm, while $h_I(A\beta_{1-42}) = 1.79 \pm 0.44$ nm for $A\beta_{1-42}$ oligomers. Histograms were fitted using a Gaussian function and D and h values are given as peak center value \pm HWHM of the distribution. A height of 2 nm was chosen as the boundary between inserted and adsorbed species. $N=20$ for all histograms, except $N=30$ for $D_I(A\beta_{1-42})$ and $h_I(A\beta_{1-42})$.

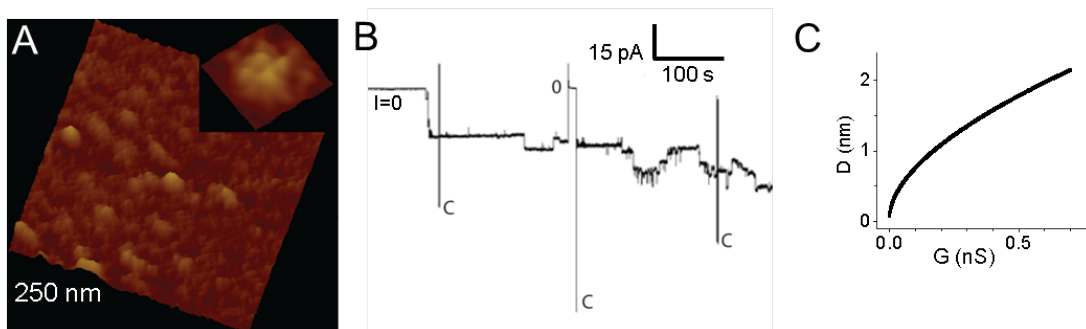


Figure 2.6: (A) AFM image of $A\beta_{pE3-42}$ oligomers inserted in a DOPS/POPE (1:1) membrane. A subpopulation of these oligomers forms pore structures. (B) Electrical recording data demonstrating the activity induced by $A\beta_{pE3-42}$ pore-forming oligomers. (C) Pore diameters estimated from eq. 2.1 for the interval of single pore conductances measured in our experiments (0 - 0.7 nS). (D) Exponential-like leakage current observed in the late stages of $A\beta_{pE3-42}$ -induced membrane permeability stemming from a superposition of discrete activity induced by $A\beta_{pE3-42}$ pore and continuous leakage current induced by globular oligomers.

Table 2.3: Comparison of pore diameters for $A\beta_{pE3-42}$, $A\beta_{1-42}$ and $A\beta_{17-42}$ obtained from eq. 2.3, MD simulations and AFM.

Peptide	Pore diameter (nm)	Method
Model equation	~ 1.1	Eq. 2.3
$A\beta_{pE3-42}$	~ 2.2 (18-mer, conformer 1) ~ 1.9 (18-mer, conformer 2)	MD [77]
$A\beta_{1-40}$	$\sim 1.0-2.0$	AFM [44]
$A\beta_{1-42}$	~ 1.9 (18-mer, conformer 1, D-isomer) ~ 2.1 (18-mer, conformer 2, D-isomer) $\sim 1.8-2.2$ (18-mer, conformer 1, L-isomer) $\sim 1.9-2.2$ (18-mer, conformer 2, L-isomer)	MD [64, 103, 88]
$A\beta_{17-42}$	$\sim 1.0-2.0$ ~ 1.7 (16-mer channel) $\sim 0.8, \sim 1.9, \sim 2.5-2.7$ (12-, 20-, 24-mer channels) $\sim 1.8, \sim 1.5, \sim 2.2$ (12-, 16-, 20-mer barrels)	AFM [89] MD [89] MD [14, 90] MD [92]

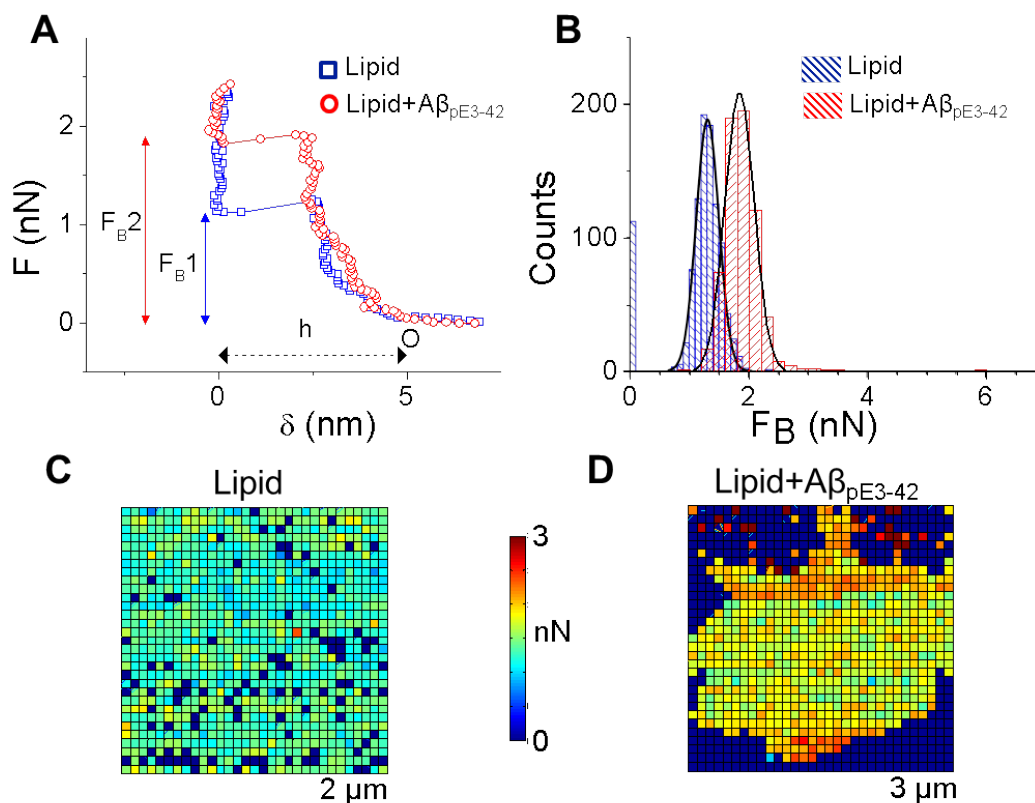


Figure 2.7: AFM force measurements demonstrating the effect of membrane-inserted Aβ_{pE3-42} oligomers on the mechanical properties of DOPS/POPE membranes. (A) Indentation curves (only approach is shown) for DOPS/POPE membranes without (black) and with (red) inserted Aβ_{pE3-42} oligomers displaying the breakthrough forces (F_B) and thickness (h) of the membranes. F is force and δ is tip-sample separation. (B) Histograms of breakthrough forces show $F_{B1} = 1.31 \pm 0.19$ nN for the DOPS/POPE membrane and $F_{B2} = 1.83 \pm 0.25$ nN for a similar membrane with inserted Aβ_{pE3-42} oligomers. (C) - (D). Force maps of the analyzed data for (C) the DOPS/POPE membrane and (D) the DOPS/POPE membrane with inserted Aβ_{pE3-42} oligomers. The outline of the membrane patch is seen in (C). A value of $F_B = 0$ was given to curves that did not show breakthrough forces outside the membrane. These curves were not analyzed any further.

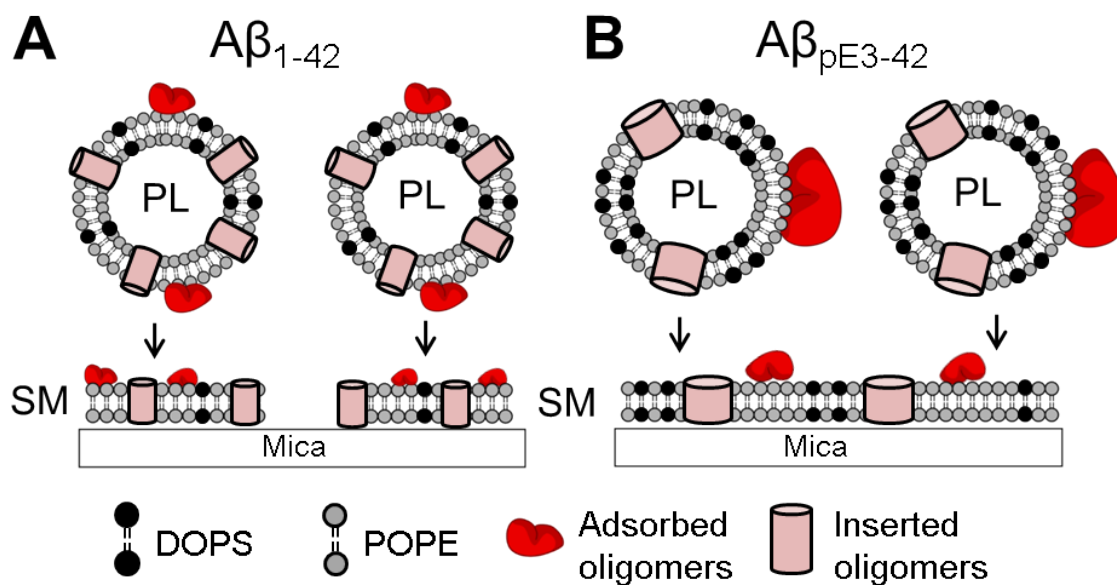


Figure 2.8: Schematics of supported membrane (SM) formation via proteoliposome (PL) rupture and fusion. (A) $A\beta_{1-42}$ proteoliposomes having a very high concentration of membrane inserted oligomers are not able to form supported membranes by fusion of ruptured proteoliposomes. (B) $A\beta_{pE3-42}$ proteoliposomes have lower concentrations of inserted oligomers, thus being able to form supported membranes. The dimensions of the inserted and adsorbed $A\beta_{pE3-42}$ oligomers are larger due to faster aggregation kinetics. Attractive interactions between $A\beta_{1-42}$ and PE head groups induce PE-rich proteoliposomes.

Chapter 3

Amyloid β ion channels in a membrane comprising of brain total lipid extracts

3.1 Abstract

Amyloid β ($A\beta$) oligomers are the predominant toxic species in the pathology of Alzheimer's disease. The prevailing mechanism for toxicity by $A\beta$ oligomers includes ionic homeostasis destabilization in neuronal cells by forming ion channels. These channel structures have been previously studied in model lipid bilayers. In order to gain further insight into the interaction of $A\beta$ oligomers with natural membrane compositions, we have examined the structures and conductivities of $A\beta$ oligomers in a membrane composed of brain total lipid extract (BTLE). We utilized two complementary techniques: atomic force microscopy (AFM) and black lipid membrane (BLM) electrical recording. Our results indicate that $A\beta_{1-42}$ forms ion channel structures in BTLE membranes, accompanied by a heterogeneous population of ionic current fluctuations. Notably, the observed current events generated by $A\beta_{1-42}$ peptides in BTLE membranes possess different characteristics

compared to current events generated by the presence of $A\beta_{1-42}$ in model membranes comprised of a 1:1 mixture of DOPS and POPE lipids. Oligomers of the truncated $A\beta$ fragment $A\beta_{17-42}$ (p3) exhibited similar ion conductivity behavior as $A\beta_{1-42}$ in BTLE membranes. However, the observed macroscopic ion flux across the BTLE membranes induced by $A\beta_{1-42}$ pores was larger than for p3 pores. Our analysis of structure and conductance of oligomeric $A\beta$ pores in a natural lipid membrane closely mimics the *in vivo* cellular environment suggesting that $A\beta$ pores could potentially accelerate the loss of ionic homeostasis and cellular abnormalities. Hence, these pore structures may serve as a target for drug development and therapeutic strategies for AD treatment.

3.2 Introduction

Alzheimer's disease (AD) is one of the most devastating neurodegenerative diseases. It is characterized by the progressive loss of memory and cognition. One of the pathological hallmarks of AD is the deposition of fibrillar amyloid plaques in the brains of AD patients.[104] Amyloid beta ($A\beta$) peptides, the major constituents of these plaques, are derived by enzymatic cleavage from the transmembrane amyloid precursor protein (APP); a process involving α -, β - and γ -secretases. The full length $A\beta_{1-40/42}$ is produced by cleavage of APP by β - and γ -secretases, and the smaller hydrophobic $A\beta_{17-42}$ (p3) fragment is produced by α - and γ -secretase APP cleavage.[37, 105, 91, 106]

Although accumulation of $A\beta$ plaques in AD brains was believed to be directly correlated to the disease, increasing evidence indicates that small $A\beta$ oligomers are the main toxic species.[7, 107] However, the exact disease mechanism has not yet been fully elucidated. A prevailing mechanism of AD pathology postulates that $A\beta$ oligomers negatively affect neuronal function and survival by forming ion permeable pores, resulting in the

destabilization of cell ionic homeostasis.[108, 17, 44, 109, 110] This hypothesis is supported by data from several experimental techniques and molecular dynamics (MD) simulations studying A β -induced permeability of ions across model lipid membranes.[17, 44, 45, 14], as well as an "optical patch clamp" method whereby total internal reflection fluorescence (TIRF) microscopy data revealed the presence of localized Ca²⁺ transients during cellular influx across *Xenopus* oocyte membranes.[111]

The p3 fragment represents an additional source of toxicity from APP processing that contributes to neuronal cell death.[91, 112] It was shown that A β _{22–35} peptides induce specific increases of Ca²⁺ levels in neural cells; these effects of A β oligomers on cellular Ca²⁺ influx could be inhibited by zinc ions.[113] We have previously shown that the p3 and A β _{9–42} (N9) fragments form pores in black lipid membrane and permeabilize the membranes of neuronal cells.[91, 51]

The structure and function of these Ca²⁺-flux inducing A β pores have been primarily studied using *in vitro* techniques. Atomic force microscopy (AFM) and Electron microscopy (EM) have been the most frequently utilized imaging techniques for examining the structure of A β pores in model membranes because of their high-resolution capabilities.[17, 114, 43] AFM images of A β oligomers reconstituted in model lipid bilayers show pore-like structures with outer pore diameters of 8-12 nm.[67, 21, 115] Electrical recording data obtained for various A β oligomers in suspended lipid membranes (also called black lipid membranes or BLM) display the heterogeneous multiple conductances characteristic of A β and all amyloid peptides studied to date.[14, 79] These current fluctuations show weak cation selectivity, voltage independence, inhibition by Congo red, and reversible blockage by Zn²⁺ ions,[44, 116, 117] Previously, we compared the pore activities and structures of A β _{1–42} and A β _{pE3–42} in anionic lipid membrane comprised of DOPS/POPE (1:1, wt/wt).[115, 79]

Because of the post translational cleavage of amino acid residues 1 (Asp) and 2 (Ala), (of which amino acid 1 is a negatively charged residue at neutral pH), and modification of the 3 (Glu) residue to the hydrophobic pyroglutamate (pE), $A\beta_{pE3-42}$ oligomeric subunits are more hydrophobic and more stable in the membrane allowing larger transient pore structures to form than for $A\beta_{1-42}$ pores, resulting in larger ion conductance of $A\beta_{pE3-42}$ pores.[79]

Most of these previous studies were conducted in model lipid membranes, not thoroughly displaying all of the structural complexities of a mixture of lipids found in natural cellular membranes. Cell membranes contain various lipids that work cooperatively in specialized domains.[1] AD brains have been shown to contain an increased fraction of anionic lipids such as phosphatidylserine (PS) and phosphatidylglycerol (PG) compared to the brains of cognitively normal patients, while the percentage of neutral lipids like phosphatidylcholine (PC) remains similar.[118] Also, anionic lipids, but not neutral lipids, show dose dependent increase in cation influx by $A\beta$ peptides[119] and the pore activity in anionic lipid membranes was decreased when cholesterol was introduced.[15, 120] These findings suggest the possible role of negatively charged lipids in permeability induced by $A\beta$ peptides. Our prior work in this field has focused primarily on DOPS/POPE membranes as an extreme model of the anionic lipid membrane found in progressed AD patients. To better simulate the initial pathogenesis of AD, here we used a membrane comprised of natural brain total lipid extracts (BTLE) which is considered to be the closest mimic of the healthy (or very early AD stage) neuronal membrane.[121] In the present study, we study the structures and ion conducting of $A\beta$ peptides in BTLE membranes. We utilize two complementary techniques, AFM, and BLM electrical recordings, to identify and characterize the biophysical properties of $A\beta_{1-42}$ pore formation and examined the structure and ion conducting properties of $A\beta$ pores in BTLE membranes and compared with the anionic DOPS/POPE (1:1, wt/wt)

membranes. Our AFM images reveal pore-like structures for the A β_{1-42} peptides in both BTLE and DOPS/POPE membranes. Interestingly, the ion conducting activity of A β_{1-42} in BTLE membranes exhibit notable differences when compared with the ion conducting properties of these peptides in DOPS/POPE membranes. We observed similar difference in the ion conducting behavior of p3 peptides when incorporated in BTLE vs. DOPS/POPE membranes. These studies reveal that both full-length A β and its non-amyloidogenic p3 fragment form pores in natural BTLE membranes, suggesting that both peptides have the capability to alter neuronal cell homeostasis and play toxic roles in AD.

3.3 Results and Discussion

3.3.1 Interaction with BTLE or DOPS/POPE liposomes facilitate the self-assembly behavior of A β

Thioflavin T (ThT) molecules are often used to monitor the self-assembly kinetics of A β , as ThT molecules show enhanced fluorescence intensity upon binding to β sheet structures in amyloid fibrils.[122, 123] Here, we used ThT fluorescence to monitor the self-assembly kinetics of A β_{1-42} in the presence of liposomes comprised of DOPS/POPE (1:1, wt/wt) or BTLE.(Figure 3.1) We examined the effect of anionic lipid (DOPS) which is one of the major known compositions of BTLE on A β_{1-42} self-assembly although the structural identity of $\sim 60\%$ of the lipids in BTLE samples is unknown.(Table 3.1) All ThT fluorescence traces show a sigmoidal trend indicating a growth of β sheet containing fibril structures.[124, 66, 125] At the initiation of each experiment, we observed low ThT intensity, indicating the absence of noticeable β -sheet structures. This low initial intensity remained approximately constant for the first few hours, and only a slight increase in ThT

fluorescence was observed during this period. In this phase, known as the lag phase time (t_{lag}), monomers aggregate into small oligomers to form nucleates or seeds.[66, 87] The ThT intensity then rapidly increased as small A β oligomers elongated into fibrils and the fluorescence reached the final equilibrium phase. Notably, A β_{1-42} started self-assembly faster when either BTLE (red circle) or DOPS/POPE (blue square) liposomes were present in the solution compared to observed aggregation kinetics of A β_{1-42} in lipid-free solution (dark blue triangle). These results indicate that the presence of a membrane surface plays an important role in self-assembly of A β_{1-42} .

The observed time-course of ThT fluorescence curves were background corrected by subtracting the ThT fluorescence curve without A β_{1-42} for A β_{1-42} in lipid-free solution or ThT fluorescence curve with the liposomes (either BTLE or DOPS/POPE) in solution for A β_{1-42} with the liposomes, respectively and were fitted using eq. (3.1).[115, 66]

$$F = F_0 + \frac{a}{1 + e^{-k(t-t_{ht})}} \quad (3.1)$$

where t is time, t_{ht} is the time it takes to get half-maximal ThT fluorescence, F_0 is the initial ThT fluorescence intensity, a is the amplitude of the highest intensity, and k is the rate constant. The lag phase time (t_{lag}) was calculated from the fitting parameters obtained above using eq. 3.2.

$$t_{lag} = t_{ht} - \frac{2}{k} \quad (3.2)$$

From the fitted curves (black solid lines) in Figure 3.1, we obtained a t_{lag} of 8.4 ± 0.3 h for A β_{1-42} with BTLE liposomes, 11.3 ± 0.5 h for A β_{1-42} with DOPS/POPE, and 19.7 ± 3.4 h for A β_{1-42} alone. The shortest observed t_{lag} for A β_{1-42} aggregation was in

BTLE membranes suggesting that the mixture of various lipids present in BTLE might increase the speed of the formation of seeds. The low ThT fluorescence intensity at this initial phase of the aggregation process suggests that there are very few protofibril species in solution. Previous reports from AFM experiments reveal small globular shape of A β oligomers[115, 126] and from structural NMR experiments of A β ₁₋₄₀ in this phase reveals a partially folded structure forming a 3₁₀ helix[84] and the presence of oligomers containing α -helix and reversible β -sheet structures.[83]

Although the observed t_{lag} for A β ₁₋₄₂ was shortest in the presence of BTLE liposomes, the aggregation rate constant (k) of A β ₁₋₄₂ with DOPS/POPE ($1.1 \pm 0.1 \text{ h}^{-1}$) was faster than A β ₁₋₄₂ with BTLE ($0.8 \pm 0.1 \text{ h}^{-1}$) or A β ₁₋₄₂ alone ($0.3 \pm 0.1 \text{ h}^{-1}$). These results suggest that A β ₁₋₄₂ peptides prefer more to form seeds with BTLE than to elongate into fibrils compared to the seeds formed with DOPS/POPE. As small oligomeric A β species are found to play a more prominent role in AD neuropathology[39, 41] than e.g., A β fibrils, the structure of these oligomeric species in the lipid membranes and the electrophysiological activities were studied using AFM and BLM.

3.3.2 Distribution of A β ₁₋₄₂ oligomer structures on DOPS/POPE and BTLE membranes

We employed AFM to study the pore-like structures and surface interactions of A β ₁₋₄₂ oligomers in BTLE and DOPS/POPE (1:1, wt/wt) membranes. As a control, intact BTLE membranes that were not exposed to A β ₁₋₄₂ oligomers were imaged. The untreated membrane (bright region, Figure 3.2A) had a flat and smooth surface with a bilayer thickness of $\sim 5.4 \text{ nm}$, in agreement with previous reports on the thickness of DOPS/POPE membrane ($\sim 5 \text{ nm}$).[115] When A β ₁₋₄₂ oligomers were reconstituted at 1:20 peptide to lipid mass ratio

in a BTLE membrane, we observed a large population of small annular objects protruding 1 - 2 nm out of the plane of the membrane (Figure 3.2B). Structures containing features that protrude < 1.5 nm protruding outside of the plane of the membrane were interpreted to be A β oligomers inserted in the membrane. Their surface density was estimated to be 300 - 500 oligomers/ μm^2 and the majority of these structures had measured diameters between 10 - 20 nm (Figure 3.2B). Two predominant subpopulations of oligomers with diameters centered around 12 nm and 16.5 nm were observed. One of these subpopulations centered around 12 nm displayed pore-like structures (inset, Figure 3.2B), comparable to those previously observed with A β oligomers inserted into synthetic lipid.[17, 17, 44, 21, 14]. In addition, we observed another minor subpopulation of larger oligomers partitioned on the bilayer surface with heights of 3 - 4 nm above the membrane plane. In DOPS/POPE membranes, A β_{1-42} oligomers were populated with a heights ranging from 1 - 5 nm outside the membrane plane, and a diameters ranging from 10 - 45 nm (Figure 3.2C). We found that the density of A β_{1-42} oligomers was lower in DOPS/POPE membranes compared to BTLE membranes, although more of larger oligomers were present in DOPS/POPE membranes. This result suggests that more oligomers interact with the surfaces of BTLE membranes than to membranes comprised of DOPS/POPE and might possibly be responsible for shorter t_{lag} for A β_{1-42} with BTLE liposomes.

3.3.3 Pore structures of A β_{1-42} in BTLE and DOPS/POPE membranes

Computational studies can provide predictions of membrane-bound conformations of the A β pores with atomic-level detail. Anionic DOPS/POPE (1:2 molar ratio) lipid membranes were used to simulate the pore structure of A β_{1-42} . We modeled A β_{1-42} pores in a β -barrel topology using two A β_{1-42} conformers with the β -strand-turn- β -strand motif

in a similar manner as we reported in previous computational studies.[21, 127, 58] Explicit MD simulations on $A\beta_{1-42}$ barrels embedded in the DOPS/POPE membrane provided fully relaxed pore conformations in the lipid environment.[127] For the 18-mer barrels, the calculated averaged pore diameter and the maximum pore height across the bilayer are ~ 7.9 and ~ 6.9 nm for the conformer 1, and ~ 8.0 and ~ 6.8 nm for the conformer 2 barrels (Figure 3.3A). The lateral pore diameter depends on the number of $A\beta$ monomers involved in the pore, suggesting that large sizes of pore might be possible with a large number of $A\beta$ subunits. However, the pore height across the membrane is almost the same among the different computed conformers, since each conformer contains a distinct turn region. The longer heights of the $A\beta_{1-42}$ barrels compared to the bilayer thickness of ~ 5 nm suggest that both sides of the full-length $A\beta$ pores protrude from the membrane surface (Figure 3.3A).

The MD models of the $A\beta_{1-42}$ pores show that the N-terminus of $A\beta_{1-42}$ extends approximately 1-1.5 nm outside of the plane of the DOPS/POPE bilayer, while the turn region at the other bilayer leaflet only protrudes less than 0.5 nm (lateral view in Figure 3.3A). The calculated extensions of the N-terminus of $A\beta_{1-42}$ protruding out of the membrane in $A\beta_{1-42}$ oligomers agree well with the measured pore heights by AFM (Figure 3.2B and Figure 3.3C).

Among these oligomer structures imaged by AFM, well-defined $A\beta_{1-42}$ pore structures were observed in both BLTE and DOPS/POPE membranes (Figure 3.2 and Figure 3.3). The quality of AFM images can often vary among different samples due to tip degradation, but high resolution imaging, when achieved, still revealed that pore structures are usually composed of 4 to 5 subunits of $A\beta_{1-42}$ oligomers and that the outer diameters of pore structures are comparable to each other with the average diameters of 11.4 ± 1.5 nm ($n =$

11) in BTLE membrane and 13.9 ± 2.5 nm ($n = 12$) in DOPS/POPE membrane, and these dimensions are comparable to the previous results found in other lipid membranes (Figure 3.3B and Figure 3.3C).[91, 17, 44, 21]

3.3.4 Ion Conducting Activity of $A\beta_{1-42}$ in DOPS/POPE and BTLE membranes

We examined the ion conducting activity of $A\beta_{1-42}$ in BTLE and model DOPS/POPE (1:1, wt/wt) lipid membranes, using a BLM electrical recording setup.[17, 17, 44, 128] Upon addition of $A\beta_{1-42}$ into the recording electrolyte solution, we observed a heterogeneous population of ion current fluctuations by recording current vs. time traces under a constant applied potential of 100 mV (Figure 3.4), consistent with the formation of $A\beta_{1-42}$ oligomer-icpores of varying size.[129] These transient ion conducting events can be categorized into three types; bursts, steps and spikes.[79] We observed mostly burst-like activities in the current vs. time traces of $A\beta_{1-42}$ in the BTLE membrane (Figure 3.1A and Figure 3.4B). Notably, the observed frequency of burst-like events was lower in DOPS/POPE membranes compared to the frequency of bursts in BTLE membranes, while the frequency of well-defined, step-wise current events typically characteristic of ion channels was more pronounced in DOPS/POPE membranes (Figure 3.4C). Based on these observations of the ion conducting activity of $A\beta_{1-42}$ in the two different types of lipid membranes, we hypothesized that the ion conducting properties of $A\beta$ oligomers is dependent on the composition of lipid head groups that could influence the observed populations of ionic bursts, steps or spikes across membranes. To support this hypothesis, we examined the ion conducting properties of p3 ($A\beta_{17-42}$), which is a truncated version of $A\beta_{1-42}$ losing many charged amino acid residues that are putatively responsible for interactions with lipid head groups.

Similar to the observations with full length $A\beta_{1-42}$ peptides, heterogeneous, burst-like features were dominantly present when p3 was incubated with BTLE membranes, while mostly step-like current events were found when p3 was incubated with DOPS/POPE membranes (Figs. 3.71A and 1C). These results support that the electrophysiological characteristics of $A\beta$ oligomers in lipid membranes could be more dependent on lipid compositions rather than peptide sequence. In order to confirm the observed ion conductance across membranes in the BLM experiments was due to the presence of $A\beta_{1-42}$ oligomers, we added Zn^{2+} ions to the recording electrolyte; Zn^{2+} is known to inhibit the ion conducting properties of $A\beta$ in membranes.[129] Upon addition of Zn^{2+} ions into the *cis* chamber of the bilayer setup, the macroscopic conductance of $A\beta_{1-42}$ oligomers decreased gradually and disappeared completely within 5 min in both BTLE and DOPS/POPE membranes (Figure 3.1B and Figure 3.4D). The conductance of p3 peptides in membranes was also blocked by Zn^{2+} ions in both BTLE and DOPS/POPE membranes (Figs. 3.7B and D). We also qualitatively observed that the p3 pore activity appeared faster than for $A\beta_{1-42}$ in most of the experiments using BTLE or DOPS/POPE membranes, perhaps suggesting faster kinetics of insertion and pore formation for p3 in membranes although more experiments would be needed to validate the observation.

We further examined the differences in amplitudes of ion influx through $A\beta_{1-42}$ and p3 pores in BTLE and DOPS/POPE membranes. The amplitudes of ion influx was calculated by dividing each observed current from step and burst events by the applied voltage (Figure 3.5). Observed amplitude of ion flux values through $A\beta_{1-42}$ ranged between 5-200 pS in BTLE membrane and 5 - 300 pS in DOPS/POPE membrane (Figure 3.5A and Figure 3.5C). In the case of p3, these values varied from 5 - 140 pS in BTLE membrane and 5 - 320 pS in DOPS/POPE membranes (Figure 3.5B and Figure 3.5D). The distribution

of peaks in both membranes appeared mostly between 10 - 30 pS. However, both $A\beta_{1-42}$ and p3 oligomers in DOPS/POPE membranes exhibited a higher fraction of current events with conductance above 150 pS (Figure 3.5C and Figure 3.5D inset) compared to their conductance properties in BTLE membranes. In addition, we analyzed macroscopic ionic flux across the membranes through $A\beta_{1-42}$ and p3 pores by integrating the current traces (i.e., providing an estimate for the total transported charge, Q (C) over a time period of 5 min ($n \geq 3$) for both BTLE and DOPS/POPE membranes (Figure 3.6). The total transported charge of $A\beta_{1-42}$ and p3 peptides in BTLE and DOPS/POPE membranes is significantly different ($p = 0.028$) as concluded from a two way ANOVA test. The contribution of peptides or the interaction of both peptides and membranes was found to be insignificant ($p = 0.883$ and $p = 0.614$, respectively) as compared to the contribution from membrane types. We observed a 3-fold increase in the average macroscopic ion flux for $A\beta_{1-42}$ in DOPS/POPE membranes compared to the flux of ion through $A\beta_{1-42}$ oligomers across BTLE membranes and a 10-fold increase was observed in the average total transported charge through p3 oligomers in DOPS/POPE membranes compared to BTLE membranes over the same window of time. The average values for the total transported charges over a 5 minute time window were 3.0×10^6 C for $A\beta_{1-42}$ and 1.4×10^6 C for p3 in BTLE membranes, whereas these values were 7.8×10^6 C for $A\beta_{1-42}$ and 9.7×10^6 C for p3 in DOPS/POPE membranes (Figure 3.6).

The interaction of $A\beta_{1-42}$ with BTLE and DOPS/POPE membranes differs considerably in BLM electrical recording (Figure 3.4). Current vs. time traces of $A\beta_{1-42}$ in BTLE membrane show mostly burst-like activities. These results suggest that pores with varying dimensions and subunit composition are active in the membranes. This observation is consistent with the multilevel current events observed for various amyloid pores.[91, 44]

Previously, we have reported that conductance of $A\beta_{1-42}$ oligomers pores ranged between 30 - 360 pS in DOPS/POPE (1:1) lipid membranes, with 90% of these current events exhibiting a conductance value of ~ 33 pS.[79]. Even higher conductance (on the order of 1 nS) have been reported for $A\beta_{1-42}$ oligomers in membranes composed of POPE and PS lipid mixtures.[14, 89] Current vs. time traces of $A\beta_{1-42}$ display burst-like events as well as step-wise current events in DOPS/POPE membranes (Figure 3.4C). The conductance of $A\beta_{1-42}$ in both of these types of membranes was seen slightly smaller than the previously reported values.

Although it is impractical to study the contribution of each individual lipid components in the BTLE membrane on $A\beta_{1-42}$ pore activity, one potential difference between BTLE and model lipid membranes used for the characterization of $A\beta$ oligomeric pores is the dominance of negatively charged phosphatidylserine (PS) group. PS lipids are one of the major known constituents of BTLE (10.6%, wt/wt) but still less than DOPS/POPE (1:1, wt/wt) lipids. AD brains have higher fraction of PS lipids compared to the brains of cognitively normal, suggesting a possible role of negatively charged lipids in AD pathology.[65, 130, 131] We observed a higher frequency of channel-like transmembrane current events from $A\beta_{1-42}$ oligomers in DOPS/POPE membranes compared to the ion transport activity of this peptide in BTLE lipid bilayers (Figure 3.4).

In addition, the frequency of burst-like ion conducting events from $A\beta$ pores in BTLE membranes was lower than in DOPS/POPE membranes. These observations could arise from a variety of reasons. First, different interactions of $A\beta_{1-42}$ peptides with the lipid head groups could affect the current events. Second, there are potential differences in phase transition temperature (T_m) of the lipids within the membranes. For example, the T_m of POPE lipid is 24 °C while the T_m of BTLE is not known. Additionally, low stability

of the pore structures in BTLE membranes could shorten the life time of the activities and cause an overlap between current events. To shed some light on a possible cause for the different conductance properties of $A\beta_{1-42}$ oligomers in different membranes, we examined the transmembrane ion transport properties of p3 peptides in both BTLE and DOPS/POPE lipid membranes. Since the charged residues of $A\beta_{1-42}$ that can interact with the head groups of the lipids are mostly located in the N-terminal region of $A\beta_{1-42}$, p3, as a truncated version of $A\beta_{1-42}$, can reveal if the interaction of the N-terminal region of full length $A\beta_{1-42}$ with the lipid headgroups can affect the ion conducting characteristics of $A\beta_{1-42}$ in membranes. We observed a trend of more burst-like current events with p3 peptides in BTLE membranes, whereas we observed more step-like current events of this peptide in DOPS/POPE membranes (Figure 3.7). We observed that current events from p3 peptides in DOPS/POPE appeared less step-wise than the current events observed for $A\beta_{1-42}$. The effect of T_m of POPE on current events was also inspected by replacing the POPE in DOPS/POPE membrane with 1, 2-dioleoyl-sn-glycero-3-phosphoethanolamine (DOPE) (to form DOPS/DOPE membranes), which has a T_m of -16°C . The ion conducting properties of $A\beta_{1-42}$ in DOPS/DOPE (1:1, wt/wt) membranes show comparable step-like channel events to the ion conducting properties of $A\beta_{1-42}$ in DOPS/POPE (1:1, wt/wt) membranes, suggesting that T_m of the lipid does not influence the formation of step-like current fluctuations of $A\beta_{1-42}$ in membranes (Figure 3.8).

We hypothesize that the presence of $A\beta$ oligomeric pores with higher conductance values in DOPS/POPE membranes compared to BTLE membranes may imply that $A\beta$ oligomers could have an increased detrimental effects in patients with AD compared to healthy patients, as DOPS/POPE membranes contain higher percentages of PS lipids than BTLE membranes, potentially mimicking an important difference between the lipid com-

positions in diseased vs. healthy brains. The BTLE membranes used here contains only 10.6% PS (Table 3.1), potentially representing a model for healthy brains. Thus, $A\beta_{1-42}$ oligomers in BTLE membranes displayed more heterogeneous current events, lower average amplitudes of conductance for individual ion fluctuations, and reduced macroscopic ion flux compared to the conductance properties of this peptide in DOPS/POPE membranes. Previous studies showed that $A\beta_{25-35}$ (a neurotoxic fragment of $A\beta_{1-42}$) could form ion conducting pores in membranes derived from a total brain lipid extract. However, in a lipid membrane extracted from soybeans,[15] cholesterol in the membrane was shown to inhibit formation of ion conducting $A\beta_{25-35}$ pores[15], and this finding with cholesterol was replicated with the inhibition of the formation of ion conducting $A\beta_{1-42}$ oligomers in cellular membranes.[110, 132] Anionic lipids have previously been suggested to promote the formation of ion conducting $A\beta$ oligomeric pores.[119, 15] The membrane disruption was shown to follow a two step mechanism with the initial formation of pores and non-specific membrane fragmentation.[63, 56] The present findings are consistent with these previous results, and suggest that lipids derived from brains provide a relatively unfavorable environment for the formation of $A\beta$ pores, but still permit their formation under some conditions. This is unsurprising given the late development and slow progression of sporadic AD cases. However, we have shown that $A\beta$ pore formation is possible in BTLE membranes providing a viable mechanism of early stage AD pathology. As lipid composition shifts to more anionic head groups during disease progression, this effect would only be intensified as demonstrated by the current events of $A\beta$ oligomers in DOPS/POPE membranes. Although further investigation of $A\beta$ oligomer structures in various lipid compositions using more detailed structural techniques, including NMR or EPR, would be helpful to characterize the effects of lipid headgroups on $A\beta$ aggregation, the results reported here suggest that regions

containing high fractions of anionic lipids (especially with PS head groups) could provide a favorable environment promoting the formation and insertion of A β pores in membranes.

3.4 Conclusions

We have investigated the structures, ion conducting properties, and self-assembly kinetics of the full-length A β_{1-42} peptide in lipid bilayers composed of brain total lipid extract (BTLE) and a model lipid mixture comprised of 1:1 (wt/wt) DOPS/POPE. A β_{1-42} peptides aggregate faster when BTLE or DOPS/POPE liposomes were present in solution. A β_{1-42} oligomers insert into both type of the membranes, forming ion-conducting pore structures that can be blocked by Zn²⁺ ions. However, the ion conducting properties of A β_{1-42} oligomers, as well as the distribution of subpopulations of membrane-associated oligomers differ as a function of lipid composition. The presence of heterogeneous bursts of ion fluctuations was observed for A β_{1-42} in BTLE membranes, which may reflect a heterogeneous population of sizes of pore-like structures found when this peptide was reconstituted in BTLE membranes. Conversely, A β_{1-42} in DOPS/POPE membranes reveal more step-wise current events, which could reflect the presence of a different heterogeneous population of oligomeric pores found in DOPS/POPE membranes by AFM. Additionally, to examine the effect of interactions of the N-terminal residues of A β_{1-42} with the membrane surface on ion conducting properties, we observed similar trends of burst-like current events in BTLE membranes and more step-wise current events in DOPS/POPE membranes for p3 peptides (which lacked the charged N-terminal residues present in full length A β). While additional molecular details for the formation of A β_{1-42} in BTLE membranes remains to be established, both full-length A β peptides and its non-amyloidogenic p3 fragment form pores in BTLE membranes, suggesting that both A β peptides have the capability to alter neuronal

cell homeostasis and play toxic roles in the brain. Hence, these oligomeric A β structures could serve as specific targets for the development of therapeutic strategies for the treatment AD.

3.5 Materials and Methods

3.5.1 Peptide preparation

All A β_{1-42} and A β_{17-42} had >90% purity as provided by the manufacturer (Anaspec, CA and rPeptide, GA). The initial powders were first dissolved in 1% ammonium hydroxide until the peptides were completely dissolved. They were subsequently sonicated for approximately 2 min. The desired amount of peptide was then aliquoted and lyophilized using a lyophilizer (FreeZone 2.5 Plus, Labconco, Kansas City, KS). The aliquots were stored at -80 °C for a maximum of 3 months until they were used. For each experiment, aliquoted peptides were taken from -80 °C and dissolved first in 10 mM NaOH and diluted with 10 mM HEPES (1 mM MgCl₂, 150 mM KCl, pH = 7.4) buffer solutions to make final concentration of 100 μ M. Percentage of NaOH in the solution never exceeds more than 10% and the pH was changed less than 1%. The peptide concentration was measured using the 280 nm UV absorbance (extinction coefficient: $\epsilon = 1490 \text{ M}^{-1} \text{ cm}^{-1}$).

3.5.2 Thioflavin T Assays

ThT assay was conducted as previously described.[115] Briefly, 10 μ M ThT solution was prepared using 10 mM HEPES (1 mM MgCl₂, 150 mM KCl, pH = 7.4) buffer in 96-well white-walled plates (Nunc). Using 10 mM NaOH, lyophilized peptide was dissolved to prevent aggregation. The peptide solution was then diluted with the HEPES buffer to its final

peptide concentration of 10 μ M in the plate well. For monitoring the effect of liposomes in A β self-assembly, 0.2 mg/ml liposomes of BTLE and DOS/POPE (1:1, wt/wt) were prepared by extrusion method using a 100 nm membrane filter and the either BTLE or DOPS/POPE liposomes were added instead of the buffer in the well. The NaOH content was maintained at <10% of the total volume. ThT fluorescence (450 nm excitation, 490 nm emission) was monitored every 5 min at 25 °C for the indicated times using a SPECTRAMax Gemini EM fluorescent plate reader (Molecular Devices, Sunnyvale, CA).

3.5.3 Proteoliposome preparation for AFM imaging

For preparation of supported lipid bilayers, 40 μ L of brain total lipid extract (BTLE), DOPS/ POPE (1:1, wt/wt), or DOPS/DOPE (1:1, wt/wt) lipids (Avanti Polar Lipids, AL) in chloroform was first added to a clean 2.5 mL vial. Chloroform was evaporated using a vacuum pump or a rotary evaporator to produce a lipid film. The dried lipid film was hydrated for an hour with 10 mM HEPES (1 mM MgCl₂, 150 mM KCl, pH = 7.4) buffer to a final concentration of 0.1~0.5 mg/ml at 25 °C under occasional vortexing. Finally, the liposome solutions were sonicated for 5 min and stored in a 4 °C until used. To achieve high insertions of A β ₁₋₄₂ or p3 peptides in BTLE or DOPS/POPE membranes, lipids were hydrated in HEPES buffer containing 0.5-1 mg/mL peptide concentrations. They were vortexed vigorously for 30 min at 5 minute intervals and subsequently sonicated for 5 min in an ice bath. The peptide to lipid mass ratios of 1:20 for A β ₁₋₄₂ and 1:7 for p3 were used. For AFM imaging, ~10 μ l of the sample solution was deposited on freshly cleaved mica and incubated for ~1-3 min to form supported lipid bilayers by vesicle rupture on the mica surface. After incubation, samples were rinsed with the buffer to remove unruptured liposomes in the solution. Topographic images A β ₁₋₄₂ and p3 in BTLE or DOPS/POPE

membranes were acquired using a Multimode AFM equipped with a Nanoscope V controller (Bruker, Santa Barbara, CA). Silicon nitride cantilevers with a nominal spring constant of 0.08 N/m (TR400PSA, Asylum research) were employed using regular tapping mode as well as peak-force tapping. The Nanoscope software was used for analyzing imaging data.

3.5.4 Formation of Planar Lipid Bilayers for BLM experiments

We formed planar lipid bilayers by the “painting method” over a 250 μm aperture in a Delrin cup (Warner Instruments, 1 ml volume).[133] This aperture was first pretreated with $\sim 2 \mu\text{l}$ of 20 mg/ml BTLE lipid solution in hexane. Following pretreatment, a solution of 10 mM HEPES, 150 mM KCl, 1 mM MgCl_2 , pH 7.0 (recording solution) was added to both chambers. Subsequently, 20 mg/ml solution of BTLE lipid in n-decane was added over the aperture using a fine tip paint brush until a bilayer was formed. During this process, the capacitance of the bilayer was monitored to check the thinning of the lipid and decane droplet. If the droplet did not thin spontaneously, we applied air-bubbles using a micron pipet under the pore to facilitate the thinning of the lipid-decane droplet. When the lipid bilayer was stable for more than 30 minutes within ± 100 mV applied potential and the capacitance of the bilayer was above 130 pF, we added 11-22 μM of $\text{A}\beta_{1-42}$ or p3 directly into the chamber. The chamber was stirred with a stirring bar by using Stir-2 stir plate (Warner Instruments) for 5 minutes to help $\text{A}\beta$ peptides access the lipid bilayer easily.

3.5.5 BLM Measurements of $\text{A}\beta$ s

We performed channel activity recordings in “Voltage clamp mode” using Ag/AgCl electrodes (Warner Instruments) immersed in each chamber. Data acquisition and storage were carried out using custom made LabVIEW software in combination with a BC-535

patch clamp amplifier (Warner Instruments, set at a gain of 10 mV/pA and a filter cutoff frequency of 3 kHz). The data were acquired at a sampling frequency of 15 kHz using a data acquisition board (National Instruments) connected to the amplifier. We conducted filtering using a digital Gaussian low-pass filter (cutoff frequency of 50 Hz) by ClampFit 9.2 software (Axon Instruments). All experiments were conducted for 60-80 minutes after adding the corresponding peptide solution. For channel blockage experiments, a final concentration of 2 mM ZnCl₂ solution was added to one side of the chamber. We analyzed the ion influx through Aβ₁₋₄₂ and p3 peptides by integrating the current (over t = 5 min) in current vs. time traces to characterize the heterogeneous conductances of both the peptides. This area represents the total transported charge during the chosen time interval.

$$\text{Total transported charge, } Q = \int_{t=0}^{t=5 \text{ min}} I(t) dt \quad (3.3)$$

We used this equation to characterize Aβ₁₋₄₂ and p3 pore-like structures.

A two way ANOVA test with the membrane types and peptide types as two independent variables and total transported charges as the dependent variable was carried out to account for the contributions of the membranes, peptides, or interaction of both.

Before introducing any Aβ peptides into the BLM cup, we monitored that the electrical current traces did not display leakage currents. The capacitance of the membrane was monitored occasionally to check the stability of the membrane. Aβ peptides were only introduced in the membrane when the capacitance was higher than 130 pF and stable at least for 30 min. We also confirmed the pore activities by changing the polarity from 100 mV to -100 mV and confirming that the measured ionic currents changed accordingly during the activity recording.

3.6 Acknowledgements

Chapter 3, in part, is a reprint of the material as it appears in Lee, J.; Kim, Y. H.; T. Arce, F.; Gillman, A. L.; Jang, H.; Kagan, B. L.; Nussinov, R.; Yang, J.; Lal, R. Amyloid Ion Channels in a Membrane Comprising Brain Total Lipid Extracts. *ACS Chem. Neurosci.* **2017**, acschemneuro.7b00006. The dissertation author was the primary author of this paper.

All simulations had been performed using the high-performance computational facilities of the Biowulf PC/Linux cluster at the National Institutes of Health, Bethesda, MD (<http://biowulf.nih.gov>). We would like to acknowledge Abhijith G Karkisaval for help with the statistical analysis. This project was supported by the National Institute on Aging of National Institutes of Health (Grant AG028709). Y.H.K and J.Y. acknowledge support from the Air Force Office of Scientific Research (FA9550-12-1-0435) and from the National Institute on Aging of the National Institutes of Health under Award Number R01AG053577. The fund from Frontier Innovation Scholars Program in UCSD supported to J.L. This project has been funded in whole or in part with Federal funds from the Frederick National Laboratory for Cancer Research, National Institutes of Health, under contract HHSN261200800001E. This research was supported [in part] by the Intramural Research Program of NIH, Frederick National Lab, Center for Cancer Research. The content of this publication does not necessarily reflect the views or policies of the Department of Health and Human Services, nor does mention of trade names, commercial products or organizations imply endorsement by the US Government.

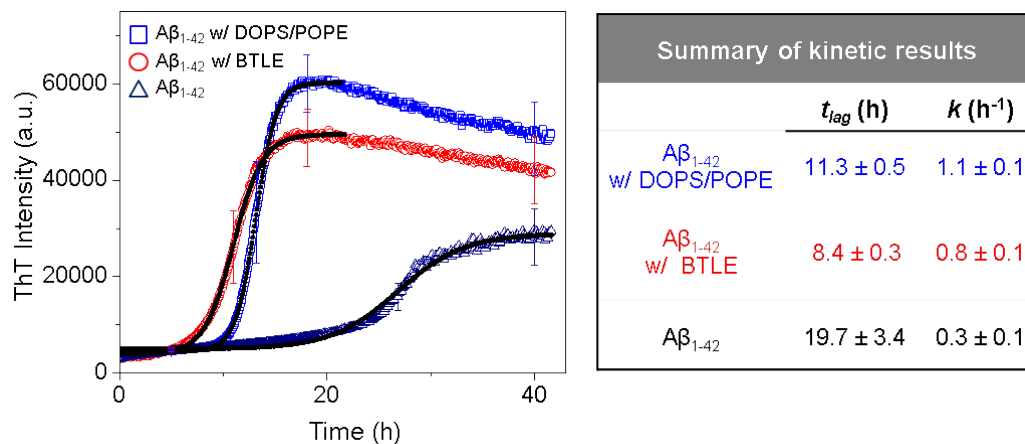


Figure 3.1: Self-assembly of $A\beta_{1-42}$ in the presence of BTLE and DOPS/POPE (1:1, wt/wt) liposomes monitored by ThT fluorescence. ThT fluorescence intensity of $A\beta_{1-42}$ in the presence of DOPS/POPE (blue square) or BTLE (red circle) increased faster than the ThT fluorescence intensity of $A\beta_{1-42}$ alone (dark blue triangle). t_{lag} and k were obtained by fitting the data from ThT fluorescence using eq. 3.1 (given in the Materials and Methods section). ThT fluorescence was measured every 5 min at 25 °C after stirring for 2 sec. In these experiments, a 10 μ M solution of $A\beta_{1-42}$ was incubated with or without BTLE or DOPS/POPE liposomes in 10 mM HEPES (150 mM KCl, 1 mM MgCl₂) buffer. The data represent an average from 5 independent measurements and the standard deviation was used for error bar.

Table 3.1: Composition of brain total lipid extract provided by Avanti Polar Lipids.

Head group	wt/wt%
PC	9.6
PE	16.7
PI	1.6
PS	10.6
PA	2.8
Unknown	58.8
Total	100

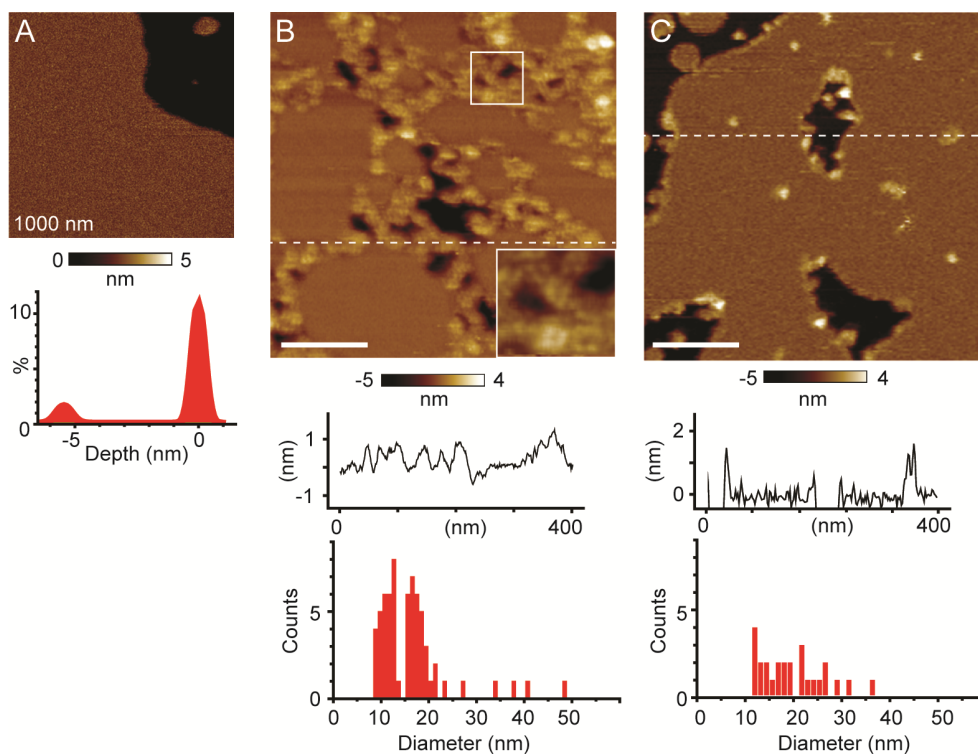


Figure 3.2: AFM images of reconstituted A β_{1-42} oligomers in BTLE or DOPS/POPE supported lipid membranes on mica. (A) AFM image of a BTLE membrane in the absence of A β . The dark region in right top corner is the mica surface. A depth histogram reveals a membrane thickness of 5.4 nm. (B) AFM image of a BTLE membrane reconstituted with A β_{1-42} oligomers (1:20 peptide/lipid mass ratio). Numerous small pore-like structures are visible at higher magnification (inset: 50 \times 50 nm² area). The cross section analysis from the dashed line shows most of the oligomers protrude < 1 nm from the membrane surface. Histograms representing the frequency of A β_{1-42} oligomers as a function of diameter shown below the cross section analysis reveal populations of oligomers mostly ranging from 9 - 20 nm. (C) AFM image of a DOPS/POPE membrane with A β_{1-42} oligomers (1:20 peptide/lipid mass ratio). Only sparsely populated small A β_{1-42} oligomers were found. The cross section analysis from the dashed line in the AFM image shows the heights of small features protrude mostly \sim 1 nm from the membrane surface with some larger A β_{1-42} oligomers. Both the cross sectional height estimates and the histograms of the diameters of A β_{1-42} oligomers were generated using a Nanoscope Analysis program. Scale bars represent 100 nm.

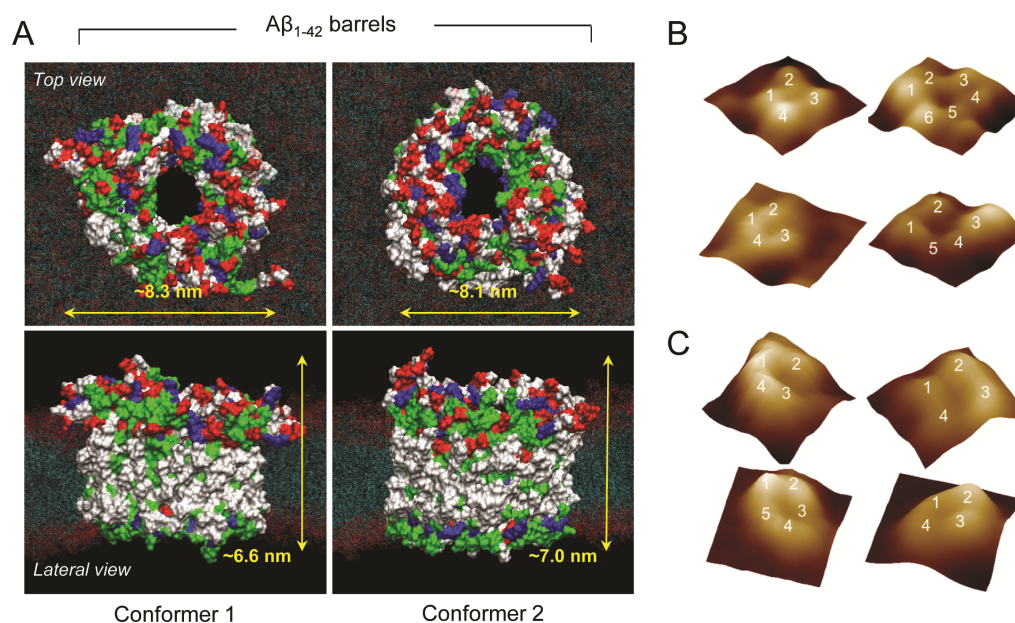


Figure 3.3: Top and lateral views of simulated (A) $A\beta_{1-42}$ channel structures embedded in the DOPS/POPE lipid bilayer for the conformer 1 and 2 18-mer barrels. The N-terminus side is represented in the upper leaflet and the turn region is represented in the lower leaflet. In the surface representation of the barrel, hydrophobic residues are shown in white, polar and Gly residues are shown in green, positively charged residues are shown in blue, and negatively charged residues are shown in red. For DOPS/POPE lipids, red dots denote the head groups, and cyan dots represent the lipid tails. Representative 3D AFM images of pore structures of $A\beta_{1-42}$ in BTLE (B) and in DOPS/POPE (C) membranes.

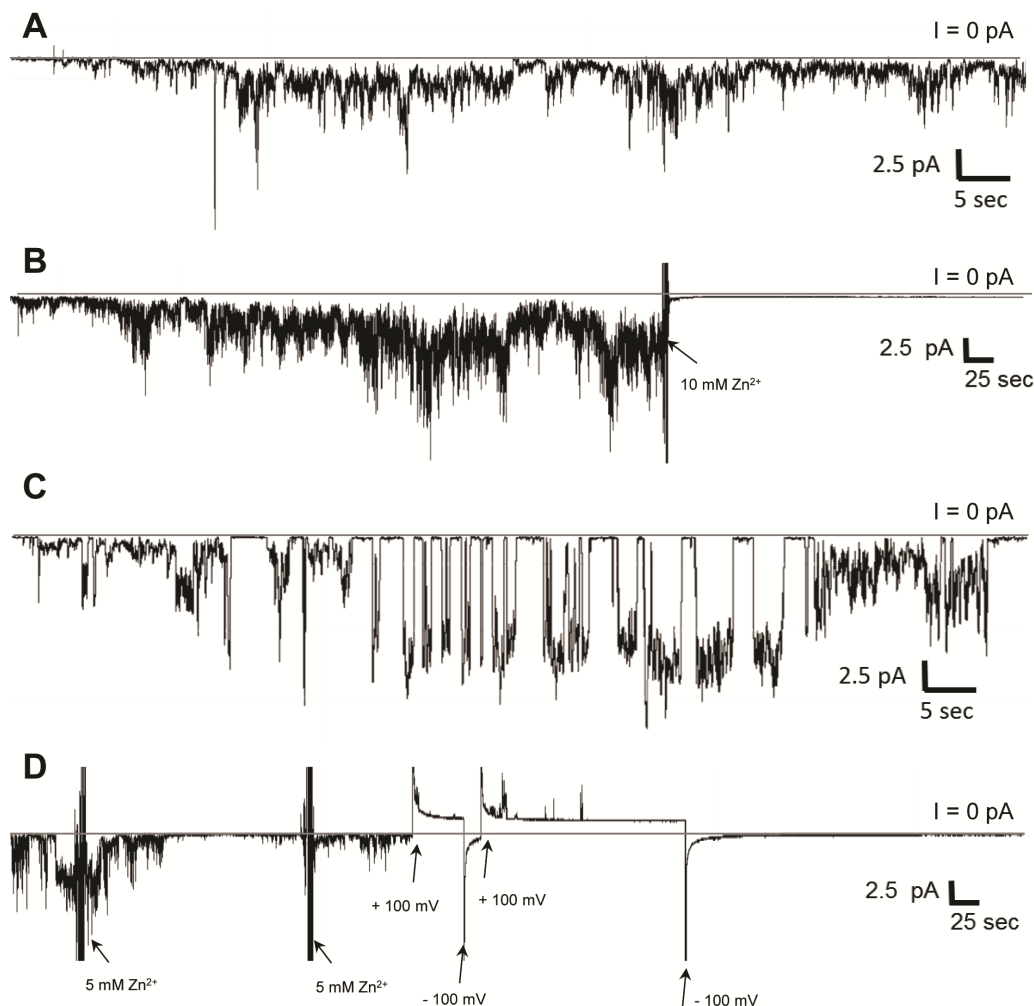


Figure 3.4: Representative electrical recordings of $A\beta_{1-42}$ in BTLE and DOPS/POPE (1:1, wt/wt) membranes. Current vs. time trace of (A) $A\beta_{1-42}$ in a BTLE membrane and (B) inhibition of $A\beta_{1-42}$ conductance by addition of Zn^{2+} (10 mM final $ZnCl_2$ concentration, *cis* chamber). Current vs. time trace of (C) $A\beta_{1-42}$ in a DOPS/POPE membrane (D) Inhibition of $A\beta_{1-42}$ conductance by addition of Zn^{2+} in DOPS/POPE membrane (10 mM final $ZnCl_2$ concentration, *cis* chamber). In all experiments, we used a final concentration of 10 μ M $A\beta_{1-42}$ in both chambers of the bilayer setup. Bilayers were formed by the painting method [133] and a bias potential of ± 100 mV was applied. Membrane capacitance was monitored to verify membrane stability. The recording electrolyte consisted of 150 mM KCl, 1 mM $MgCl_2$, 10 mM HEPES (pH 7.0) buffer was used.

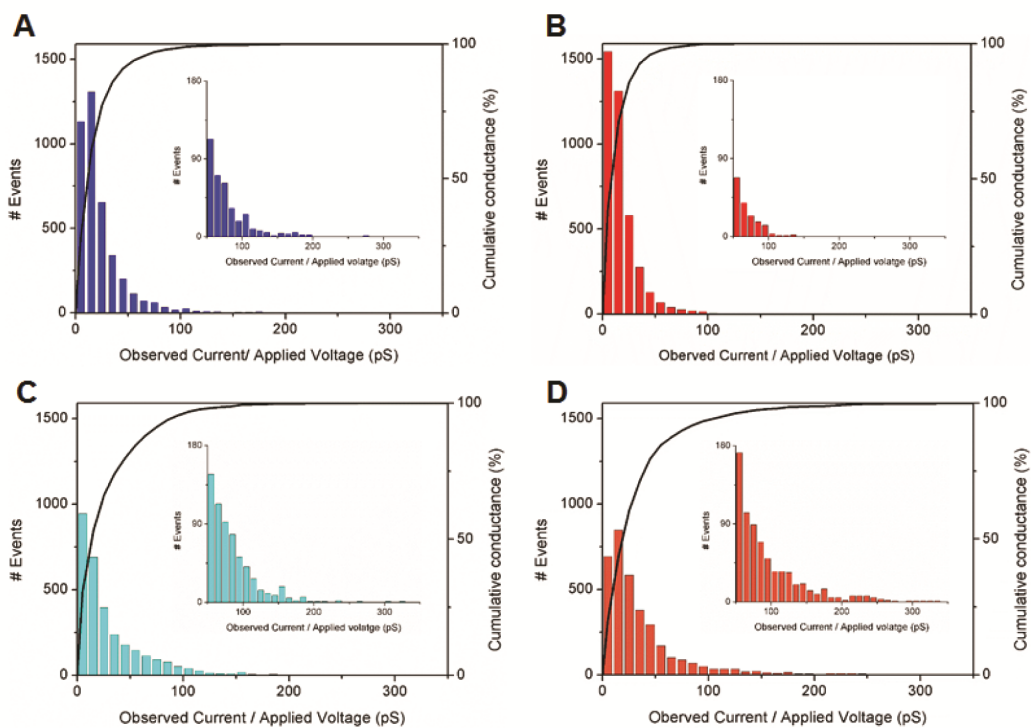


Figure 3.5: Histograms of frequency vs. conductance of ion current fluctuations of $A\beta_{1-42}$ in (A) BTLE membranes or (B) DOPS/POPE membranes and p3 in (C) BTLE membranes or (D) DOPS/POPE membranes. Insets are expanded representation of the histograms from 50 pS to 350 pS (observed current/applied voltage).

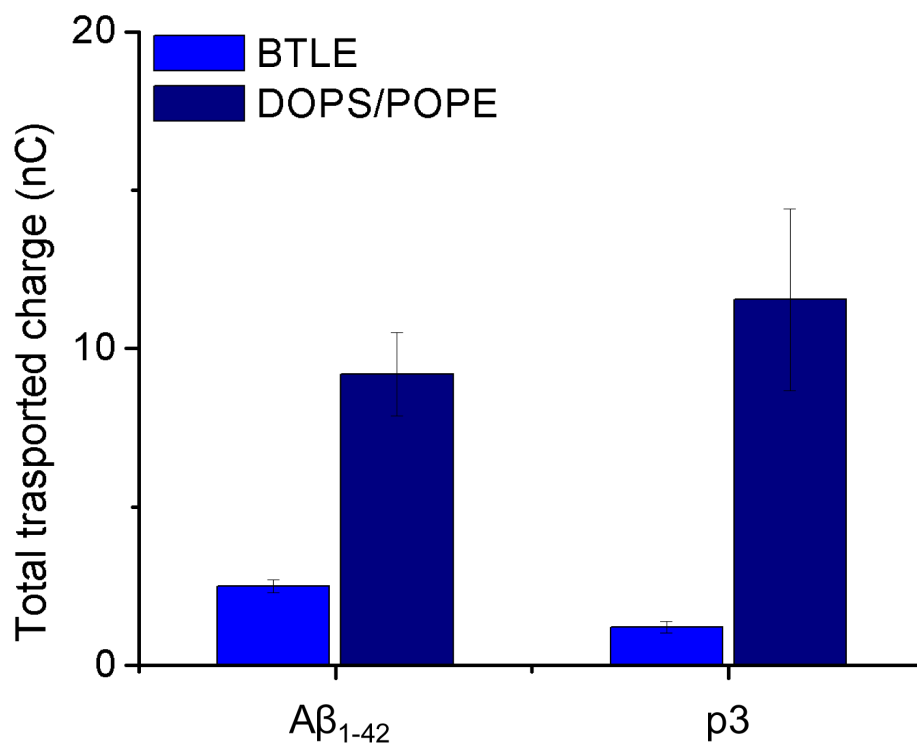


Figure 3.6: Quantification of ion influx through A β_{1-42} and p3 using the total transported charge, Q (C), in BTLE and DOPS/POPE membranes (n = 5) over a 5 minute period of time. Current vs. time traces of 11 μ M A β_{1-42} and 11 μ M p3 pore activities were integrated to quantify Q through A β_{1-42} and p3 pores (5 min. time window, +100 mV). The total transported charge of A β_{1-42} and p3 peptides in BTLE and DOPS/POPE membranes is significantly different (p = 0.028) from two way ANOVA test. The data reveal that \sim 2-fold increase in Q for A β_{1-42} in DOPS/POPE membranes compared to the Q in BTLE membranes and \sim 10-fold increase was observed in Q for p3 in DOPS/POPE membranes compared to the Q in BTLE membranes. The electrolyte solution consisted of 150 mM KCl, 1 mM MgCl₂, 10 mM HEPES at pH 7.0. The data represent mean \pm standard errors of the mean.

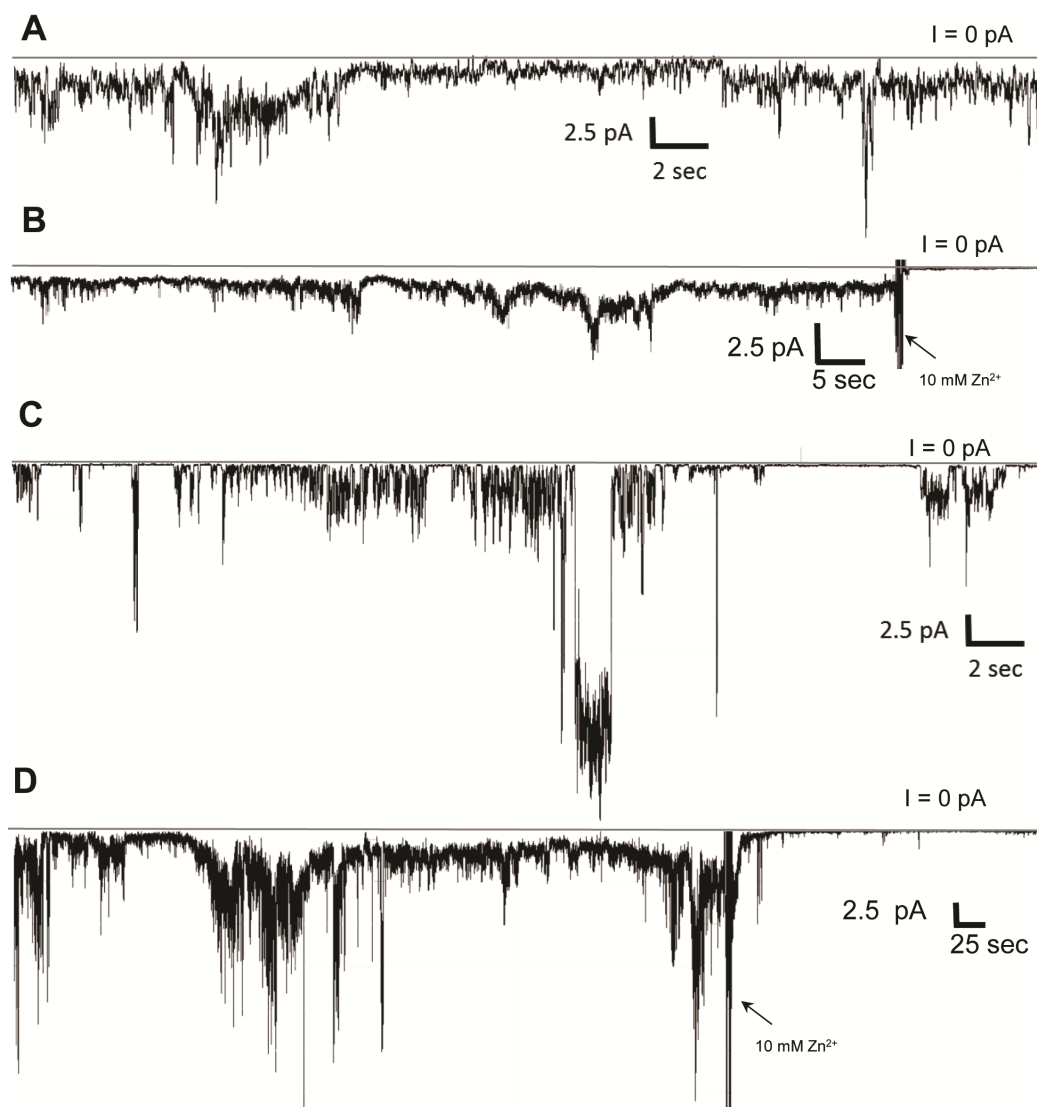


Figure 3.7: Representative electrical recordings of p3 in BTLE and DOPS/POPE (1:1, wt/wt) membrane. Current vs. time trace of (A) p3 in a BTLE membrane and (B) Inhibition of p3 ion conducting activities by addition of Zn^{2+} in BTLE lipid membrane (10 mM final concentration, *cis* chamber). Current vs. time trace of (C) p3 in DOPS/POPE membrane (D) Inhibition of p3 activities by addition of Zn^{2+} in DOPS/POPE membrane (10 mM final concentration, *cis* chamber). Bilayers were formed by the painting method and a bias potential of ± 100 mV was applied. Membrane capacitances were measured to check the stability of the membrane. 150 mM KCl, 1 mM MgCl_2 , 10 mM HEPES (pH 7.0) buffer was used.

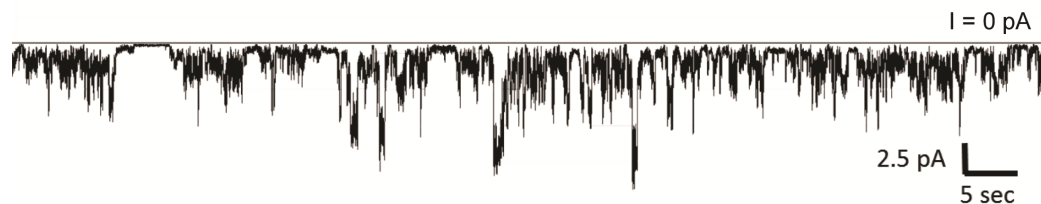


Figure 3.8: Representative current vs. time traces of $A\beta_{1-42}$ in a DOPS/DOPE (1:1, wt/wt) membrane. $A\beta_{1-42}$ oligomers show step-like conducting activities along with burst like activities. Final concentration of $11 \mu\text{M}$ $A\beta$ oligomers was added to the *cis* side of the chamber. Bilayers were formed by the painted technique and ± 100 mV bias potential was applied. 150 mM KCl, 1 mM MgCl_2 , 10 mM HEPES (pH 7.0) buffer was used.

Chapter 4

The diphenylpyrazol compound anle138b blocks $A\beta$ channels and rescues disease phenotypes in a mouse model for amyloid pathology

4.1 Abstract

Alzheimer's disease is a devastating illness eventually leading to dementia. An effective treatment does not yet exist. Here we show that oral application of the novel compound anle138b restores hippocampal synaptic and transcriptional plasticity as well as spatial memory in a mouse model for Alzheimer's disease, when given orally before or after the onset of pathology. At the mechanistic level we provide evidence that anle138b blocks the formation of conducting $A\beta$ pores without changing the membrane embedded $A\beta$ -oligomer structure. In conclusion, our data suggest that anle138b is a novel and promising

compound to treat AD-related pathology that should be tested in clinical trials.

4.2 Introduction

Alzheimer's disease (AD) is the most common neurodegenerative disorder causing a severe emotional and economic burden to our societies. Due to increased life expectancies the number of those afflicted with AD is expected to double by 2025. Despite intensive research effective therapeutic approaches are still not available. The pathogenesis of AD has been linked to protein aggregation, namely the aggregation of amyloid-beta peptides (A β) and tau protein. The accumulation of pathogenic aggregates of A β peptides in the brain appears to be a key event in the pathogenesis of AD [6, 7, 134, 135, 136] and targeting amyloid pathology still represent a promising therapeutic strategy.[137, 138] The precise molecular events that trigger amyloid-induced decline of synaptic plasticity and neuronal cell death are still not entirely resolved and are likely to be multifactorial. One of the first explanations of neuronal dysfunction and toxicity in AD is the channel hypothesis first proposed by Arispe and co-workers [89], which postulates that unregulated A β ion channels result in a loss of ionic homeostasis (primarily through a gain of Ca²⁺) that eventually triggers neuronal dysfunction and cell death. In-vivo evidence for this mechanism is however still rare and a compound that would block pores and be active in mammalian animal models has not been reported yet. Thus the original request by Arispe and coworkers that a useful strategy for drug discovery for treatment of AD should include screening compounds for their ability to block or otherwise modify A β channels is still left unsatisfied.[89] In this work, we examine the efficacy of the diphenylpyrazol (DPP) compound anle138b in an animal model of A β deposition. Oral application of anle138b ameliorates A β -induced deficits in synaptic plasticity and memory formation. This effect is linked to the capacity

of anle138b to reduce the conductivity of A β pores in lipid bilayer membranes. Our data suggests the functional modulation of the membrane bound A β -oligomers as a mechanism for neuroprotection and supports the idea that anle138b should be taken into clinical trials to treat aggregopathies, including AD.

4.3 Results

4.3.1 Synaptic plasticity and memory function in a mouse model for deposition of amyloid β after oral treatment with anle138b

We employed APPPS1 Δ 9 mice [139], a well-established model for AD-linked amyloid deposition, to test the therapeutic effect of anle138b treatment in vivo. Since in the patients therapeutic intervention is normally initiated only after the onset of amyloid plaque formation, we decided to test anle138b in two experimental cohorts. In the pre-plaque group treatment was initiated before the onset of pathology when mice were 2 months of age, while in the post-plaque group treatment was initiated after the onset of amyloid deposition and memory disturbances in 6 month-old mice.[140, 141, 142] In both cohorts anle138b was continuously provided via food pellets. Thus, in the pre-plaque group mice were subjected to anle138b or placebo treatment from 2 months of age and electrophysiological, behavioral and biochemical analysis was initiated at 6 months of age. A group of wild type (WT) mice treated with anle138b served as an additional control. We first measured synaptic plasticity by analyzing hippocampal long-term potentiation (LTP). While robust hippocampal LTP at the Schaffer-Collateral synapse was observed in WT control mice treated with anle138b (Figure 4.1A), LTP was significantly impaired in APPPS1 Δ 9 mice that received placebo (Figure 4.1B). Notably, this LTP deficit was completely rescued in APPPS1 Δ 9 mice treated

with anle138b (Figure 4.1C). This data suggest that oral application of anle138b protects against A β induced impairment of hippocampal synaptic plasticity. To test if the effect of anle138b on hippocampal plasticity also improved hippocampus-dependent memory function, another group of anle138b and placebo treated mice were subjected to the Morris-water maze test, a well-established paradigm to assay spatial memory in rodents.[143] Anle138b treated WT mice displayed robust spatial learning as indicated by decreasing escape latency throughout the 8 days of training (Figure 4.1D). In contrast, APPPS1 Δ 9 mice treated with placebo showed significantly impaired escape latency (Figure 4.1D). This deficit was partially rescued in APPPS1 Δ 9 mice that received anle138b. Spatial reference memory was analyzed in a probe test performed after 8 days of training. While WT mice showed a significant preference for the target quadrant, no such effect was observed in placebo treated APPPS1 Δ 9 mice (Figure 4.1E), confirming memory impairment in APPPS1 Δ 9 mice. In contrast, anle138b treated APPPS1 Δ 9 mice displayed a significant preference for the target quadrant indicating restored spatial memory (Figure 4.1E). Swim speed was similar amongst the groups (Figure 4.1F). We also examined if anle138b would affect basal explorative behavior (Figure 4.1G) or basal anxiety (Figure 4.1H). No difference was found amongst the groups suggesting that oral administration of anle138b can protect APPPS1 Δ 9 mice from deteriorating hippocampal synaptic plasticity and hippocampus-dependent memory consolidation.

Encouraged by this data we investigated whether anle138b could also reinstate synaptic plasticity and memory function when significant amyloid deposition had already occurred by employing the post plaque group. To this end 6-month old APPPS1 Δ 9 mice were treated with either anle138b or placebo for 4 months. WT mice treated with anle138b served as an additional control group. Analysis was performed when mice were 10 month

of age. In a first cohort we measured hippocampal LTP. WT mice treated with anle138b showed robust LTP (Figure 4.2A), while LTP was significantly impaired in placebo treated APPPS1 Δ 9 mice (Figure 4.2B). Notably, a complete restoration of hippocampal LTP was seen in APPPS1 Δ 9 mice treated with anle138b (Figure 4.2C). In conclusion, similar to the pre-plaque group treatment with anle138b had a marked ameliorating effect on LTP even after the onset of plaque deposition.

To analyze if reinstatement of hippocampal plasticity would also correlate with improved memory function, we subjected mice to the Morris water maze test. WT mice treated with anle138b rapidly learned the task as indicated by reduced escape latency throughout the 8 days of training (Figure 4.2D). Placebo treated 10-month old APPPS1 Δ 9 mice display impaired spatial learning as indicated by the escape latency that did not significantly decrease during the training (Figure 4.2D). When compared to the placebo group, APPPS1 Δ 9 mice treated with anle138b showed improved spatial learning (Figure 4.2D). A probe test was performed after 8 days of training. WT mice treated with anle138b showed a significant preference for the target quadrant indicative of intact spatial reference memory (Figure 4.2E). Placebo treated APPPS1 Δ 9 mice exhibited severely impaired memory function (Figure 4.2E) and displayed no target preference (Figure 4.2E). In APPPS1 Δ 9 mice treated with anle138b (Figure 4.2E) target preference was improved significantly but did not reach WT levels. Of note, swim speed was not different between the experimental groups (Figure 4.2F). Exploratory behavior (Figure 4.2G) and basal anxiety (Figure 4.2H) were measured in the open field test. There was no significant difference amongst groups. Thus, oral administration of anle138b partially restores hippocampal plasticity and memory function in APPPS1 Δ 9 mice even at an advanced stage of pathology.

4.3.2 Anle138b reinstate transcriptional homeostasis and ameliorates amyloid pathology

Pathological alterations often lead to aberrant changes in transcriptional plasticity indicating subde-regulated cellular homeostasis.[144] To this end numerous studies have shown that AD pathogenesis is linked to altered gene-expression in various brain regions.[144, 145, 146]. Moreover, there is evidence that monitoring gene-expression changes can inform about the efficacy of therapeutic intervention.[146]

To this end we performed RNA-sequencing from hippocampal tissue in the pre- and post-plaque experimental groups. We first compared hippocampal gene-expression in WT mice treated with placebo or anle138b. Neither in the pre- or the post-plaque group did we find any differentially expressed genes (Figure 4.1A) indicating that treatment with anle138b does not affect gene-expression and cellular homeostasis in the absence of pathological changes. Next we compared gene-expression in placebo treated WT and APP mice of the pre-plaque group. We identified 202 differentially expressed genes of which 73 were up- and 129 were down-regulated (Figure 4.3B). Pathway analysis shows that de-regulated genes are linked to reduced energy metabolism, mitochondria function, cytoskeleton integrity and synaptic plasticity, while pathways linked to cell growth were increased (Figure 4.3C). This data is in line with previous reports of gene-expression changes in AD.[145, 146]

Of note, in APP mice treated with anle138b only 27 genes were de-regulated when comparing APP to control mice (Figure 4.3B). Thus none of the pathways deregulated in response to amyloid pathology (Figure 4.3C) remained significant after anle138b treatment and in fact no enrichment for any specific pathway could be detected. Since the expression of the APP and PS1 transgenes was similar in placebo and anle138b treated APP mice (Figure 4.3D) the gene-expression data supports the electrophysiological and behavioural findings

and indicates that in the pre-plaque group anle138b treatment reinstates cellular homeostasis in the hippocampus of APPPS1 Δ 9 mice. We also analyzed hippocampal gene-expression in the post-plaque group. When comparing placebo treated WT and APP mice we found 130 differentially expressed genes of which the majority (124) were up-regulated (Figure 4.3B). The comparison of anle138b treated WT and APP mice revealed 220 differential expressed genes (Figure 4.3B). Many of the genes de-regulated in the placebo and anle138b treated groups were similar (Figure 4.3E) and pathway analysis revealed that in both groups gene-expression changes almost exclusively represent an induction of neuroinflammatory processes (Figure 4.3F). This data suggests that anle138b treatment does not have a major impact on inflammatory processes when given at a stage of advanced amyloid pathology. Since anle138b treatment nevertheless reinstated hippocampal synaptic plasticity and also partially restored memory function, these findings indicates that the therapeutic efficacy of anle138b is most likely not due to the dampening of inflammatory processes.

Since anle138b was shown to exhibit anti-aggregative effects in models for α -synuclein and prion toxicity [147] it is likely that at least part of the therapeutic effect observed in this study is due to anle138b interfering with amyloid aggregation. To test this hypothesis we prepared brain slices for immunohistochemical analysis using thioflavin S staining which is commonly used to quantify A β plaques (Figure 4.4A). We first assayed the amyloid plaques pathology in the hippocampus and cortex in the pre-plaques group. Since no amyloid pathology was detectable in WT mice treated with anle138b this data served as technical control. We observed a significant reduction in the number of plaques and the total area covered by plaques of anle138b-treated animals (Figure 4.4A). Similar results were obtained when we analyzed plaque load in the post-plaques group (Figure 4.4B), although the pathology was generally more severe in the post-plaque group. Thus,

oral administration of anle138b reduces amyloid pathology when administered before or after the onset of pathology.

4.3.3 Biophysical characterization of $A\beta$ in the presence of anle138b

To better understand the mechanisms that underlie the therapeutic effect of anle138b we analyzed its impact on the pore formation of $A\beta$. [89] To this end we employed black lipid membranes (BLM) using a mixture of POPE and DOPS in a 1:1 ratio (Figure 4.5), an assay in which the current passing through the membrane is a measure of membrane integrity. We first established that the conductance and the morphology of POPE and DOPS lipids, as measured by atomic force microscopy (AFM), lipid bilayers are not affected in the presence of anle138b.

When we examined the effect of $A\beta_{1-42}$ in DOPS/POPE (1:1) membranes, a step-wise growth of bulk membrane conductance indicates that the activity increases through the combined action of many individual pores (Figure 4.5A). This stacking effect is likely the result of prolonged pore lifetimes and the formation of opening and/or additional conducting pores. The significantly reduced pore activity observed in anle138b-doped membranes (Figure 4.5B) suggests activity of fewer $A\beta_{1-42}$ pores compared to the number of active pores in the membranes without the anle138b compound. Instead, the pore dynamics appear to be affected, resulting in less stable and shorter lived open pores, and a reduction in the total number of conducting pores. AFM data revealed that anle138b treatment did not affect the structure of $A\beta_{1-42}$ pores in this assay (Figure 4.6) suggesting that anle138b does not simply prevent $A\beta_{1-42}$ from entering lipid bilayer membranes and forming pores. Rather anle138b appears to render conducting $A\beta_{1-42}$ pores to non-conducting ones thereby providing one possible mechanism by which anle138b ameliorates LTP and learning defects

in APP.

To provide further *in vivo* evidence for this interpretation we treated primary hippocampal neurons with A β ₁₋₄₂ monomers or oligomers in the absence or presence of anle138b and assayed membrane integrity. While the addition of A β ₁₋₄₂ oligomers but not A β ₁₋₄₂ monomers significantly impaired membrane integrity, this effect was rescued by anle138b (Figure 4.5C). This effect is not simply due to anle138b-mediated reduced cell death, since the viability of hippocampal neurons measured via the MTT assay was identically affected by A β ₁₋₄₂ monomer and oligomer treatment in our experimental setting (Figure 4.5D).

4.3.4 Discussion

In this work, we investigated the effect of anle138b in the established APPPS1 Δ 9 mouse model for AD. Anle138b was previously found to be orally available when applied via dry food and to reach levels of up to 100 μ M in the brain.[148] There is no evidence that anle138b is metabolized in the brain and the metabolites detected in other organs were not found in the brain either, compatible with their dramatically increased hydrophilicity.[147] Anle138b was also found to be non-toxic in mice up to 2 g/kg. Mice that received similar concentrations of anle138b as used in our study lived without any detectable toxicity, even when the drug was applied for more than a year.[147] Also in this study, no negative or positive effects of anle138b on WT animals were detected. The APPPS1 Δ 9 mouse model features dysfunction of neurons detected by memory decline after four months and severe plaques formation after 6 months.[149] Of note, anle138b treatment completely restored hippocampal LTP in the pre- and post-plaque group of APPPS1 Δ 9 mice. In line with this observation spatial reference memory was fully or partially restored in the pre- and

post-plaque groups, respectively. There have been numerous pre-clinical studies aiming to restore synaptic plasticity and memory function in mouse models for amyloid pathology, ranging from antibody based therapies [150], symptomatic treatments not directly targeted towards amyloid [151], small molecules that modulated APP processing [152] or small molecules that are supposed to target toxic amyloid species directly. [153] Anle138b belongs to the latter category and its therapeutic effect is in line with other small molecule drugs. For example, epigallocatechin gallate (EGCG) that was shown to affect A β toxicity by redirecting toxic A β structures into off-pathway oligomers [154, 155] and was able to ameliorate spatial memory deficits in APP mice after the onset of amyloid deposition. [156] In addition to the restoration of hippocampal LTP and spatial reference memory, we also observed restoration of physiological gene-expression in the pre-plaque group, indicating that hippocampal maintain a homeostatic state. As such in placebo-treated mice genes linked to metabolic function and neuronal plasticity were down-regulated, while this effect was completely reverted after anle138b treatment. Even in the placebo treated pre-plaque group we observed little evidence for neuroinflammatory processes, which is in contrast to the data from the post-plaque group. In fact, the gene-expression changes observed in the placebo-treated post-plaque group were dominated by increased inflammation. This data suggest that in APPPS1 Δ 9 mice the decline of synaptic plasticity precedes inflammatory processes. Of note, anle138b treatment had no effect on pathological gene-expression in the post-plaque group, yet hippocampal LTP was completely restored and spatial memory was partially restored. This data suggests that therapeutic strategies that aim to reduce amyloid toxicity at least in the APPPS1 Δ 9 model may have little influence on neuroinflammation when applied at an advanced stage of the disease. Nevertheless, a significant therapeutic effect could be observed in the post-plaque group. This might be explained by removal of

toxic A β species which can lead to the restoration of synaptic function in neurons even in a detrimental inflammatory environment. The question by which mechanism toxic A β species induces synaptic dysfunction and neurotoxicity is still under debate and include for example NMDA receptor endocytosis [157], α -amino-3-hydroxy-5-methyl-4-isoxazole propionic acid surface receptor modulation [158] as well as pore formation via A β channels.[89] Especially the latter hypothesis has long been proposed but has not been studied intensively so far. Since synaptic function relies on the integrity of membranes and their ability to modulate ion fluxes in a voltage dependent way, we focused on the questions whether anle138b would modulate the pore forming activity of A β , an idea that has been proposed to be a mechanism for impaired neuronal function and cell death already more than 20 years ago.[89] This mechanism was also proposed in cell based models for EGCG [159] as well as the related compounds MRS2481 and MRS2485. [159] The observed stepwise growth of bulk membrane conductance in the presence of A β without anle138b, indicates that the activity increases through the combined action of many individual pores.

Numerous MD simulations [51, 79, 19] and NMR spectroscopy based investigations [160] of A β pores have pointed to a β -barrel structure for the intramembrane region of the pore. It was previously shown that A β containing a point substituted proline (F19P) showed pore structure by AFM but did not demonstrate ionic conductance.[128, 90] The chemical structure of proline introduces a kink in the peptides secondary structure, which is known to disrupt β -sheet formation. MD simulations of F19P barrel structure showed that β -sheet destabilization led the highly charged N-terminal regions to bind at the peptide mouth and collapsed the pore.[90, 91] Our data is consistent with such a model and suggests that anle138b induces a conformational change within A β pores that greatly reduces or, in most pores eliminates, toxic ionic flux. Steric blockage by anle138b without conformational

change of the pore is energetically unfavorable due to the hydrophobicity of anle138b, as this scenario would require anle138b to be in contact with water molecules inside the pore. The above mentioned mechanisms provide further insight into the method of action in preventing pore activity and reducing Alzheimer's pathogenicity. In vivo evidence to further support the notion that anle138b counteracts the detrimental effect of toxic A β species on membrane integrity stems from our finding that A β 1-42 administration to hippocampal neurons impaired membrane integrity, which was attenuated by anle138b. Our interpretation that conversion of conducting to non-conducting A β pores is one possible mode of anle138b action, may also explain that anle138b ameliorated all tested disease phenotypes in the pre-plaque group, while in the post-plaque group only LTP was completely restored. Hence in the post-plaque group the presence of toxic A β species has already induced secondary processes such as inflammation that persistently affect memory function even if membrane integrity and LTO is restored in neurons.

4.3.5 Conclusion

Our data shows that anle138b can reinstate synaptic plasticity and memory function in a mouse model for amyloid pathology via mechanisms that involve the blockage of A β induced pores in membranes. Careful analysis of this activity indicates that the oligomers are still in the membrane but have a changed conductivity profile, mainly staying open for shorter time and lacking the possibility of building up large currents as seen in the absence of the compounds. Taking into account that anle138b has beneficial effects in animal models for Parkinsons and Prion diseases REF and also shows to ameliorate disease phenotypes in a mouse model for Tau pathology, we suggest that anle138b should be tested in humans for its potential to treat aggregopathies.

4.4 Materials and Methods

4.4.1 Mouse Experiments

The APP(Swe)/PS1E Δ 9 (henceforth called: APPPS1 Δ 9) mouse model of AD was used for this study. Upon completion of treatment, these and control mice underwent cognitive assessment by a behavior battery of tests. Electrophysiology, small RNA-sequencing and histochemical analysis of plaque burden were also assessed. All mice were maintained on a C57BL/6 background. They were kept in a 12 h dark/light cycle and housed in groups under constant standard conditions of temperature and humidity. Mice had at libitum access to food and water. Animal care and handling were carried out in compliance with the Declaration of Helsinki and approved by local ethical committees.

Anle138b treatment. In order to investigate the prophylactic effect of anle138b, we treated healthy, plaque-free, adult, APPPS1 Δ 9 mice with placebo- or anle138b-containing dry food pellets for 4 months (from 2 to 6 months of age) (Pre-plaque group). Age- and sex-matched wild-type littermates were also treated and served as controls. Similarly, in order to investigate the therapeutic effect of anle138b, we treated symptomatic APPPS1 Δ 9 mice and treated them for 4 months (from 6 to 10 months of age) (Post-plaque group). Controls were age- and sex-matched wild-type littermates treated with anle138b or placebo. Anle138b was administered orally. Dry food pellets were prepared containing 2 g anle138b per kg food (SSNIFF). This amounted to an estimated daily dose of 500 mg/kg (at an approx. 6 g daily food consumption and 25 g body weight). Based on pharmacokinetics studies, 40 to 70 μ M anle138b reached the brain during most of the wake phase.[148] Placebo food was prepared from the same batch but without anle138b (SSNIFF). Of note, our previous PK studies in mice have shown that after a single bolus the half-life of anle138b in the brain is

approximately 4 h.[147]

Morris Water Maze. Mice were single-caged and brought into the testing room at least one week prior to the beginning of the experiment to allow them to acclimate. In the Morris Water Maze, mice were trained to find a submerged 10x10 cm platform in a pool (1.10 m in diameter) of milky water using spatial cues by the pool sides as orientation points. Mice were trained over 8 consecutive days with 4 trials per day per mouse. Time and path to platform were tracked and recorded (TSE systems). On day 9 (probe test), the platform was removed and quadrant preference was recorded (target quadrant being that one where the platform was). Open Field. Mice were allowed to spend 5 min in an open arena (40x40 cm). Path length while exploring as well as time in the center or corners were quantified using the VideoMot2 System (TSE).

RNA-sequencing. Library preparation and cluster generation for mRNA sequencing was performed according to Illumina standard protocols (TruSeq, Illumina). Libraries were quality-controlled and quantified using a Nanodrop 2000 (Thermo Scientific), Agilent 2100 Bioanalyzer (Agilent Technologies) and Qubit (Life Technologies). Base calling from raw images and file conversion to fastq-files was achieved by Illumina pipeline scripts. Subsequent steps included quality control (FastQC, www.bioinformatics.babraham.ac.uk), mapping to reference genome (mm10, STAR aligner v2.3.0,[161] non-default parameters), read counting on genes or exons (HTSeq, <http://www-huber.embl.de/users/anders/HTSeq>, mode: intersection-non-empty) and differential gene (DESeq2 1.4.5 [162]) usage biostatistical analysis. PCA and distance heatmaps were generated in R following instructions in the vignette for DESeq2. Genes were considered differentially expressed with an adjusted (Benjamini-Hochberg) as indicated in the figure legends. Gene set overlaps were calculated using Venny (<http://bioinfogp.cnb.csic.es/tools/venny/>). Pathway analysis was performed

using Cytoscape (www.cytoscape.com)

4.4.2 Electrophysiology on hippocampal slices

Slice Preparation. Acute hippocampal slices prepared from WT mice and from APPPS1 Δ 9 mice were used for electrophysiological recordings. All the procedures were carried out in compliance with the guidelines from the Animal Committee on Ethics in the Care and Use of Laboratory Animals of TU-Braunschweig. Briefly, after anesthetization using CO₂, the mice were decapitated and the brains were quickly removed and cooled in 2-4 °C artificial cerebrospinal fluids (ACSF). The hippocampi were dissected and transverse hippocampal slices (400 μ m) were prepared by using a manual tissue chopper. Then the slices were incubated for 3 h at 32 °C in an interface chamber (Scientific System Design) which was continuously perfused with oxygenated aCSF at a flow rate of 0.8 ml/min. The ACSF contained the following (in mM): 124 NaCl, 4.9 KCl, 1.2 KH₂PO₄, 2.0 MgSO₄, 2.0 CaCl₂, 24.6 NaHCO₃, 10 D-glucose, equilibrated with 95% O₂/5% CO₂ (32 L/h).

Slice Recordings. To evoke field EPSP (fEPSP) from Schaffer collateral/commissural-CA1 synapses, one monopolar lacquer-coated, stainless-steel electrode (5 M Ω ; AM Systems) was positioned at the stratum radiatum layer of the CA1 region. For recording fEPSP (measured as its initial slope function), one electrode (5 M Ω ; AM Systems) was placed in the CA1 apical dendritic layer and signals were amplified by a differential amplifier (Model 1700, AM Systems). The signals were digitized using a CED 1401 analog-to-digital converter (Cambridge Electronic Design). After the preincubation period, an input-output curve (afferent stimulation vs. fEPSP slope) was generated. Test stimulation intensity was adjusted to elicit fEPSP slope of \sim 40% of the maximal fEPSP response. Four 0.2 Hz biphasic constant current pulses (0.1 ms/polarity) were used for baseline recording and testing at each

time point. Long-term potentiation (LTP) was elicited by strong tetanus (STET) consisting of three stimulus trains of 100 pulses at 100 Hz delivered at 10 min intervals (300 pulses in total). Data (fEPSP slope) was normalized to baseline and plotted as average \pm SEM. The average values of the slope function of the fEPSP (millivolts per milliseconds) for each time point were analyzed using paired t test; $P < 0.05$ was considered as statistically significant.

Thioflavin S Staining. Thioflavin S staining was performed as previously described with the some modifications.[163, 164] Briefly, mice were sacrificed and their brain quickly removed on ice. Left hemispheres were embedded in OCT (Tissue TEK) and stored at -80°C until ready to section. Sagittal, $25\ \mu\text{m}$ -thick sections were cut using a cryostat. And, 5 sets of 5 slides per brain containing 4 sections/slide were made by taking every 5th section, so that each set consisted of 20 representative sections throughout the brain. Sections were then fixed with 4% PFA for 25 min at room temperature, washed twice with 0.9% NaCl and quickly rinsed with PBS. Staining was performed using 0.05% thioflavin S in 50% ethanol for 8 min in the dark and differentiated with two changes of 80% ethanol for 10 sec. This was followed by 3 washes with large volumes of distilled water and an incubation step in high-concentrated phosphate buffer (411 mM NaCl, 8.1 mM KCl, 30 mM Na_2HPO_4 , 5.2 mM KH_2PO_4 , pH 7.2) at 4°C for 30 min. Finally, slides were briefly rinsed in PBST and covered with coverslip using Vectashield Hard Set mounting media with DAPI (Vector). Slides were allowed to set in the dark at 4°C and imaged immediately thereafter. To control for background, unspecific staining or tissue auto-fluorescence, slides from age-matched wild-type brains were used as negative control. Images at 4X magnification of hippocampus and cortex were captured using an Olympus IX70 fluorescence microscope. Quantification of number of plaques, area covered by the plaque and average plaque size was performed using the particle analysis tool of the ImageJ software. Statistical analysis was carried out

using GraphPad Prism5.

4.4.3 Biophysical characterization on A β ₁₋₄₂

Materials A β ₁₋₄₂ was purchased from Bachem and Anaspec (Fremont, CA). The phospholipids 1,2-dioleoyl-*sn*-glycero-3-phosphoserine (DOPS) and 1-palmitoyl-2-oleoyl-*sn*-glycero-3-phosphoethanolamine (POPE) were purchased from Avanti Polar Lipids (Alabaster, AL). All other chemicals were purchased from Sigma-Aldrich (St. Louis, MO).

Peptide handling For BLM experiments, A β ₁₋₄₂ peptides were dissolved in Milli-Q water to a concentration of 1 mg/mL prior to being aliquoted for storage. These 50 μ L aliquots were stored at -80 °C for a maximum of 60 days before use. Samples were thawed only once. For ThT and AFM experiments, powder form of A β ₁₋₄₂ (Bachem, Torrance, CA) was first dissolved in 1% ammonium hydroxide until the peptides were completely dissolved. They were subsequently sonicated for approximately 2 min. Small volume of peptides were then aliquoted and lyophilized using a lyophilizer (Labconco FreeZone 2.5 Plus, Kansas City, KS). The aliquots were stored at -80 °C until used. For every experiment, aliquoted peptides were thawed and hydrated in 20 mM NaOH and HEPES buffer solutions at pH 7.4, sequentially. The peptide concentration was measured using the 280 nm UV absorbance ($\epsilon = 1490 \text{ M}^{-1}\text{cm}^{-1}$).

Planar Lipid Bilayer Electrical Recording We prepared planar lipid bilayers using the so-called "painted" technique.[133] Anle138b was mixed with a 1:1 (w/w) solution of DOPS and POPE in chloroform at a concentration of 10 mM with respect to the volume of the lipids. A lipid specific gravity of 0.8 was used for the calculation. This mixture was subsequently dried in a Rotavapor R-210 (Buchi) and resuspended in decane at a total lipid concentration of 20 mg/mL. Bilayers with embedded Anle138b were formed from this

solution. Spontaneous membrane formation occurs following the addition of lipid directly over a pore with a diameter of $\sim 250 \mu\text{m}$ in a Delrin septum (Warner Instruments, Delrin perfusion cup, volume 1 mL). In previous studies, this membrane composition was shown to be stable for long recording times (~ 4 hrs). Control experiments establishing the stability of membranes formed with the addition of Anle138b were performed. As the electrolyte, we use 150 mM KCl, 10 mM HEPES (pH 7.4), and 1 mM MgCl_2 .

With the preparation of the anle138b loaded lipids we observed the following difficulty: Anle138b was dissolved in decane along with the lipids prior to membrane painting. Since Anle138b is soluble in both the decane and the lipids, the distribution of compound in the lipid membrane that spontaneously forms upon lipid deposition over the aperture can vary. Lipid monolayers bind to either side of the partition and the bilayer membrane forms as the monolayers fuse together at the center, excluding the decane solvent to the perimeter. This solvent annulus acts as a bridge to the delrin partition and is essential for membrane stability.[165] If a significant proportion of the Anle138b is mobile in the decane, the compound could be partitioned to the solvent annulus rather than incorporated into the membrane leading to BLM results that appear similar to that seen with $\text{A}\beta_{1-42}$ in the absence of compound. This is why we believe that only in 50% of the cases anle138b modulated the activity of the pores.

Before performing electrical recordings, we verified that the bilayer was stable for several minutes with low conductance (< 10 pS) across 100 mV applied voltage and that the system capacitance was > 110 pF. When both criteria were met, peptide was added directly to the *cis* (hot wire) side and stirred for 5 min. Peptide concentration in the bilayer chamber was approximately $10 \mu\text{M}$. Bilayer stability was monitored by periodic capacitance measurements throughout the course of the experiment.

All traces were recorded in voltage clamp mode using the 2 kHz built-in filter cutoff of our BC-535 amplifier (Warner Instruments, Hamden, CT). A sampling frequency of 15 kHz was used for all data acquisition. We used a custom-made LabVIEW program to record the current and Clampfit 10.2 (Molecular Devices, Sunnyvale, CA) to analyze traces. For representation in figures, we have filtered the recorded current versus time traces with a digital Gaussian low-pass filter with a cutoff frequency of 50 Hz.

Lipid Bilayer Preparation for AFM Imaging For liposome preparation, 1-palmitoyl-2-oleoyl-sn-glycero-3-phosphoethanolamine (POPE) and 1,2-dioleoyl-sn-glycero-3-phospho-L-serine (DOPS) lipids were used in a 1:1 ratio (both purchased from Avanti Polar Lipids, Alabaster, Al). Liposomes were prepared by mixing 20 μL of each lipid (5 mg/mL) dissolved in chloroform and allowed to dry overnight in vacuum. The dried lipid film (and anle138b) was hydrated with peptide solution (1:60 peptide to lipid molar ratio) to facilitate peptide incorporation in the lipid bilayer, resulting in proteoliposome formation. For control, the dried lipid film (and anle138b) was hydrated with 200 μL of HEPES buffer and vortexed occasionally for an hour. The large multilamellar vesicles formed with this procedure were sonicated for 5 min. Supported lipid bilayers were formed by (proteo)liposome rupture and fusion on the mica substrate.[21, 90, 91, 17, 103, 44] Lipid concentrations of 0.1~1 mg/mL were deposited on freshly cleaved mica and incubated for ~ 10 min on a hot plate above the lipid transition temperature to facilitate fusion of the ruptured proteoliposomes on the mica surface. As a last step, samples were rinsed with buffer to remove unruptured proteoliposomes still in solution.

AFM Imaging on Membranes Topographic images were acquired using a Multimode AFM equipped with a Nanoscope V controller (Bruker, Santa Barbara, CA). Silicon Nitride cantilevers with spring constants of 0.08 N/m (OMCL-TR400, Olympus) were employed

for imaging in fluid using tapping mode. Resonance frequencies of ~ 8 kHz and drive amplitudes under 100 mV were used. All experiments were performed at room temperature. Actual spring constants were measured using thermal tune before the experiments. To measure outer pore diameters, tip broadening was taken into account by modeling the inserted oligomers as a spherical cap protruding a height, h above the surface of the lipid bilayer in contact with a spherical tip of radius, R . [115]

4.4.4 Cell Membrane Integrity and viability

CyQUANT. Primary neuronal cultures were produced from E17.5 CD1 Swiss embryos. On DIV 10 cultures were treated conditioned medium supplemented with anle138b to a final concentration of 1 μM in 0.05% DMSO (Roth, A994.2) or 0.05% DMSO as vehicle. After 24 h $\text{A}\beta_{1-40}$ oligomers, monomers or buffer ($n=4$ each) were applied at 10 μM and incubated for 48 h. CyQUANT[®] Direct Cell Proliferation Assay (Thermo Fisher, C35011) was used according to manufacturers protocol to determine membrane integrity. After 30 min incubation fluorescence was measured with a Tecan infinite 200. Statistical analysis was performed in GraphPad Prism.

MTT assay. Cell viability was measured using the MTT assay with the same sample preparation as for the CyQUANT assay. Briefly, after anle138b and $\text{A}\beta$ treatment the cell culture medium was supplemented with MTT to a final concentration of 0.5 mg/ml and incubated for 1 h at 37 °C in a standard cell culture incubator. Subsequently medium was removed and metabolites suspended in 500 μl DMSO. Absorption at 800 nm was measured using a Tecan infinite 200.

4.5 Acknowledgements

Chapter 4, in part, has been submitted for publication of the material as it may appear in Hernandez Martinez, A., Urbanke, H., Gillman, A.L., Lee, J., Ryazanov, S., Agbemenyah, H.Y., Li, Q., Rezaei-Ghaleh, N., Wilken P., Bartels, C., Leonov, A, Leonov, A., Lal, R., Benz, R., Zweckstetter, M., Giese A., Schneider A., Korete, M., Griesinger, C., Arce, FT., Eichele, G., Fischer, A. The diphenylpyrazol compound anle138b blocks A β channels and rescues disease phenotypes in a mouse model for amyloid pathology. 2017 (*under revision*). The dissertation author was the primary author of this paper.

We thank Lina-Maria Jaime Tobon and Inga Urban for assistance. This work was supported by core funds from the DZNE (to AF and MZ), the Max Planck Society (to GE and CG), the Hans and Ilse Breuer Award for Alzheimers disease (to AF), the DFG project FI981/9-1 (to AF) and the EU (ERC consolidator grant to AF) . HU holds a PhD fellowship from the Hans and Ilse Breuer Foundation. J.L., A.L.G., and R.L. acknowledge support from the National Institute on Aging of National Institutes of Health (Grant AG028709).

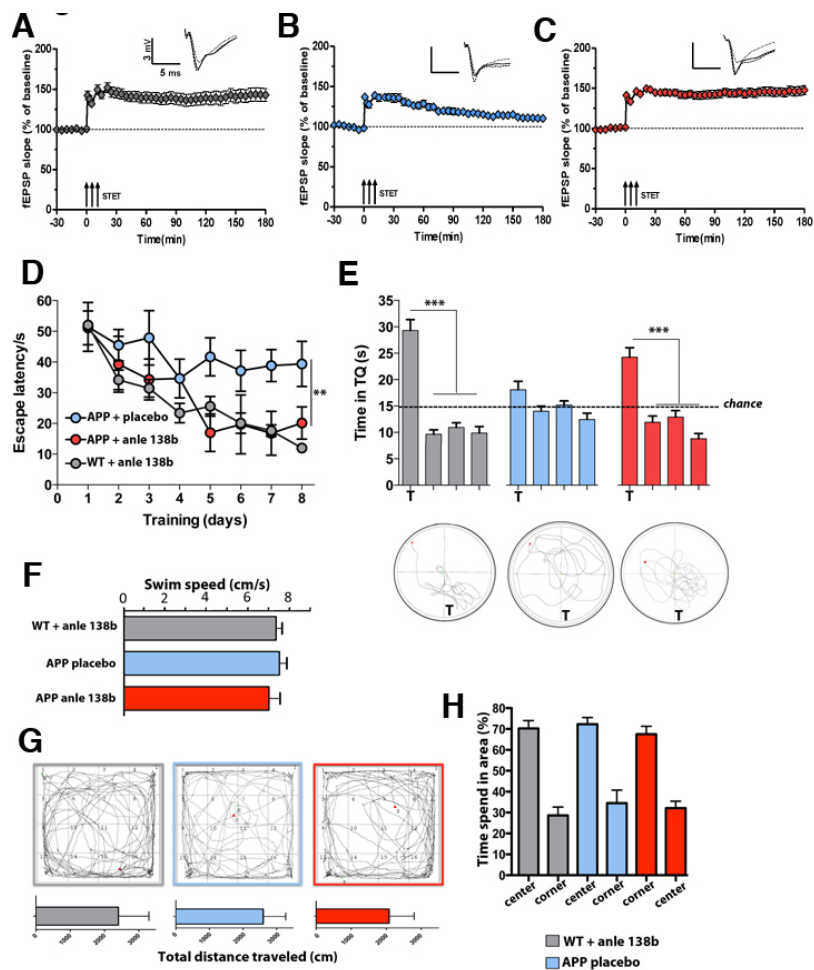


Figure 4.1: Anle138b rescues hippocampal LTP deficits spatial memory in the pre-plaque group. A. In WT mice of the pre-plaque group (treated from 2-6 month of age with anle138b) robust LTP that lasts for at least 3h is elicited upon a strong tetanization (STET) (3 trains of 100 pulses at 100 Hz given 10 min apart, arrows) at the schaffer-collateral synapse (t test, $P = 0.0001$; $n = 16$). B. LTP is not maintained in APPPS1 Δ 9 mice treated with placebo. Here, the potentiation declined to baseline after 3 h (t test, $P = 0.08$; $n = 20$). C. APPPS1 Δ 9 treated with anle138b show reversal of LTP impairment (t test, $P < 0.0001$; $n = 23$). D. Escape latency in the Morris water maze test is impaired in placebo but not in anle138b treated APP mice (ONE-way ANOVA $F = 16,01$, $**P < 0,0008$ $n = 15/\text{group}$). E. Probe test performed 24 h after the last training session. The lower panel shows representative swimming path during the probe test. T = target quadrant compared vs. other quadrants (t test, $***P < 0,0001$). F. Average swim speed during water maze training. G. Explorative behavior in the open field test. Upper panel: Representative motion tracks during the test session. Lower panels show the total distance traveled during the 5 min test session. H. Bar graph showing the time spent in the center vs. the corner of the open field. Error bars indicate SEM.

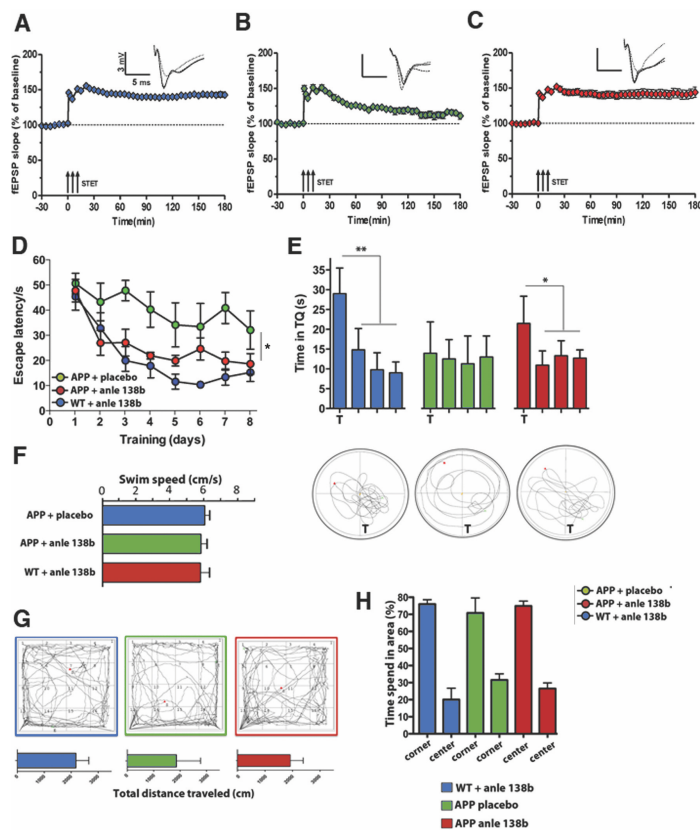


Figure 4.2: Anle138b rescues hippocampal LTP deficits spatial memory in the post-plaque group. A. WT mice of the post-plaque group (treated from 6 - 10 month of age) display robust LTP upon STET (arrows) that was maintained throughout the recording session (t test, $P = 0.0001$; $n = 30$). B. Lasting LTP induced by STET was not observed in 10-month old APPS1 Δ 9 placebo treated mice. The potentiation decayed to baseline after 3 h (t test, $P = 0.16$; $n = 19$). C. Treatment with anle138b starting at 6 month of age rescues LTP deficit in 10-month old APPS1 Δ 9 mice (t test, $P < 0.0001$; $n = 20$). Triplets of arrows represent STET applied for inducing L-LTP. Insets in each graph represent typical fEPSP traces recorded 15 min before (dotted line), 30 min after (broken line), and 3 h after (full line) STET. D. Escape latency in the Morris water maze test is impaired in placebo treated APP mice and partially restored to WT levels in anle138b treated APP mice (ONE-way ANOVA, $F = 35.94$, $P < 0.0001$; $P = 0.0309$ for APP + anle138b vs. APP + placebo and $P = 0.4$ for APP + placebo vs WT + anle138b, $n = 7$ /group). E. Probe test performed 24 h after the last training session. The lower panel shows representative swimming path during the probe test. T = target quadrant compared vs. other quadrants (t test, ** $P < 0.001$; * $P < 0.05$) F. Average swim speed during water maze training. G. Explorative behavior in the open field test. Upper panel: Representative motion tracks during the test session. Lower panels show the total distance traveled during the 5 min test session. H. Bar graph showing the time spent in the center vs. the corner of the open field. Error bars indicate SEM.

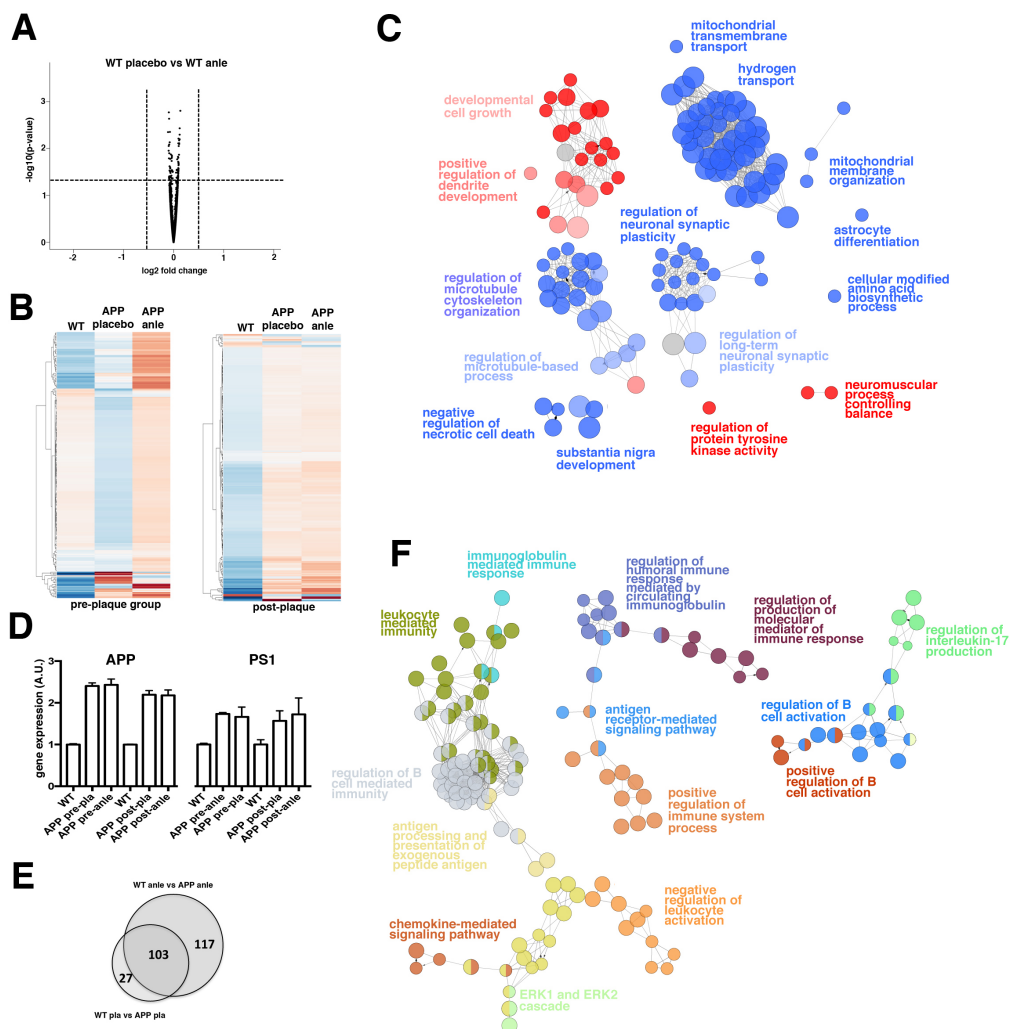


Figure 4.3: Hippocampal gene-expression in anle138b treated mice. **A.** Volcano plot comparing gene-expression in WT mice treated with placebo or anle138b. There is no statistically significant difference (indicated by the dashed lines) amongst groups. **B.** Left panel: Heat map showing differentially expressed genes in placebo treated WT and APP mice and anle138b treated APP mice of the pre-plaque group. Note that there is a WT-like gene-expression pattern is to a large extent reinstated in anle138b treated APP mice. Right panel: Heat map showing differentially expressed genes in placebo treated WT and APP mice and anle138b treated APP mice of the post-plaque group. **C.** Pathways down-regulated (blue) or up-regulated (red) in placebo treated APP mice when compared to WT control group. **D.** Expression of APP and PS1 genes in WT and transgenic mice, placebo or anle138b treated. Note that anle138b treatment does not affect APP or PS1 expression. **E.** Venn diagram showing that 10-month old mice treated with placebo or anle138b show very similar changes in hippocampal gene-expression. **F.** Pathways up-regulated in 10-month old APP mice. Analysis is based on the 220 genes commonly increased in placebo and anle138b treated APP mice. Note that the pathways are exclusively linked to neuroinflammation. Error bars indicate SEM.

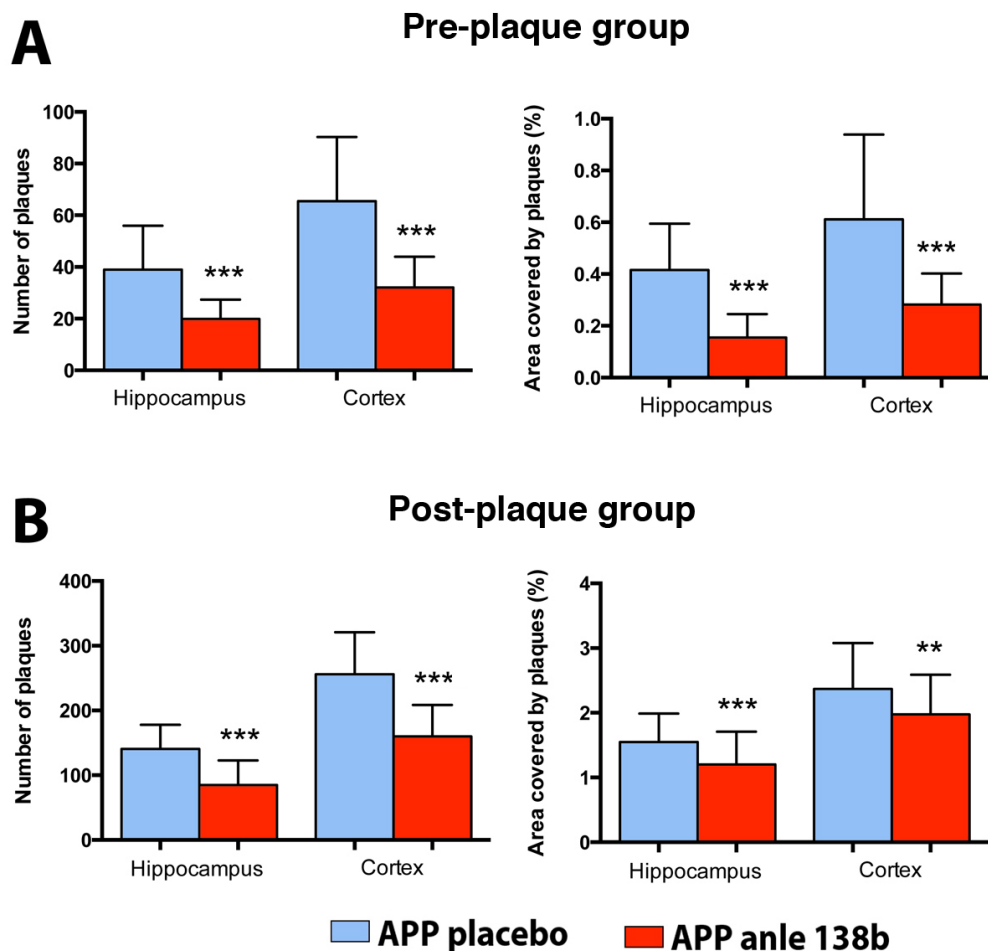


Figure 4.4: Amyloid plaque pathology is ameliorated by anle138b treatment in the pre-plaque (A) and post-plaque (B) groups. A. Reduced amyloid pathology as indicated by reduced number of plaques (left panel) and reduced area covered by plaques (right panel) in the pre-plaque group (t test *** $P < 0,0001$, $n = 5$ /group). B. Reduced amyloid pathology as indicated by reduced number of plaques (left panel) and reduced area covered by plaques in the post-plaque group (t test *** $P < 0,0001$, *** $P < 0.01$ $n = 5$ /group). Error bars indicate SEM.

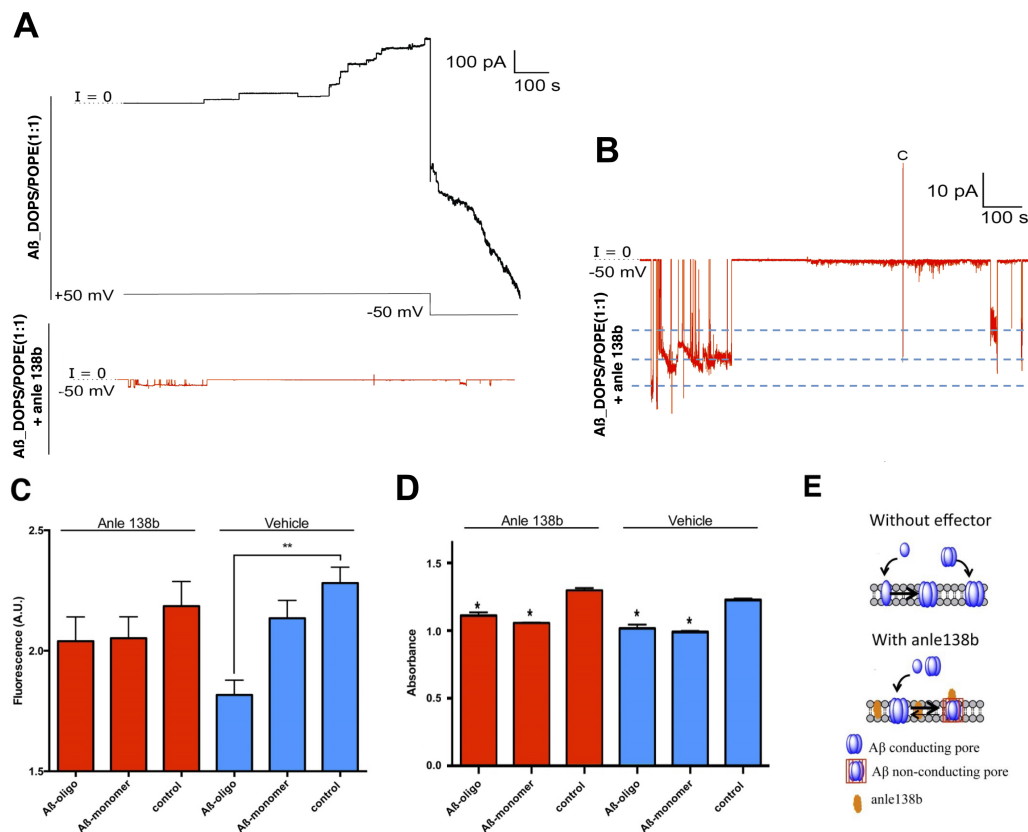


Figure 4.5: Anle138b ameliorates $A\beta_{1-42}$ induced membrane integrity. A. $A\beta_{1-42}$ induces pore-like step ionic current increases across lipid bilayer membranes and grows with inverted sign after voltage inversion to amplifier saturation current. B. In the presence of anle138b, the current does not increase beyond 30 pA. Discreet conductance levels are highlighted suggesting multiple opening and closing events for three individual pores. C. Hippocampal neurons (DIV 10) were treated with Anle138b (1 μ M) or vehicle before $A\beta_{1-42}$ oligomers or monomers were added (10 μ M, n=4/group). After 48 h membrane integrity, was measured as fluorescence intensity using a CyQUANT assay (Thermo Fisher). In the vehicle group, membrane integrity was significantly impaired when treated with $A\beta$ oligomers comparing with control neurons or $A\beta$ monomer treated neurons, anle138b treated neurons did not exhibit a difference between addition of $A\beta$ monomers or $A\beta$ oligomers. (t test, $**P < 0,01$). D. Same experimental setting as in (C) but cell viability was measured using the MTT assay (t test, $*P < 0,05$ vs. control). No difference in cell viability was observed for $A\beta$ monomer or oligomer treatment in the absence or presence of anle138b. E. Schematic of potential mechanisms of activity inhibition for anle138b. In the absence of anle138b, $A\beta$ monomers and/or oligomers insert in the membrane and form conducting pores. Treatment with anle138b renders these conductive channels inactive most probably due to reduced life time of the open state. Error bars indicate SEM.

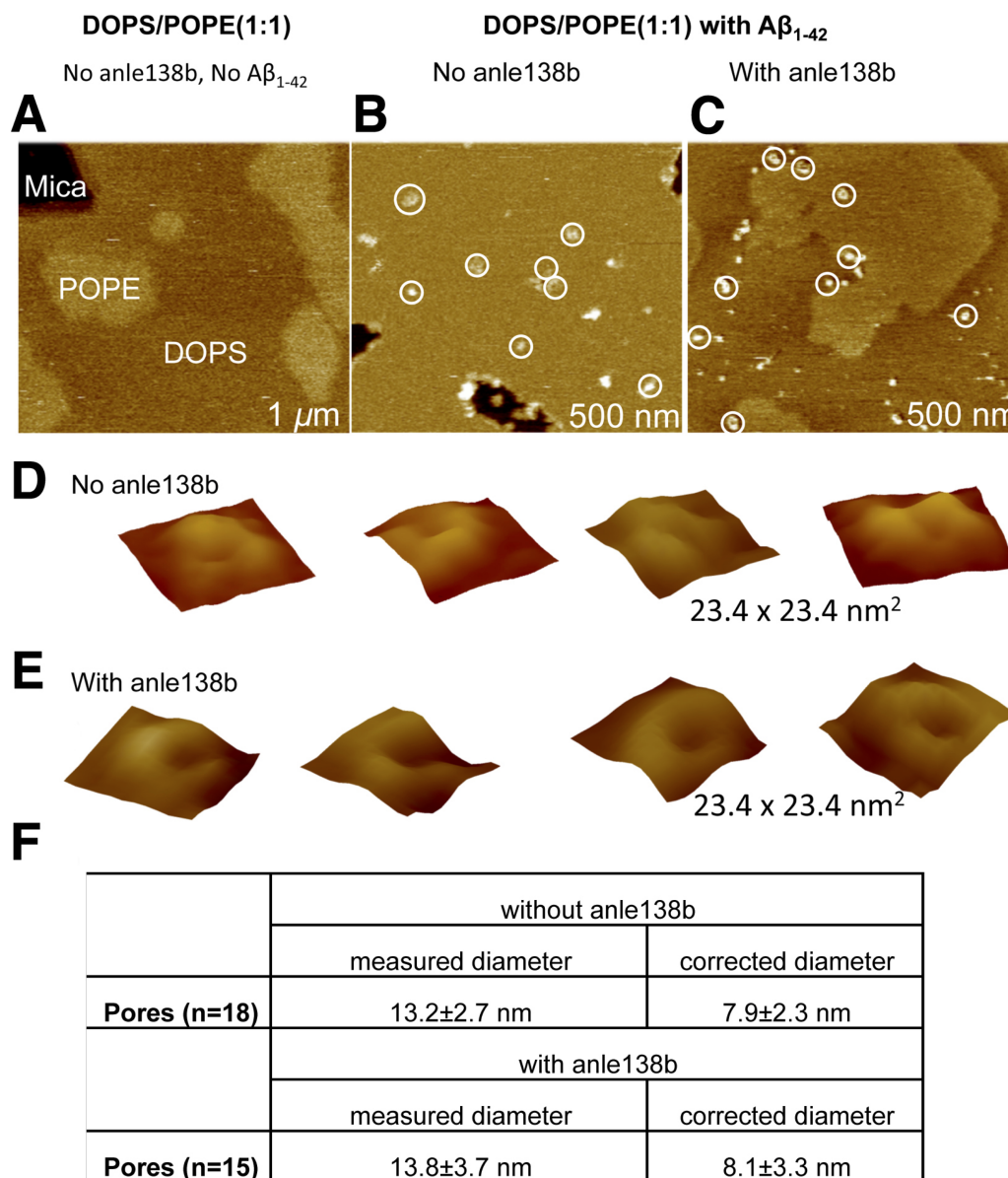


Figure 4.6: Observation of A β pores by AFM in anle138b-doped membranes. A-C: AFM tapping mode images showing similar pore structures in membranes with and without anle138b. A. POPE/DOPS (1:1) membranes without compound and not exposed to A β ₁₋₄₂ showing lateral phase separation. B. Membrane with the same lipid composition as in a) without compound reconstituted with A β ₁₋₄₂ at a 1:60 peptide/lipid molar ratio. C. Membrane with the same lipid composition as above with anle138b (10 mM with respect to lipid volume) and reconstituted with A β ₁₋₄₂ (1:60 peptide/lipid molar ratio). D, E. Four representative pores extracted from (B) and (C), respectively. F. Table summarizing that A β pores show the same dimension in the presence or absence of anle138b.

Chapter 5

Nanofiber optic force transducers with sub-piconewton resolution via near-field plasmon-dielectric interactions.

5.1 Abstract

Ultrasensitive nanomechanical instruments, including the atomic force microscope (AFM)[166, 26, 167, 168] and optical/magnetic tweezers[169, 170, 171, 172], have helped shed new light on the complex mechanical environments of biological processes. However, it is difficult to scale down the size of these instruments due to their feedback mechanisms[173], which if overcome would enable high-density nanomechanical probing inside of materials. A variety of molecular force probes including mechanophores[174], quantum dots[175], fluorescent pairs[176, 177], and molecular rotors[178, 179, 180] have been designed to measure intracellular stresses; however, fluorescence-based techniques can have short operating times due to their photo-instability and it is still challenging to quantify the

forces with high spatial and mechanical resolution. Here we develop a compact nanofiber optic force transducer (NOFT) that utilizes strong near-field plasmon-dielectric interactions to measure local forces with a sensitivity of <200 fN. The NOFT system is tested by monitoring bacterial motion and heart cell beating as well as detecting infrasound power in solution.

5.2 Introduction

The design and working principle of the NOFT is shown in Fig. 5.1a. SnO₂ nanofiber waveguides (WGs)[181] were placed on a substrate (silica or quartz) and gold nanoparticles (~ 80 nm diameter) were directly attached to the bare nanofiber via electrostatic forces to serve as reference nanoparticles ($\text{NP}_{reference}$). The sensor nanoparticles (NP_{sensor}) were designed by covalently linking cystamine-functionalized gold nanoparticles to a polyethylene glycol (PEG) monolayer grafted to the WG. The scattering intensity of NP_{sensor} is strongly dependent on the WG-NP separation distance. Therefore, to quantitatively read-out forces on NP_{sensor} via an optical signal, a link must be established between 1) the scattering intensity and polymer thickness and 2) the polymer thickness and the force applied on the nanoparticle. Both of these links can be achieved by initiating an accurate calibration model. We have statistically measured a 0.55 ± 0.05 ratio of the average scattering intensities between NP_{sensor} and $\text{NP}_{reference}$ (Fig. 5.1b) and determined that the mechanical stiffness of the PEG films is stable up to two weeks when kept in PBS solution (Fig. 5.4).

5.3 Results

White defect emission can be launched down the WG by exciting one end with a light source above the band gap of SnO₂(3.6 eV)[181]. Since the position of the plasmonic nanoparticles can be optically tracked in the far-field with angstrom-level spatial resolution[182], forces on the nanoparticles can be extracted by monitoring the scattering intensity assuming the mechanical properties of the polymer cladding are well characterized. The force sensitivity of the NP_{sensor} can be calculated by multiplying the distance sensitivity ($D_{sensitivity}$) and the spring constant (k_{PEG}) of the PEG film. $D_{sensitivity}$ is determined by the minimum discernible intensity and the relationship between intensity and distance, such that $D_{sensitivity} = (\Delta\sigma/\mu)/S_{distance}$, where $\Delta\sigma/\mu$ is the change in the coefficient of variation from the scattering intensity of NP_{sensor}, and $S_{distance}$ is the local slope of the scattering intensity vs. nanoparticle-WG distance curve. As shown in Fig. 5.1c, the curves of σ/μ vs. μ for both NP_{reference} and NP_{sensor} follow similar trends indicating that there is no observable thermal-related vibration from NP_{sensor} on the polymer. This is likely due to the dense polymer brush underneath NP_{sensor} and an increased drag coefficient close to the surface[183, 184]. From the noise level of these two curves, $\Delta\sigma/\mu$ is consistently centered at 0.005, independent of whether there is a PEG layer underneath or not.

An AFM integrated with an optical microscope was used to calibrate the force response of the NOFT. Due to the difficulty of reproducibly applying force directly on a NP_{sensor} with a bare AFM tip, which often caused the nanoparticle to dislodge from the polymer film (Fig. 5.5), we simultaneously measured the optical signal from a single nanoparticle-modified AFM tip (spring constant $k = 9.4$ pN/nm) and force-distance curves. Previous work showed that the AFM tip does not influence the scattering intensity during interaction of the nanoparticle with the WG (Fig. 5.6)[185]. As the modified tip approaches

the WG, the scattering intensity increases, plateauing with larger intensity fluctuations when the polymer is fully compressed (Figs. 5.1e and 5.7). The increased modulation is likely caused by small sliding of the tip along the WG surface (contacting slightly different regions of the nanofiber)[186].

The force-scattering intensity vs. time retraction curve (latter 50 s in Fig. 5.1e) can be converted to force-scattering intensity vs. distance (Fig. 5.1f) since the speed of the cantilever is known. During retraction of the AFM tip, we observed a 30% drop in the intensity (decay constant of 33 nm) from its maximum point within 10 nm, which corresponds to the thickness of the PEG monolayer in the force curve. We obtained an average PEG thickness of 15 ± 1 nm and a PEG chain density of 0.036 ± 0.006 chains/nm² by fitting the force curve with an Alexander-de Gennes model for brush polymers[25, 187] (Fig. 5.8). From the scattering intensity profile, a NP_{sensor} sitting on a 15 nm thick PEG film corresponds to a 55% decrease in scattering intensity compared to NP_{reference}, agreeing well with the measured scattering intensity ratio in Fig. 5.1b. This result indicates that the NOFT platform detects forces prior to the AFM, and demonstrates that the AFM indentation experiments underestimate (10 nm) the real thickness of the PEG film (15 nm) underneath NP_{sensor}. From the scattering-distance relationship we extracted a value of 0.019 nm^{-1} for $S_{distance}$ and 2.6 \AA for $D_{sensitivity}$ at a distance of 15 nm from the WG. We obtained a value of ~ 160 fN for the force sensitivity ($F_{sensitivity}$) using Alexander-de Gennes' model and evaluating the first derivative of the force at the contact point ($k_{PEG} = 6.3 \times 10^{-4} \text{ nN/nm}$).

To demonstrate the performance of the calibrated NOFT in quantifying forces[188], we placed NOFTs in a solution of *Helicobacter pylori* (*H. pylori*) bacteria (Fig. 5.2a). We recorded the scattering intensity of NP_{sensor} with and without bacteria (see Methods) and plot the relationships of σ/μ vs. μ in Fig. 5.2b. Because UV excitation can induce

some fluorescence, causing a slight increase in background noise, we developed a statistical method to discriminate the background noise from the true signal. When the background noise δ is small compared to the signal, σ/μ increases linearly with respect to $1/\mu^2$ (Fig. 5.2c). The slopes of the lines reflect the noise level of the system, and the intercept with the vertical axis corresponds to the root mean square (r.m.s.) of the deformation depth ratio $\sqrt{\Delta t^2}$ (the ratio of the distance fluctuation Δx to 33 nm, which is the scattering decay constant of the nanoparticle). When active bacteria are present, $\sqrt{\Delta t^2}$ increases by 0.016, which translates to a force of ~ 400 fN by the bacteria (a very similar value to the propulsion force of a single bacterium[189]).

The detected force is likely due to i) the microflow forces induced by bacteria swimming in the vicinity of NP_{sensor} , and/or ii) the interaction of bacteria with the PEG cladding, thus producing oscillations of NP_{sensor} . A direct collision between a bacterium and NP_{sensor} is unlikely to occur due to the small cross-section of NP_{sensor} . As described in the method section, our estimation shows $N = 1.7 \times 10^{-6}/s$. Accordingly, no binding of the bacteria to the NOFT was observed (Fig. 5.9).

To verify that the measured force originated from motion of the bacteria, and not Brownian forces, dead bacteria were tested, resulting in a similar optical response as bacteria-free experiments (Fig. 5.10). These results were compared with AFM measurements (Fig. 5.2d). The RMS of the AFM cantilever deflection in a solution without bacteria was 0.55 \AA (Fig. 5.2e) giving a RMS force sensitivity of $2.2 \pm 0.2 \text{ pN}$ ($k = 40 \text{ pN/nm}$). After adding bacteria, the induced force was approximately 10 pN (Fig. 5.2f). Interestingly, the calculated average stress on NP_{sensor} is four orders of magnitude higher than on the AFM cantilever (A detail description is shown in the method section). This is likely due to the small size of the nanoparticle (i.e., small drag coefficient) which doesn't filter as much of the higher

frequency signals as the bulk cantilever[190]. This demonstrates that the NOFT is capable of monitoring sub-pN forces from microorganisms in a dynamic environment.

We subsequently explored the ability of the NOFT to detect acoustic signatures from both micromechanical and biomechanical systems[191]. An AFM tip was employed to generate small acoustic oscillations near a NP_{sensor} by vertical modulation at low frequencies (Fig. 5.3a). The small applied forces (~ 300 pN) did not produce any measurable vibration of the WG (Figs. 5.11 and 5.12), but once the tip was moved close to NP_{sensor} (at a distance of ~ 500 nm), Fourier transforms of the scattering intensity resolved the oscillation frequencies of 1 Hz and 2 Hz that were applied to the AFM cantilever (Fig. 5.3b). From these experiments we estimate that the NOFT can detect sound pressure levels down to -30 dB in water.

With this sensitivity, acoustic signatures from many different biomechanical systems could be detectable. To explore this we placed a NOFT $\sim 100 \mu\text{m}$ away from a small assembly of neonatal mouse cardiomyocytes (Fig. 5.3c) and resolved beating frequencies of 1-3 Hz from the cells (Fig. 5.3d)[192]. We also observed that the cardiomyocytes stopped beating after about 30 min as the cell culture solution cooled down[193] (Fig. 5.13). The large spread in beating frequency is anticipated (supported by results from optical imaging techniques) as a smaller array does not have complete coherence and will show cycling variations from cell to cell. This demonstrates that the NOFT platform is quite versatile and could lead to *in vivo* stethoscopic applications.

5.4 Conclusion

In summary, we developed a novel NOFT platform that leverages the optical response of plasmonic nanoparticles attached to a compressible cladding embedded in the evanescent field of a nanofiber. We achieved angstrom-level distance sensitivity and a force sensitivity

of 160 fN. After fully calibrating the system, the NOFT was used to detect sub-pN forces from the swimming action of bacteria, and acoustic signatures from beating cardiomyocytes with a sensitivity of -30 dB. With the ability to tune the force and dynamic range via the mechanical response of the compressible cladding, detect forces from multiple nanoparticles on a single fiber, and a geometry that can be inserted into small volumes, NOFT will become a valuable tool for biomechanical and intracellular studies.

5.5 Methods

5.5.1 Integrated AFM/Optical Setup

AFM/optical measurements were done using a Dimension Hybrid XYZ scanner (Bruker, CA) on a Zeiss Axiovert 135TV inverted light microscope (Fig. 5.1d). The AFM scanner was run by Nanoscope software 5.31R1 (Bruker) and has a scan range of 90 x 90 μm^2 . The 325 nm line from a continuous-wave helium cadmium laser (~ 2 mW) was launched through a quartz slide from underneath at an angle of $\sim 45^\circ$ relative to the sample plane. The scattering intensities were collected through a 10x objective with a 600 nm short pass filter and recorded by an EMCCD camera (Andor Technology).

5.5.2 Optical setup for the measurement of bacteria motion force

After placing a SnO₂ nanofiber (via micromanipulation) across a silica trench, it was fixed to the substrate using polydimethylsiloxane (PDMS), and PEG was grafted on the suspended nanofiber. A cured PDMS ring was placed around the channel, forming a reservoir that could be filled with the bacteria solution or just the PBS solution. The bacteria concentration was held fixed at 1.65×10^7 CFU/mL for all experiments. After covering

the PDMS ring with a thin fused silica chip ($\sim 170 \mu\text{m}$ thickness), one end of nanofiber was excited by 325 nm UV light ($\sim 10 \text{ mW}$) at an angle of $\sim 45^\circ$ relative to the sample plane. The scattering intensity signals were collected through a 50x objective and recorded by an EMCCD camera (Andor Technology). The sampling frequency was $\sim 66 \text{ Hz}$, and the recording period was ~ 15 seconds.

5.5.3 Optical setup for the measurement of cell beating frequency

325 μm thick PEG gels containing neonatal mouse cardiomyocytes in a GelMA hydrogel were placed in a microfluidic chamber containing NOFTs in the cell culture solution (74% DMEM Fluobrite, 25% M199 medium without phenol red, 0.5% penicillin/streptomycin solution (Gibco), 0.5% 1 M HEPES buffer). A similar excitation and collection setup to the bacteria experiment was used to detect the beating frequency of the cardiomyocytes. The sampling frequency was $\sim 19 \text{ Hz}$, and the recording period was ~ 52 seconds.

5.5.4 Tin dioxide (SnO_2) nanofiber chip preparation

The SnO_2 nanofiber waveguides (WGs) were synthesized via a thermal vaporization process in the presence of trace amounts of O_2 as described elsewhere.[181] The WGs have cross-section dimensions of 200 - 400 nm. Before placing the SnO_2 nanofiber WGs on a quartz or silica substrate, the substrate was sonicated in ethanol and rinsed thoroughly with deionized (DI) water. The substrates were then placed in a RCA1 solution that consisted of ammonium hydroxide/hydrogen peroxide/DI water (1:1:5 vol/vol), heated at 75°C for 10 min, followed by a rinsing with copious amounts of DI water and dried under airflow. The substrates were then placed in a piranha solution containing sulfuric acid/hydrogen peroxide

(3:1 vol/vol), heated at 75 °C for 10 min, followed by a rinsing with DI water and dried under airflow. After placing the SnO₂ nanofiber WGs on the substrate, the substrate was hydrolyzed under oxygen plasma treatment for 10 minutes, and rinsed with water and dried under airflow. An atomic layer of amine groups was formed on the SnO₂ nanofiber WGs by evaporating aminopropyltrimethoxysilane (APTMS) in a dry box chamber for 1 hour followed by heating at 100 °C for 10 minutes. A solution containing 0.2 mM COOH-PEG-COOH (5 kDa) (Laysan Bio, Inc), 1 mM EDC, and 1 mM TEA in DMF was placed on top of the nanofiber chip overnight to graft PEG monolayer on the nanofiber. The substrate was then rinsed with copious amounts of methanol and blown dry. For the attachment of gold nanoparticles on the PEG layer of the WGs, 1 mL of a citrate-capped gold nanoparticle solution ($\sim 7.8 \times 10^9$ particles/ml, ~ 80 nm nominal diameter, Sigma-Aldrich) was first mixed with 1 mL of DI water containing 7.5 mg of cysteamine and stirred for 1 hour to functionalize the gold nanoparticles with thiol groups. After centrifugation and rinsing with DI water (x3), the nanoparticles were covalently linked to the carboxylate groups on the PEG polymer via EDC and NHS chemistry.

5.5.5 Alexander-de Gennes force model

The Alexander-de Gennes force model calculates the force between two equal surfaces containing polymer brushes using scaling laws.[187] Butt *et al.* derived an equation for only one polymer-coated surface [194]:

$$F = 50k_BTR_TL_0\sigma^{3/2}e^{-2s\pi/L_0} \quad (5.1)$$

where F is the force, k_B is the Boltzmann constant, T is the temperature (room temperature for our measurements), R_T is the radius of tip 40 nm, s is the separation between the AFM tip and substrate, L_0 is the thickness of the polymer, and σ is the polymer chain density. L_0 and σ are the fitting parameters. This model works in the distance range of $0.2 < \frac{s}{L_0} < 0.9$. The fittings were done for 10 different force curves with an error of $< 1\%$.

5.5.6 Preparation of *H. pylori* bacteria

H. pylori Sydney strain 1 (SS1) was used in this study. The bacteria were maintained on a Columbia agar supplemented with 5% (vol/vol) laked horse blood at 37 °C under microaerobic conditions (10% CO₂, 85% N₂, and 5% O₂), as previously described.[195] For experiments, fresh colonies of *H. pylori* bacteria were subcultured from the agar plates in BHI broth containing 5% (vol/vol) fetal bovine serum (FBS) and cultured overnight at 37 °C under microaerobic conditions with moderate reciprocal shaking. The bacteria were harvested by centrifugation at 4,000 x g for 10 min, resuspended and adjusted to a concentration of 1.65×10^7 CFU/mL (determined by OD₆₀₀ measurement, OD₆₀₀ = 1.0 corresponding to $\sim 1 \times 10^8$ CFU/mL) using phosphate-buffered saline (PBS) containing calcium and magnesium. The fluorescein isothiocyanate (FITC) labeled bacteria were prepared using a protocol previously described [196] with some modifications. Briefly, the bacteria suspension was adjusted to 8×10^8 CFU/mL in PBS and 16 μ L FITC (1 mg/mL in DMSO) was added to 8 mL of the bacteria solution and incubated at 37 °C under dark, microaerobic conditions with moderate reciprocal shaking. After 12 h, the FITC-labeled bacteria were washed 3x in PBS with 0.1% Tween-20. Finally, the bacteria were resuspended and the concentration was adjusted to 1.65×10^7 CFU/mL using PBS.

5.5.7 Statistical analysis of scattering intensity

$$t_0 = x_0/33, \quad \Delta t = \Delta x/33, \quad \mu = I_0 e^{-t_0}$$

$$i = \delta + I_0 e^{-(t_0 - \Delta t)} = \delta + \mu e^{\Delta t}$$

$$\begin{aligned} \sigma &= \sqrt{1/N \sum (i - \mu)^2} = \sqrt{1/N \sum (\delta + \mu e^{\Delta t} - \mu)^2} \approx \sqrt{1/N \sum (\delta^2 + \mu^2 \Delta t^2 + 2\mu \Delta t \delta)} \\ \sigma/\mu &= \sqrt{\sum \delta^2 / N \mu^2 + \overline{\Delta t^2} + (2 \sum \Delta t \delta) / N \mu} = \sqrt{\overline{\Delta t^2}} \sqrt{\sum \delta^2 / N \mu^2 \overline{\Delta t^2} + (2 \sum \delta t \delta) / N \mu \overline{\Delta t^2} + 1} \\ &\approx \sqrt{\overline{\Delta t^2}} \left((\sum \delta^2) / 2N \mu^2 \overline{\Delta t^2} + (\sum \Delta t \delta) / N \mu \overline{\Delta t^2} + 1 \right) \approx \sqrt{\overline{\Delta t^2}} + (\sum \delta^2) / 2N \mu^2 \sqrt{\overline{\Delta t^2}} \end{aligned} \quad (5.2)$$

Here x_0 is the average distance of NP_{sensor} away from the waveguide, Δx is the instantaneous distance fluctuation of NP_{sensor} on the polymer, i is the instantaneous scattering intensity of NP_{sensor}, and I_0 is the average intensity of NP_{reference} directly on the waveguide. t_0 and Δt are the ratio of x_0 and Δx with respect to the nanoparticle scattering decay constant (~ 33 nm), respectively. μ is the average scattering intensity, σ is the standard derivation of the scattering intensity, δ is the instantaneous background noise of the system, and N is the number of data points in the time course. Taylor expansions were used for $e^{\Delta t}$ and $\sqrt{\sum \delta^2 / N \mu^2 \overline{\Delta t^2} + (2 \sum \delta t \delta) / N \mu \overline{\Delta t^2} + 1}$ to give the approximate solutions. The term $(\sum \delta t \delta) / N \mu \overline{\Delta t^2} + 1$ is considered negligible because Δt is a small ratio and δ is a random number around zero.

5.5.8 Number of bacteria (N) directly interacting with nanoparticle per second

$$N = \frac{area \times v}{V} \times (c \times V) = area \times v \times c \quad (5.3)$$

where the surface area of NP_{sensor} is $\sim 2 \times 10^4 \text{ nm}^2$, v is the speed of bacteria $\sim 5.2 \text{ }\mu\text{m/s}$ [average velocity tracked from video recording which is comparable to values reported for *H. pylori* ($\sim 20 \text{ }\mu\text{m/s}$ at $25 \text{ }^\circ\text{C}$) [197] and other bacteria [198]], c is the concentration of bacteria $\sim 1.65 \times 10^7 \text{ CFU/ml}$, V is the volume of the bacteria solution, therefore $N = 1.7 \times 10^{-6} \text{ bacteria/s}$.

5.5.9 Force detection with a free-standing AFM cantilever

After immersing an AFM cantilever (spring constant $k = 40 \text{ pN/nm}$) in PBS buffer for 1 hour to stabilize the system, the deflection sensitivity of the cantilever was measured, and the cantilever was moved away from the surface so that the deflection feedback could be measured. The imaging size was set to zero and the deflection data were recorded with/without bacteria at room temperature.

5.5.10 Average stress applied on NP_{sensor} and AFM cantilever

The spring constant (k) for a rectangular beam can be derived from Euler-Bernoulli beam theory [199],

$$k = \frac{Ewt^3}{4L^3} \quad (5.4)$$

where E is the Young's modulus of the beam, w is the width of the beam, t is the thickness of beam, L is the length of the beam. Therefore, the average stress (q) applied on the rectangular cantilever beam [200] can be expressed as:

$$q(\text{AFM cantilever}) = \frac{8kx}{3lw} = 4.7 \times 10^{-9} \text{ pN/nm}^2 \quad (5.5)$$

where x is the average fluctuation of the cantilever beam. The cross-section area of NP_{sensor} is $\sim 5 \times 10 \text{ nm}$, therefore the average stress applied on the NP_{sensor} can be expressed as:

$$q(NP_{sensor}) = \frac{kx}{area} = 8.1 \times 10^{-5} \text{ pN/nm}^2 \quad (5.6)$$

5.5.11 Sound pressure level estimation using an oscillating AFM tip

We assumed a sphere of radius of $2.2 \mu\text{m}$ (same volume as the AFM tip) was oscillated at a frequency of $1 \text{ Hz} \sim 500 \text{ nm}$ away from a NP_{sensor} . With this assumption the sound pressure could be estimated using the following expression [201]:

$$p = \frac{\rho_0 a^3 \cos\theta}{2r^2} \frac{dv}{dt} \quad (5.7)$$

where a is the radius of the sphere, ρ_0 is the density of water, θ is the angle between the sphere oscillation direction with the line between oscillation center and nanoparticle, r is the distance between the oscillating sphere and the nanoparticle, and dv/dt is the acceleration of the oscillation. The sound pressure level (SPL) can be expressed in decibels:

$$SPL = 20 \times \log_{10}\left(\frac{p}{p_{ref}}\right) \quad (5.8)$$

where the reference pressure $p_{ref} = 1 \times 10^{-6} \text{ N/m}^2$ in water. Thus the estimated SPL that the NOFT detect is $\sim -30 \text{ dB}$.

5.5.12 Cardiomyocytes sample preparation Gelatin

Gelatin methacrylate (GelMA) was synthesized as previously described.[202] Gelatin (10% wt/vol, Type A, 300 Gel Strength, Sigma-Aldrich) was dissolved in Dulbeccos phos-

phate buffered saline (DPBS, Gibco). The solution was allowed to stir for 1 hour at 60 °C and subsequently degassed and purged with argon. Methacrylic anhydride (Sigma-Aldrich) was added to the solution at a rate of 0.5 mL/min to a final concentration of 8% (vol/vol). The solution was stirred for 3 hours and diluted 1:1 with warm PBS. The dilute solution was dialyzed against DI water using 13.5 kDa cutoff dialysis tubing (Spectrum Labs) for 1 week at 40 °C. Samples were frozen and free-dried via a lyophilizer (Labconco), and stored at -80 °C until used. Photoinitiator, LAP was synthesized as previously described.[203] A solution of 2,4,6-trimethylbenzoyl chloride (0.018 mol, Acros Organics) was added dropwise to an equimolar amount of dimethyl phenylphosphinate (Sigma-Aldrich). The reaction was stirred continuously for 18 hours at room temperature under argon. The solution was then heated to 50 °C and a four-fold excess of lithium bromide (Sigma-Aldrich) dissolved in 100 mL of 2-butanone was added. After 10 minutes, a solid precipitate formed and the solution was allowed to cool. After 4 hours, the filtrate was washed three times with 2-butanone (Sigma-Aldrich) and vacuum filtered. Neonatal mouse cardiomyocytes (NMVCs) were isolated from the hearts of neonates of CD-1 wild-type mice (Charles River Labs). In brief, hearts were surgically removed from 1-day-old pups and digested in Hank's Balanced Salt Solution (Gibco) with 0.046% Trypsin (Affymetrix) at 4 °C overnight. Blood cells were removed from hearts by type II Collagenase (Worthington) after shaking at 37 °C for two minutes. A heterogeneous cell population containing cardiomyocytes and fibroblasts was isolated after further digestion using type II Collagenase (Worthington) at 37 °C for seven minutes. Fibroblasts were removed by pre-plating for 1.5 hours on 75 cm² plastic tissue culture flasks (Corning) in a humidified incubator at 37 °C with 5% CO₂. Isolated cardiomyocytes were resuspended in dark medium formulated by 75% DMEM and 25% M199 medium containing 10 mM HEPES, 10% horse serum (hyclone), 5% fetal bovine

serum (Gibco), and 1% 100x Penicilin/Streptomycin/L-Glutamine solution (Gibco). A prepolymer solution consisting of 20% polyethylene glycol diacrylate (PEGDA 700 MW, vol/vol, Sigma-Aldrich) and 0.1% LAP (wt/vol) in DPBS was added between 125 μm polydimethylsiloxane (PDMS) spacers and a pretreated 3-(trimethoxysilyl)propyl methacrylate (TMPSA, Sigma-Aldrich) coverslip. A UV lamp (Brand, Intensity) was used to expose the prepolymer solution for 30 seconds, forming a base layer. 10% GelMA (wt%/vol) and 0.2% LAP (wt/vol) was dissolved in DPBS and subsequently mixed 1:1 with NMVCs cell concentrate to produce a final concentration of 5% GelMA (wt%/vol), 0.1% LAP (wt/vol), and 20 million NMVCs/mL. The NMVCs were encapsulated in the GelMA hydrogel 3D printing. First a set of 250 μm PDMS spacers were placed on top of a microscope slide followed by the PEGDA coverslip facing down. The GelMA/NMVCs mixture was then added between the spacers and placed under a custom-build digital micromirror device (DMD) system, which consisted of a LED light source (365 nm; Hamamatsu), a DMD chip (Texas Instruments), motion controller (Newport), and a set of projection optics. A digital bitmap mask in the shape of a square was made in Adobe Photoshop and load ed to the DMD chip. A 3 mm x 3mm x 250 μm slab was exposed to UV light (88 mW/cm²) for 20 seconds, encapsulating NMVCs in the GelMA hydrogel. Constructs were cultured in dark media, replacing the media daily.

5.6 Acknowledgements

Chapter 5, in part, is a reprint of the material as it appreas in Lee, J.*; Huang, Q.*; Arce FT.*; Yoon, I.; Angsantikul, P.; Liu, J.; Shi, Y.; Villanueva, J.; Thamphiwatana, S.; Ma, X.; Zhang, L.; Chen, S.; Lal, R.; Sirbuly, DJ. Nanofibre optic force transducers with sub-piconewton resolution via near-field plasmon-dielectric interactions. *Nature Photonics*

2017 doi:10.1038/nphoton.2017.74 The dissertation author was the primary author of this paper.

The authors acknowledge X. Qu, W. Zhu, S. Ward and J. Friend for helpful discussions. This work was supported by the National Science Foundation (ECCS 1150952) and the University of California, Office of the President (UC-LFRP 12-LR-238415). Grant support from the California Institute of Regenerative Medicine (grant no. RT3-07899) and the National Institutes of Health (grant no. R01EB021857) to S.C. was greatly appreciated. A part of this project was supported by the National Institute on Aging of National Institutes of Health (grant AG028709). This work was performed in part at the San Diego Nanotechnology Infrastructure (SDNI) of UCSD, a member of the National Nanotechnology Coordinated Infrastructure, which is supported by the National Science Foundation (grant no. ECCS-1542148).

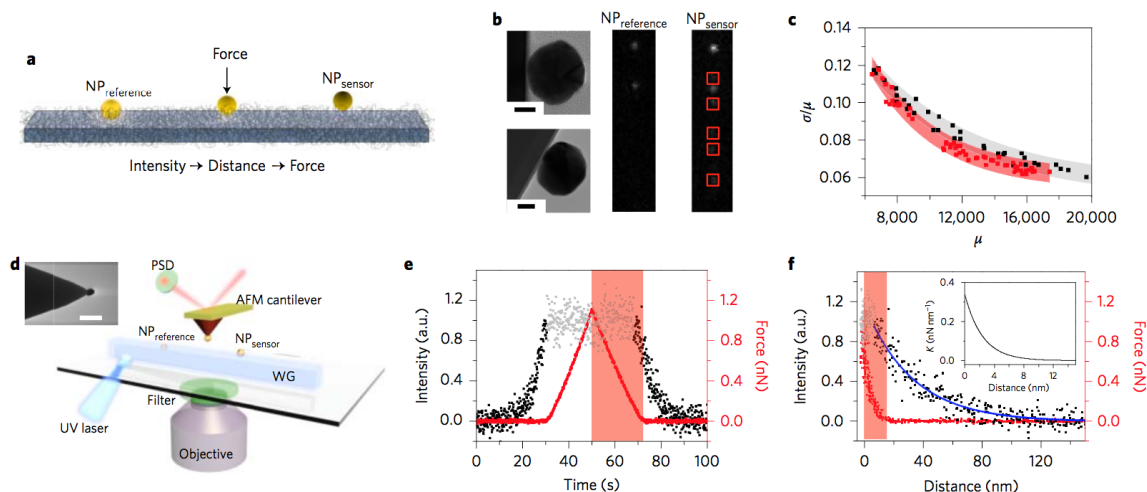


Figure 5.1: Nanofiber optic force transducer calibration. **a**, Schematic showing a $NP_{reference}$ directly on the nanofiber and a NP_{sensor} linked on a compressible PEG film grafted on the nanofiber. The scattering intensity of NP_{sensor} is directly related to its distance from the WG and the distance is strongly dependent on the applied force. **b**, TEM images of a $NP_{reference}$ (top left) and NP_{sensor} (bottom left). Scattering images of two $NP_{reference}$ (middle) and several NP_{sensor} (red boxes) attached to a PEG film in the presence of the $NP_{reference}$ (right). **c**, The relationship between the coefficient of variation (σ/μ) and average scattering intensity (μ) of $NP_{reference}$ (black squares) and NP_{sensor} (red squares). The gray ($NP_{reference}$) and pink (NP_{sensor}) regions are the exponential decay fits to the experimental data with an error of 0.005. **d**, Scheme showing the simultaneous detection of nanoparticle scattering intensity, distance and force with a NP_{sensor} attached either to AFM tip (calibration mode) or PEG film (sensing mode). Inset: SEM image of a single gold nanoparticle attached to an AFM tip. **e**, Relationship of scattering intensity (black dots) and force (red dots) with time. The gray dots indicate the optical saturation region when the PEG layer is fully compressed. **f**, Relationship of scattering intensity (black dots) and force (red dots) with respect to distance. The blue line is an exponential fit to the scattering intensity decay. Inset: relationship between the spring constant k_{PEG} and the distance fitted with Alexander-de Gennes' model (the contact section of the AFM retraction curve is highlighted with a light red box in e and f).

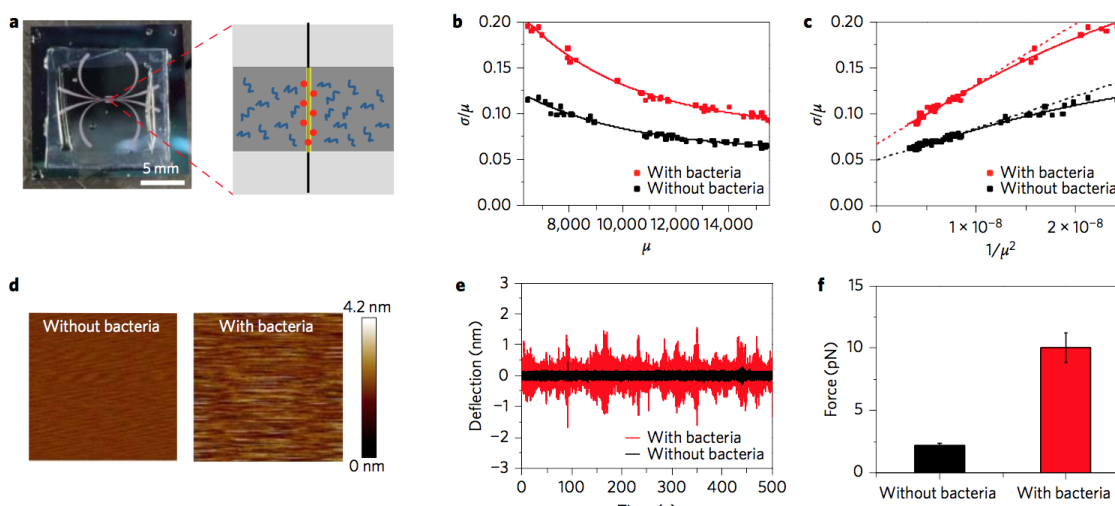


Figure 5.2: Force detection from bacteria motion. **a**, Photograph (left) of a microfluidic chip that houses the NOFT device for detecting the force induced by *H. pylori* bacteria. Schematic (right) showing a zoom in of the NOFT sensor traversing a microfluidic channel. The bacteria (black squiggly lines) periodically swim nearby the NP_{sensor} (red dots) causing optical modulations. **b**, Plot showing the relationship of the coefficient of variation (σ/μ) with respect to average intensity (μ) in phosphate-buffered saline (PBS) without bacteria (black dots) and with active bacteria (red dots). Solid lines are drawn to guide the eye. **c**, Comparison of σ/μ with $1/\mu^2$ in PBS with (red dots) and without (black dots) bacteria. Solid lines are drawn to guide eye. The dashed lines are linear fits to the data points below 1×10^{-8} . **d**, AFM deflection images obtained without feedback control in PBS with (right) and without (left) bacteria. **e**, Time-course of cantilever deflection in PBS with (red) and without (black) bacteria in PBS. **f**, Comparison of measured forces using AFM [deflection RMS multiplied by the spring constant ($k = 40$ pN/nm)] in PBS with (red) and without (black) bacteria. The error bar is the standard derivations from 10 different time-courses.

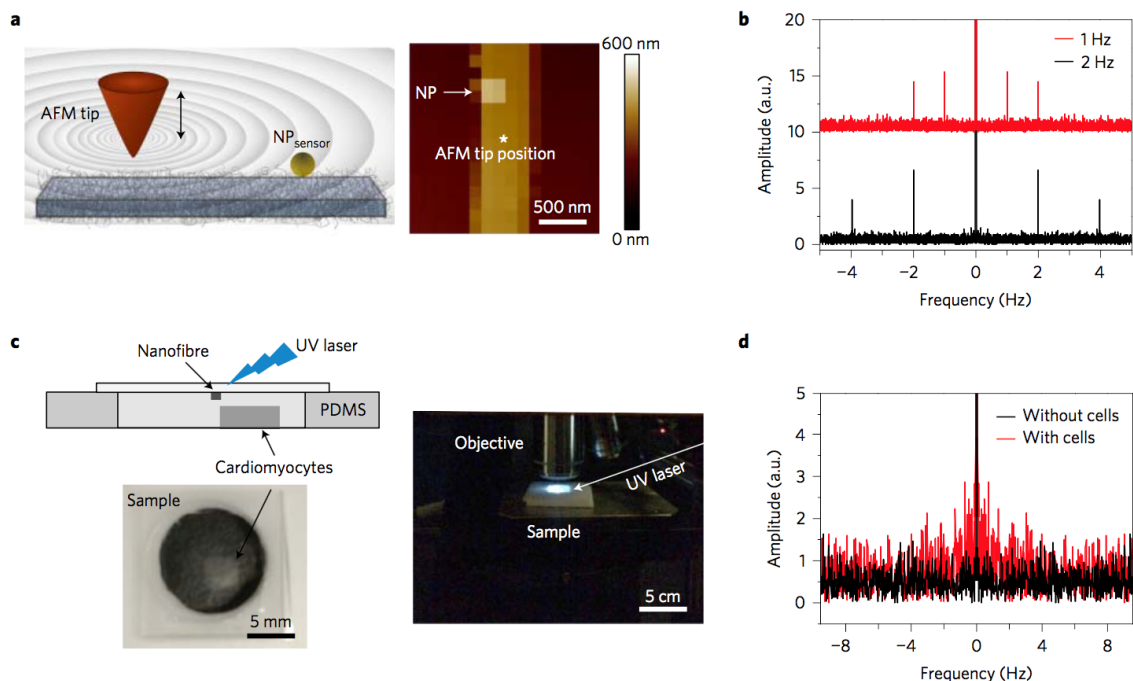


Figure 5.3: Acoustic frequency detection. **a**, (left) Scheme showing an AFM tip acting as an acoustic source nearby a NP_{sensor} . (right) Example of a force mapping image (~ 300 pN force) that was used to locate a NP_{sensor} and then the AFM tip was moved away to generate the acoustic wave. **b**, Fourier transformations of the NP_{sensor} scattering intensity after oscillating the AFM tip at two different frequencies (1 Hz and 2 Hz). **c**, (top left) Cross-sectional side view of the microfluidic chamber used to house the NOFT and cardiomyocyte cluster. The UV laser was focused through the quartz cover onto the NOFT without illuminating the cell culture, and scattering signals were collected back through a top-mounted microscope objective (pictured at right). (bottom left) Optical image of a $3\text{ mm} \times 3\text{ mm} \times 250\text{ }\mu\text{m}$ cardiomyocyte cell cluster that was placed $\sim 100\text{ }\mu\text{m}$ away from the NOFT in the microfluidic chamber. **d**, Fourier transforms taken from the end facet of the NOFT with (red) and without (black) cardiomyocytes.

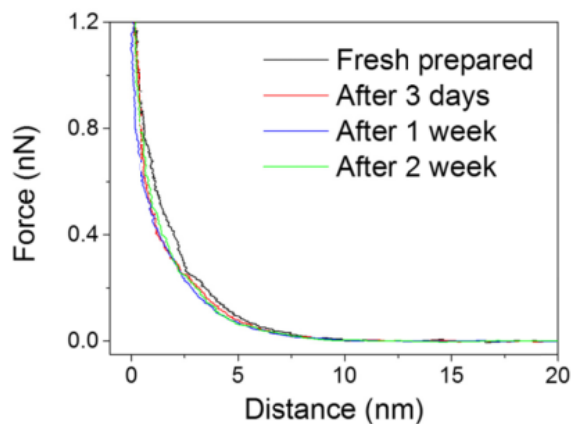


Figure 5.4: Force curves of a PEG monolayer in PBS buffer grown on a silicon substrate. The mechanical stability of the PEG monolayer tracked over two weeks.

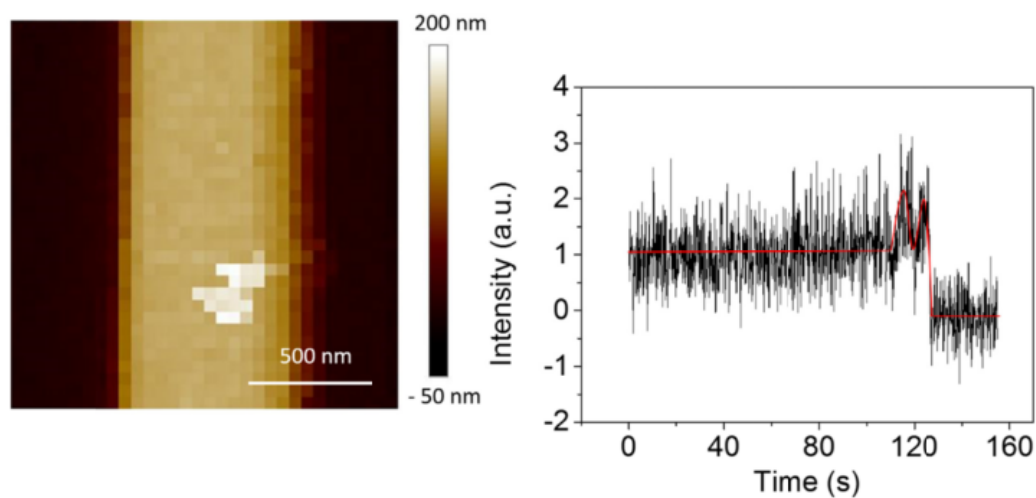


Figure 5.5: A force mapping image of a nanofiber with NP_{sensor} linked on top of a PEG monolayer. (left) A time-course of the optical scattering intensity during the force mapping. The red line is drawn to guide the eye. (right) There is some modulation in the nanoparticle scattering intensity when NP_{sensor} is contacted by the AFM tip. The nanoparticle was eventually moved away by the AFM tip.

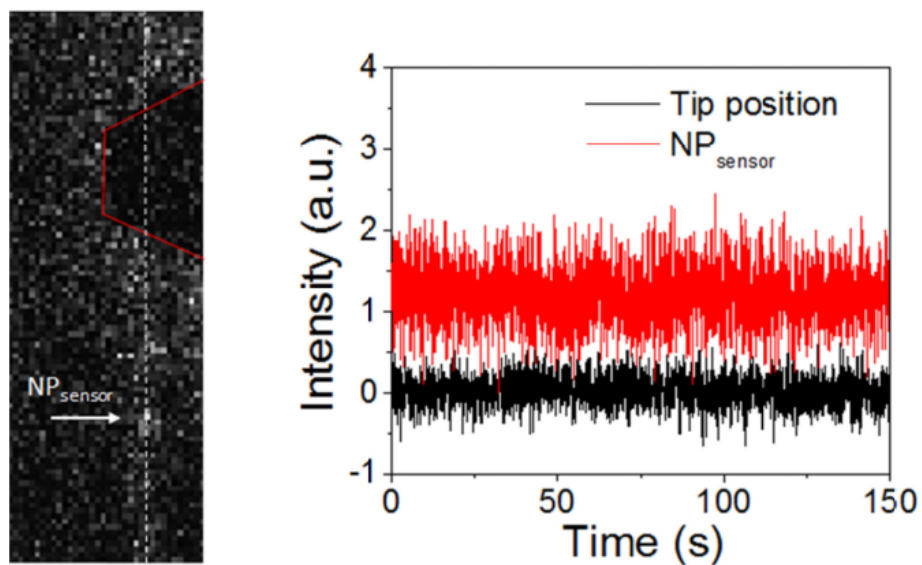


Figure 5.6: Optical image of a bare AFM tip (red outline) indenting on a SnO₂ nanofiber (location denoted by white dotted line).(left) Scattering intensity of a NP_{sensor} on the nanofiber and the AFM tip region during indentation.(right)

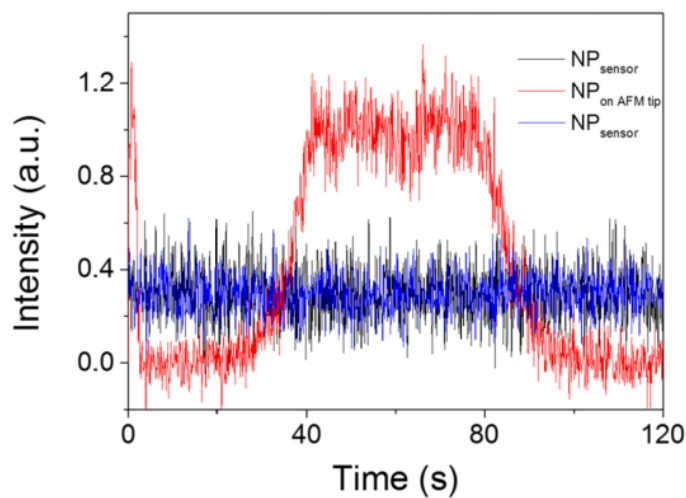


Figure 5.7: Scattering intensities of two NP_{sensor} (black and blue traces) measured simultaneous while a nanoparticle-modified AFM tip (red trace) is indented onto a nanofiber waveguide.

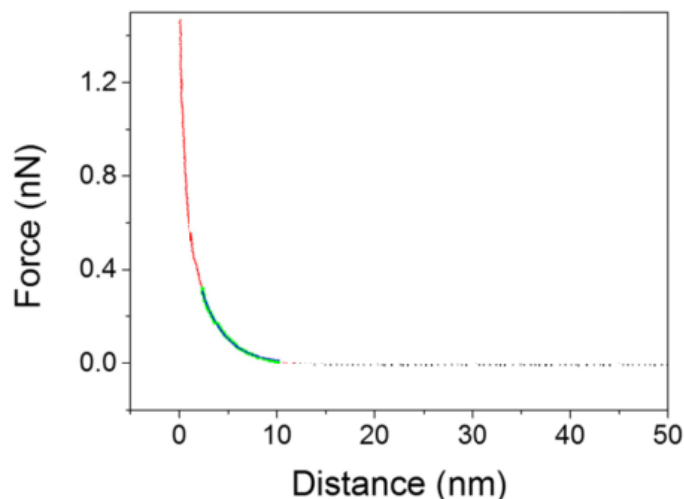


Figure 5.8: Representative force curve of a PEG film using a gold nanoparticle attached to an AFM tip (Black dot). The rising force portion is highlighted with red, and the green portion is the fitting region. The blue line is the fit using Alexander-de Gennes model for a parabolic tip.[187]

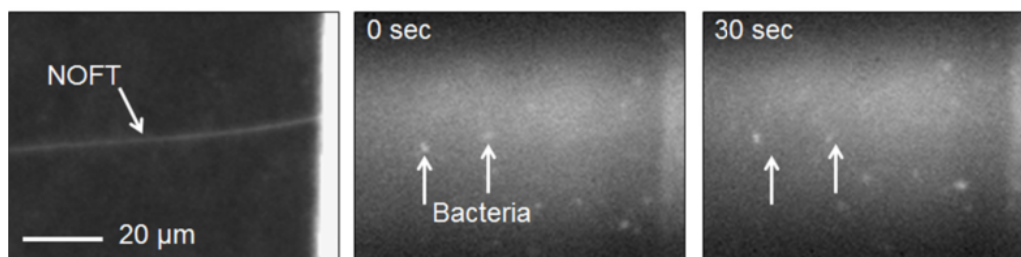


Figure 5.9: (left) Dark-field optical image of a NOFT suspended across a trench (similar to Figure 5.2a in main text). (center/right) Fluorescence images (snapshots from movie) same region as left image) using a 442 nm excitation showing fluorescein isothiocyanate (FITC) labeled *H. pylori*. The 0 second snapshot was taken 30 minutes after the NOFT was first exposed to the bacteria solution. The white arrows are pointing to two bacteria near the NOFT in the center image and are placed in the same location in the right image, showing that the bacteria are still freely moving and no bacteria are bound to the NOFT.

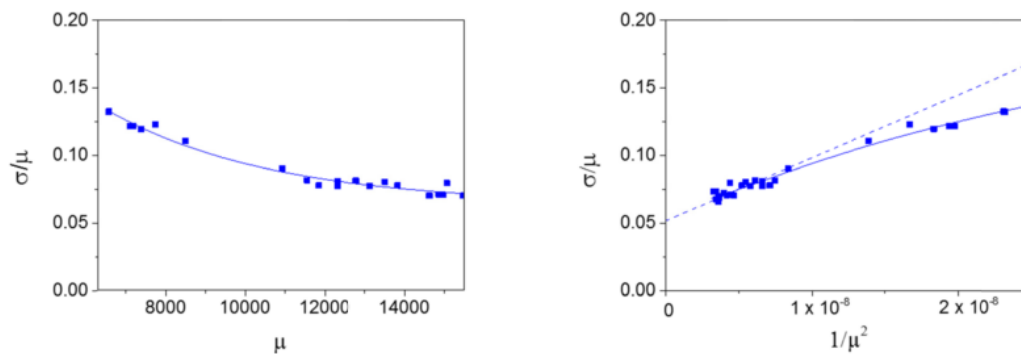


Figure 5.10: (left) Relationship between the coefficient of variation (σ/μ) and the average intensity (μ) in PBS for the dead bacteria (blue dots). The solid line is drawn to guide the eye. (right) Plot of σ/μ vs. $1/\mu$ in PBS with dead bacteria. The solid line is drawn to guide the eye. The dashed lines are linear fits to the data points below 1×10^{-8} . The dead bacteria were fixed with 10% percent Formalin in PBS for 30 minutes.

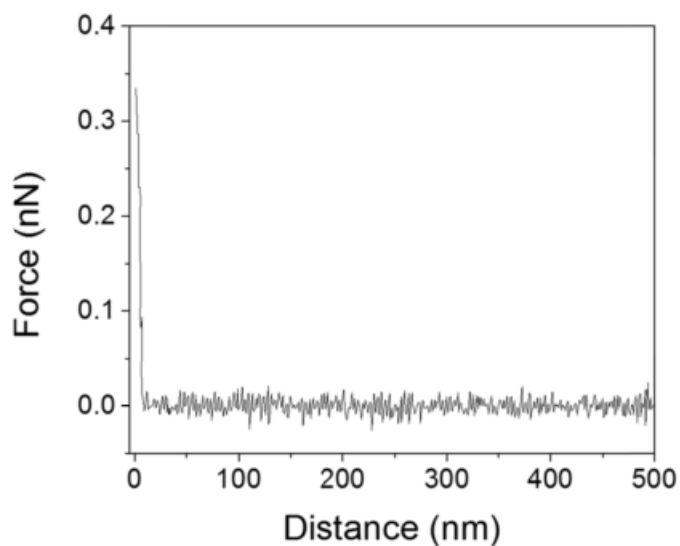


Figure 5.11: Representative force curve of a PEG film on the WG using an AFM tip at a frequency of 2 Hz.

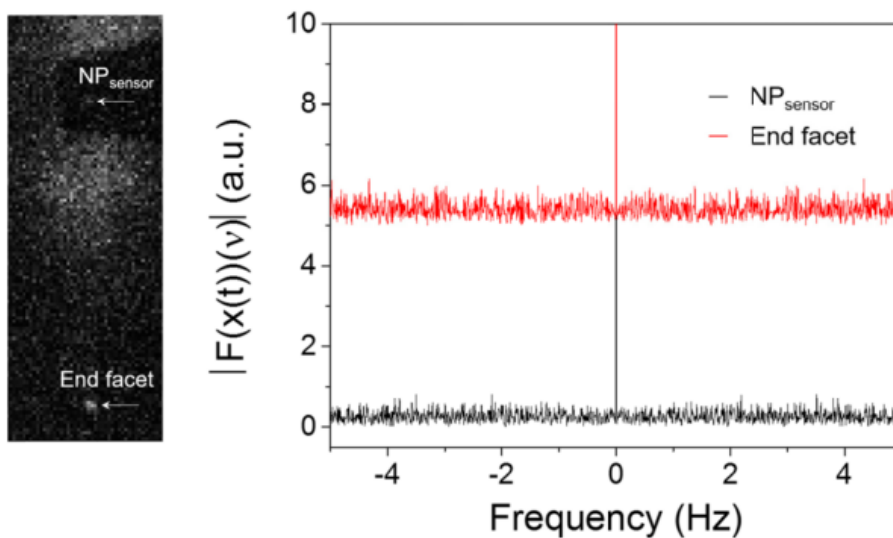


Figure 5.12: (left) Scattering image of NP_{sensor} and end facet when AFM is running force mapping indentation $\sim 2.5 \mu\text{m}$ away from the NP_{sensor} at a frequency of 2 Hz. (right) Fourier transforms taken from the NP_{sensor} (black) and end facet of the NOFT (red). 13

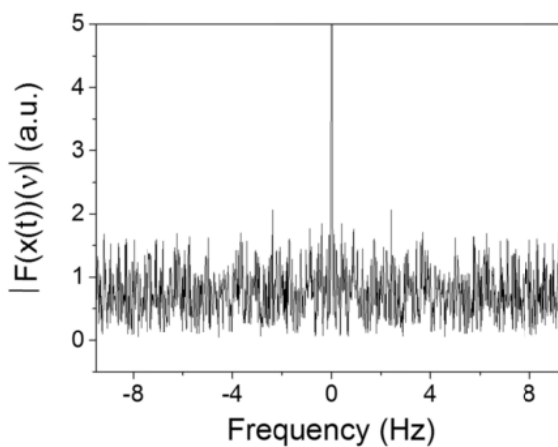


Figure 5.13: Fourier transforms taken from the end facet of the NOFT with the cardiomyocyte cluster after ~ 30 minutes at room temperature.

Bibliography

- [1] Gilbert Di Paolo and Tae-Wan W Kim. Linking lipids to Alzheimer's disease: cholesterol and beyond. *Nature reviews. Neuroscience*, 12(5):284–96, may 2011.
- [2] Fabrizio Chiti and Christopher M Dobson. Protein misfolding, functional amyloid, and human disease. *Annu. Rev. Biochem.*, 75:333–366, jan 2006.
- [3] A S DeToma, S Salamekh, A Ramamoorthy, and M H Lim. Misfolded proteins in Alzheimer's disease and type II diabetes. *Chem. Soc. Rev.*, 41:608–621, 2012.
- [4] G B D 2013 Mortality Collaborators and Causes of Death. Global, regional, and national agesex specific all-cause and cause-specific mortality for 240 causes of death, 19902013: a systematic analysis for the Global Burden of Disease Study 2013. *The Lancet*, 385(9963):117–171, jan 2015.
- [5] Alzheimer's Association*. 2015 Alzheimer's disease facts and figures. *Alzheimer's & Dementia*, 11(3):332–384, mar 2015.
- [6] J. Hardy and G. Higgins. Alzheimer's disease: the amyloid cascade hypothesis. *Science*, 256(5054):184–185, apr 1992.
- [7] John Hardy and Dennis J Selkoe. The amyloid hypothesis of Alzheimer's disease: progress and problems on the road to therapeutics. *Science (New York, N.Y.)*, 297(5580):353–356, jul 2002.
- [8] Robert D. Terry. An honorable compromise regarding amyloid in Alzheimer disease. *Annals of Neurology*, 49(5):684–684, may 2001.
- [9] Karie N Dahlgren, Arlene M Manelli, W Blaine Stine, Lorinda K Baker, Grant A Krafft, and Mary Jo LaDu. Oligomeric and fibrillar species of amyloid- β peptides differentially affect neuronal viability. *Journal of Biological Chemistry*, jun 2002.
- [10] William L Klein, Grant A Krafft, and Caleb E Finch. Targeting small Abeta oligomers: the solution to an Alzheimer's disease conundrum? *Trends in neurosciences*, 24(4):219–24, apr 2001.

- [11] W Blaine Stine, Karie N Dahlgren, Grant a Krafft, and Mary Jo LaDu. In vitro characterization of conditions for amyloid-beta peptide oligomerization and fibrillogenesis. *The Journal of biological chemistry*, 278(13):11612–22, mar 2003.
- [12] Christoph Schmitz, Bart P F Rutten, Andrea Pielen, Stephanie Schäfer, Oliver Wirths, Günter Tremp, Christian Czech, Veronique Blanchard, Gerd Multhaup, Payam Rezaie, Hubert Korr, Harry W M Steinbusch, Laurent Pradier, and Thomas A Bayer. Hippocampal Neuron Loss Exceeds Amyloid Plaque Load in a Transgenic Mouse Model of Alzheimer's Disease. *The American Journal of Pathology*, 164(4):1495–1502, apr 2004.
- [13] Alberto Gómez-Ramos, Miguel Díaz-Hernández, Raquel Cuadros, Félix Hernández, and Jesús Avila. Extracellular tau is toxic to neuronal cells. *FEBS Letters*, 580(20):4842–4850, sep 2006.
- [14] N Arispe, H B Pollard, and E Rojas. Giant multilevel cation channels formed by Alzheimer disease amyloid beta-protein [A beta P-(1-40)] in bilayer membranes. *Proceedings of the National Academy of Sciences*, 90(22):10573–10577, nov 1993.
- [15] Meng-chin Allison Lin and Bruce L Kagan. Electrophysiologic properties of channels induced by A β 25-35 in planar lipid bilayers. *Peptides*, 23(7):1215–1228, 2002.
- [16] Yutaka Hirakura, Rustam Azimov, Rushania Azimova, and Bruce L Kagan. Polyglutamine-induced ion channels: a possible mechanism for the neurotoxicity of huntington and other CAG repeat diseases. *Journal of Neuroscience Research*, 60(4):490–494, may 2000.
- [17] HAI A I Lin, Rajinder Bhatia, and Ratneshwar Lal. Amyloid β protein forms ion channels: Implications for Alzheimer's disease pathophysiology. *FASEB J.*, 15(13):2433–2444, nov 2001.
- [18] Hilal a Lashuel, Peter T Lansbury, and P T Lansbury Jr. Are amyloid diseases caused by protein aggregates that mimic bacterial pore-forming toxins? *Quarterly reviews of biophysics*, 39(2):167–201, may 2006.
- [19] Hyunbum Jang, Jie Zheng, Ratnesh Lal, and Ruth Nussinov. New structures help the modeling of toxic amyloid β ion channels. *Trends in Biochemical Sciences*, 33(2):91–100, feb 2008.
- [20] Hyunbum Jang, Fernando Teran Arce, Srinivasan Ramachandran, Ricardo Capone, Ratnesh Lal, and Ruth Nussinov. β -Barrel Topology of Alzheimer's β -Amyloid Ion Channels. *Journal of Molecular Biology*, 404(5):917–934, dec 2010.
- [21] Laura Connelly, Hyunbum Jang, Fernando Teran Arce, Ricardo Capone, Samuel A Kotler, Srinivasan Ramachandran, Bruce L Kagan, Ruth Nussinov, Ratnesh Lal, F T Arce, Hyunbum Jang, Ricardo Capone, Samuel A Kotler, Srinivasan Ramachandran, Bruce L Kagan, Ruth Nussinov, and Ratnesh Lal. Atomic Force Microscopy and

- MD Simulations Reveal Pore-Like Structures of All-d-Enantiomer of Alzheimer's β -Amyloid Peptide: Relevance to the Ion Channel Mechanism of AD Pathology. *The Journal of Physical Chemistry B*, 116(5):1728–1735, jan 2012.
- [22] Yuri Sokolov, J Ashot Kozak, Rakez Kayed, Alexandr Chanturiya, Charles Glabe, and James E Hall. Soluble Amyloid Oligomers Increase Bilayer Conductance by Altering Dielectric Structure. *The Journal of General Physiology*, 128(6):637–647, dec 2006.
- [23] Isabelle Sponne, Alexandre Fifre, Béatrice Drouet, Christophe Klein, Violette Koziel, Martine Pinçon-Raymond, Jean-Luc Olivier, Jean Chambaz, and Thierry Pillot. Apoptotic neuronal cell death induced by the non-fibrillar amyloid-beta peptide proceeds through an early reactive oxygen species-dependent cytoskeleton perturbation. *The Journal of biological chemistry*, 278(5):3437–45, jan 2003.
- [24] Hyunbum Jang, Fernando Teran Arce, Srinivasan Ramachandran, Ricardo Capone, Ratnesh Lal, and Ruth Nussinov. Structural Convergence Among Diverse, Toxic β -Sheet Ion Channels. *The Journal of Physical Chemistry B*, 114(29):9445–9451, jul 2010.
- [25] Sara M Butterfield and Hilal a Lashuel. Amyloidogenic protein-membrane interactions: mechanistic insight from model systems. *Angewandte Chemie (International ed. in English)*, 49(33):5628–54, aug 2010.
- [26] G Binnig, C F Quate, and Ch. Gerber. Atomic Force Microscope. *Physical Review Letters*, 56(9):930–933, mar 1986.
- [27] a Engel and D J Müller. Observing single biomolecules at work with the atomic force microscope. *Nature structural biology*, 7(9):715–8, sep 2000.
- [28] R Lal and L Yu. Atomic force microscopy of cloned nicotinic acetylcholine receptor expressed in *Xenopus* oocytes. *Proceedings of the National Academy of Sciences of the United States of America*, 90(15):7280–4, 1993.
- [29] Gajendra S Shekhawat, Mary P Lambert, Saurabh Sharma, Pauline T Velasco, Kirsten L Viola, William L Klein, and Vinayak P Dravid. Soluble state high resolution atomic force microscopy study of Alzheimer's beta-amyloid oligomers. *Applied physics letters*, 95(18):183701, nov 2009.
- [30] Rikke Louise Meyer, Xingfei Zhou, Lone Tang, Ayyoob Arpanaei, Peter Kingshott, and Flemming Besenbacher. Immobilisation of living bacteria for AFM imaging under physiological conditions. *Ultramicroscopy*, 110(11):1349–57, oct 2010.
- [31] Daniel J Muller and Yves F Dufrene. Atomic force microscopy as a multifunctional molecular toolbox in nanobiotechnology. *Nat Nano*, 3(5):261–269, may 2008.

- [32] Atsushi Miyagi, Yasuo Tsunaka, Takayuki Uchihashi, Kouta Mayanagi, Susumu Hirose, Kosuke Morikawa, and Toshio Ando. Visualization of intrinsically disordered regions of proteins by high-speed atomic force microscopy. *Chemphyschem : a European journal of chemical physics and physical chemistry*, 9(13):1859–66, sep 2008.
- [33] Kiyohiko Igarashi, Takayuki Uchihashi, Anu Koivula, Masahisa Wada, Satoshi Kimura, Tetsuaki Okamoto, Merja Penttilä, Toshio Ando, and Masahiro Samejima. Traffic Jams Reduce Hydrolytic Efficiency of Cellulase on Cellulose Surface. *Science*, 333(6047):1279–1282, 2011.
- [34] Loredana S Dorobantu, Subir Bhattacharjee, Julia M Foght, and Murray R Gray. Atomic force microscopy measurement of heterogeneity in bacterial surface hydrophobicity. *Langmuir : the ACS journal of surfaces and colloids*, 24(9):4944–51, may 2008.
- [35] J H Hafner, C L Cheung, a T Woolley, and C M Lieber. Structural and functional imaging with carbon nanotube AFM probes. *Progress in biophysics and molecular biology*, 77(1):73–110, jan 2001.
- [36] E L Florin, V T Moy, and H E Gaub. Adhesion forces between individual ligand-receptor pairs. *Science (New York, N.Y.)*, 264(5157):415–7, apr 1994.
- [37] Gopal Thinakaran and Edward H. Koo. Amyloid precursor protein trafficking, processing, and function. *Journal of Biological Chemistry*, 283(44):29615–29619, oct 2008.
- [38] Jean D. Sipe and Alan S. Cohen. Review: History of the amyloid fibril. *J. Struct. Biol.*, 130(2-3):88–98, jun 2000.
- [39] Summer L Bernstein, Nicholas F Dupuis, Noel D Lazo, Thomas Wyttenbach, Margaret M Condron, Gal Bitan, David B Teplow, Joan-Emma E Shea, Brandon T Ruo-tolo, Carol V Robinson, and Michael T Bowers. Amyloid-beta protein oligomerization and the importance of tetramers and dodecamers in the aetiology of Alzheimer’s disease. *Nature Chem.*, 1(4):326–331, 2009.
- [40] S L Bernstein, T Wyttenbach, A Baumketner, J E Shea, G Bitan, D B Teplow, and M T Bowers. Amyloid beta-protein: Monomer structure and early aggregation states of A beta 42 and its Pro(19) alloform. *J. Am. Chem. Soc.*, 127(7):2075–2084, 2005.
- [41] David Eisenberg and Mathias Jucker. The Amyloid State of Proteins in Human Diseases. *Cell*, 148(6):1188–1203, mar 2012.
- [42] C G Glabe. Structural Classification of Toxic Amyloid Oligomers. *J. Biol. Chem.*, 283(44):29639–29643, 2008.

- [43] Hilal A Lashuel, Dean Hartley, Benjamin M Petre, Thomas Walz, Peter T Lansbury, Peter T Lansbury Jr, John Turner, John C King, Tom A Lachlan-cope, and Phil D Jones. Neurodegenerative disease: Amyloid pores from pathogenic mutations. *Nature*, 418(6895):291, jul 2002.
- [44] Arjan Quist, Ivo Doudevski, Hai Lin, Rushana Azimova, Douglas Ng, Blas Frangione, Bruce Kagan, Jorge Ghiso, and Ratnesh Lal. Amyloid ion channels: a common structural link for protein-misfolding disease. *Proceedings of the National Academy of Sciences of the United States of America*, 102(30):10427–32, jul 2005.
- [45] Bruce L. Kagan, Yutaka Hirakura, Rustam Azimov, Rushana Azimova, and Meng Chin Lin. The channel hypothesis of Alzheimer’s disease: current status. *Peptides*, 23(7):1311–1315, jul 2002.
- [46] S Jawhar, O Wirths, and T A Bayer. Pyroglutamate Amyloid-beta (A beta): A Hatchet Man in Alzheimer Disease. *J. Biol. Chem.*, 286(45):38825–38832, 2011.
- [47] T C Saido, W YamaoHarigaya, T Iwatsubo, and S Kawashima. Amino- and carboxyl-terminal heterogeneity of beta-amyloid peptides deposited in human brain. *Neurosci. Lett.*, 215(3):173–176, 1996.
- [48] C Russo, E Violani, S Salis, V Venezia, V Dolcini, G Damonte, U Benatti, C D’Arrigo, E Patrone, P Carlo, and G Schettini. Pyroglutamate-modified amyloid beta-peptides - A beta N3(pE)-strongly affect cultured neuron and astrocyte survival. *J. Neurochem.*, 82(6):1480–1489, 2002.
- [49] T C Saido, T Iwatsubo, D M Mann, H Shimada, Y Ihara, and S Kawashima. Dominant and differential deposition of distinct beta-amyloid peptide species, AbetaN3(pE), in senile plaques. *Neuron*, 14(2):457–466, 1995.
- [50] A Relini, O Cavalleri, R Rolandi, and A Gliozzi. The two-fold aspect of the interplay of amyloidogenic proteins with lipid membranes. *Chem. Phys. Lipids*, 158(1):1–9, 2009.
- [51] Fernando Terán Arce, Hyunbum Jang, Srinivasan Ramachandran, Preston B. Landon, Ruth Nussinov, and Ratnesh Lal. Polymorphism of amyloid β peptide in different environments: implications for membrane insertion and pore formation. *Soft Matter*, 7(11):5267, 2011.
- [52] Y Miller, B Ma, and R Nussinov. Polymorphism in Alzheimer A beta Amyloid Organization Reflects Conformational Selection in a Rugged Energy Landscape. *Chem. Rev.*, 110(8):4820–4838, 2010.
- [53] H Jang, L Connelly, F T Arce, S Ramachandran, B L Kagan, R Lal, and R Nussinov. Mechanisms for the Insertion of Toxic, Fibril-like beta-Amyloid Oligomers into the Membrane. *J. Chem. Theory Comput.*, 9(1):822–833, 2013.

- [54] K Matsuzaki and C Horikiri. Interactions of amyloid beta-peptide (1-40) with ganglioside-containing membranes. *Biochemistry*, 38(13):4137–4142, 1999.
- [55] K Matsuzaki, K Kato, and K Yanagisawa. A beta polymerization through interaction with membrane gangliosides. *Biochim. Biophys. Acta Mol. Cell Biol. Lipids*, 1801(8):868–877, 2010.
- [56] Samuel A Kotler, Patrick Walsh, Jeffrey R Brender, and Ayyalusamy Ramamoorthy. Differences between amyloid- β aggregation in solution and on the membrane: insights into elucidation of the mechanistic details of Alzheimer’s disease. *Chemical Society reviews*, jan 2014.
- [57] Hyunbum Jang, Laura Connelly, Fernando Teran Arce, Srinivasan Ramachandran, Ratnesh Lal, Bruce L Kagan, and Ruth Nussinov. Alzheimer’s disease: which type of amyloid-preventing drug agents to employ? *Physical Chemistry Chemical Physics*, 15(23):8868, 2013.
- [58] Hyunbum Jang, Fernando Teran Arce, Srinivasan Ramachandran, Bruce L Kagan, Ratnesh Lal, and Ruth Nussinov. Disordered amyloidogenic peptides may insert into the membrane and assemble into common cyclic structural motifs. *Chemical Society reviews*, feb 2014.
- [59] T L Williams and L C Serpell. Membrane and surface interactions of Alzheimer’s A beta peptide - insights into the mechanism of cytotoxicity. *FEBS J.*, 278(20):3905–3917, 2011.
- [60] F T Arce, H Jang, L Connelly, S Ramachandran, B L Kagan, R Nussinov, and Ratnesh Lal. StructureFunction Studies of Amyloid Pores in Alzheimer’s Disease as a Case Example of Neurodegenerative Diseases. In Yuri Lyubchenko, editor, *Bio-nanoimaging: Protein Misfolding and Aggregation*, chapter 36, pages 397–408. Elsevier, 2014.
- [61] Kevin J Hallock, Dong-Kuk Lee, and A Ramamoorthy. MSI-78, an Analogue of the Magainin Antimicrobial Peptides, Disrupts Lipid Bilayer Structure via Positive Curvature Strain. *Biophysical Journal*, 84(5):3052–3060, may 2003.
- [62] Jeffrey R Brender, Deborah L Heyl, Shyamprasad Samisetti, Samuel A Kotler, Joshua M Osborne, Ranadheer R Pesaru, and Ayyalusamy Ramamoorthy. Membrane disordering is not sufficient for membrane permeabilization by islet amyloid polypeptide: studies of IAPP(20-29) fragments. *Physical Chemistry Chemical Physics*, 15(23):8908–8915, 2013.
- [63] M F M Sciacca, S A Kotler, J R Brender, J Chen, D K Lee, and A Ramamoorthy. Two-Step Mechanism of Membrane Disruption by A beta through Membrane Fragmentation and Pore Formation. *Biophys. J.*, 103(4):702–710, 2012.

- [64] M SoOderberg, C Edlund, I Alafuzoff, K Kristensson, and G Dallner. Lipid composition in different regions of the brain in alzheimer's disease/senile dementia of alzheimer's type. *Journal of neurochemistry*, 59(5):1646–1653, 1992.
- [65] Kimberly Wells, AkhlaqA. Farooqui, Leopold Liss, and LloydA. Horrocks. Neural membrane phospholipids in alzheimer disease. *Neurochemical Research*, 20(11):1329–1333, 1995.
- [66] Liza Nielsen, Ritu Khurana, Alisa Coats, Sven Frokjaer, Jens Brange, Sandip Vyas, Vladimir N. Uversky, and Anthony L. Fink. Effect of Environmental Factors on the Kinetics of Insulin Fibril Formation: Elucidation of the Molecular Mechanism. *Biochemistry*, 40(20):6036–6046, may 2001.
- [67] H. Jang, F. T. Arce, S. Ramachandran, R. Capone, R. Lal, and R. Nussinov. β -barrel topology of alzheimer's β -amyloid ion channels. *J. Mol. Biol.*, 404(5):917–934, 2010.
- [68] Carlos Bustamante, James Vesenka, Chun Lin Tang, William Rees, Martin Guthold, and Rebecca Keller. Circular dna molecules imaged in air by scanning force microscopy. *Biochemistry*, 31(1):22–26, 1992.
- [69] Muriel Arimon, Ismael Díez-Pérez, Marcelo J Kogan, Núria Durany, Ernest Giralt, Fausto Sanz, and Xavier Fernández-Busquets. Fine structure study of $\alpha\beta$ 1-42 fibrillogenesis with atomic force microscopy. *The FASEB journal*, 19(10):1344–1346, 2005.
- [70] Jeffrey L Hutter and John Bechhoefer. Calibration of atomic-force microscope tips. *Review of Scientific Instruments*, 64(7):1868–1873, 1993.
- [71] H Ti Tien, S Carbone, and EA Dawidowicz. Formation of black lipid membranes by oxidation products of cholesterol. *Nature*, 212(5063):718–719, 1966.
- [72] P. Mueller, D. O. Rudin, H. T. Tien, and W. C. Wescott. Reconstitution of cell membrane structure in vitro and its transformation into an excitable system. *Nature*, 194(4832):979–980, 1962.
- [73] Dagmar Schlenzig, Susanne Manhart, Yeliz Cinar, Martin Kleinschmidt, Gerd Hause, Dieter Willbold, Susanne Aileen Funke, Stephan Schilling, and Hans-Ulrich Demuth. Pyroglutamate formation influences solubility and amyloidogenicity of amyloid peptides. *Biochemistry*, 48(29):7072–8, jul 2009.
- [74] Phillip M Pifer, Elizabeth a Yates, and Justin Legleiter. Point mutations in $A\beta$ result in the formation of distinct polymorphic aggregates in the presence of lipid bilayers. *PloS one*, 6(1):e16248, jan 2011.
- [75] C M Yip, A A Darabie, and J McLaurin. A beta 42-peptide assembly on lipid Bilayers. *J Mol Biol*, 318(1):97–107, 2002.

- [76] C M Yip, E A Elton, A A Darabie, M R Morrison, and J McLaurin. Cholesterol, a modulator of membrane-associated A beta-fibrillogenesis and neurotoxicity. *J Mol Biol*, 311(4):723–734, 2001.
- [77] C M Yip and J McLaurin. Amyloid-beta peptide assembly: a critical step in fibrillogenesis and membrane disruption. *Biophysical Journal*, 80(3):1359–1371, mar 2001.
- [78] T L Williams, B R G Johnson, B Urbanc, A T A Jenkins, S D A Connell, and L C Serpell. A beta 42 oligomers, but not fibrils, simultaneously bind to and cause damage to ganglioside-containing lipid membranes. *Biochem. J.*, 439:67–77, 2011.
- [79] Alan L Gillman, Hyunbum Jang, Joon Lee, Srinivasan Ramachandran, Bruce L Kagan, Ruth Nussinov, and Fernando Teran Arce. Activity and Architecture of Pyroglutamate-Modified Amyloid- β (A β pE3-42) Pores. *The Journal of Physical Chemistry B*, 118(26):7335–7344, jun 2014.
- [80] L Tosatto, A O Andrichetti, N Plotegher, V Antonini, I Tessari, L Ricci, L Bubacco, and M D Serra. Alpha-synuclein pore forming activity upon membrane association. *Biochim. Biophys. Acta-Biomembr.*, 1818(11):2876–2883, 2012.
- [81] MSP Sansom. Structure and function of channel-forming peptaibols. *Quarterly reviews of biophysics*, 26(04):365–421, 1993.
- [82] I Cherny and E Gazit. Amyloids: Not only pathological agents but also ordered nanomaterials. *Angew. Chem. Int. Ed.*, 47(22):4062–4069, 2008.
- [83] Yuta Suzuki, Jeffrey R Brender, Molly T Soper, Janarthanan Krishnamoorthy, Yunlong Zhou, Brandon T Ruotolo, Nicholas A Kotov, Ayyalusamy Ramamoorthy, and E Neil G Marsh. Resolution of Oligomeric Species during the Aggregation of A β 140 Using 19F NMR. *Biochemistry*, 52(11):1903–1912, feb 2013.
- [84] Subramanian Vivekanandan, Jeffrey R Brender, Shirley Y Lee, and Ayyalusamy Ramamoorthy. A partially folded structure of amyloid-beta(1-40) in an aqueous environment. *Biochemical and biophysical research communications*, 411(2):312–316, jul 2011.
- [85] Rakez Kaye, Anna Pensalfini, Larry Margol, Yuri Sokolov, Floyd Sarsoza, Elizabeth Head, James Hall, and Charles Glabe. Annular protofibrils are a structurally and functionally distinct type of amyloid oligomer. *Journal of Biological Chemistry*, 284(7):4230–4237, 2009.
- [86] M. Bucciantini, E. Giannoni, F. Chiti, F. Baroni, L. Formigli, J. S. Zurdo, N. Taddei, G. Ramponi, C. M. Dobson, and M. Stefani. Inherent toxicity of aggregates implies a common mechanism for protein misfolding diseases. *Nature*, 416(6880):507–511, 2002.

- [87] Kelly A Conway, Seung-Jae J Lee, Jean-christophe C Rochet, Tomas T Ding, Robin E Williamson, and Peter T Lansbury. Acceleration of oligomerization, not fibrillization, is a shared property of both α -synuclein mutations linked to early-onset Parkinson's disease: Implications for pathogenesis and therapy. *Proceedings of the National Academy of Sciences*, 97(2):571–576, jan 2000.
- [88] Juliette Janson, Richard H Ashley, David Harrison, Susan McIntyre, and Peter C Butler. The mechanism of islet amyloid polypeptide toxicity is membrane disruption by intermediate-sized toxic amyloid particles. *Diabetes*, 48(3):491–498, 1999.
- [89] N Arispe, E Rojas, and H B Pollard. Alzheimer disease amyloid β protein forms calcium channels in bilayer membranes: Blockade by tromethamine and aluminum. *Proc. Natl. Acad. Sci. U.S.A.*, 90(2):567–571, 1993.
- [90] Laura Connelly, Hyunbum Jang, Fernando Teran Arce, Srinivasan Ramachandran, Bruce L Kagan, Ruth Nussinov, Ratnesh Lal, F T Arce, Srinivasan Ramachandran, Bruce L Kagan, Ruth Nussinov, and Ratnesh Lal. Effects of Point Substitutions on the Structure of Toxic Alzheimer's β -Amyloid Channels: Atomic Force Microscopy and Molecular Dynamics Simulations. *Biochemistry*, 51(14):3031–3038, mar 2012.
- [91] Hyunbum Jang, Fernando Teran Arce, Srinivasan Ramachandran, Ricardo Capone, Rushana Azimova, Bruce L Kagan, Ruth Nussinov, and Ratnesh Lal. Truncated beta-amyloid peptide channels provide an alternative mechanism for Alzheimer's Disease and Down syndrome. *Proceedings of the National Academy of Sciences of the United States of America*, 107(14):6538–6543, apr 2010.
- [92] M Mustata, R Capone, H Jang, F T Arce, S Ramachandran, R Lal, and R Nussinov. K3 Fragment of Amyloidogenic beta(2)-Microglobulin Forms Ion Channels: Implication for Dialysis Related Amyloidosis. *J. Am. Chem. Soc.*, 131(41):14938–14945, 2009.
- [93] Philippe Brûlet and Harden M McConnell. Lateral hapten mobility and immunochemistry of model membranes. *Proceedings of the National Academy of Sciences*, 73(9):2977–2981, 1976.
- [94] Fitzroy J Byfield, Helim Aranda-Espinoza, Victor G Romanenko, George H Rothblat, and Irena Levitan. Cholesterol depletion increases membrane stiffness of aortic endothelial cells. *Biophysical journal*, 87(5):3336–3343, 2004.
- [95] R A. Demel and B De Kruffyff. The function of sterols in membranes. *Biochimica et Biophysica Acta (BBA)-Reviews on Biomembranes*, 457(2):109–132, 1976.
- [96] Evan Evans and David Needham. Physical properties of surfactant bilayer membranes: thermal transitions, elasticity, rigidity, cohesion and colloidal interactions. *Journal of Physical Chemistry*, 91(16):4219–4228, 1987.
- [97] David Needham and Rashmi S Nunn. Elastic deformation and failure of lipid bilayer membranes containing cholesterol. *Biophysical journal*, 58(4):997–1009, 1990.

- [98] Lorena Redondo-Morata, Marina I Giannotti, and Fausto Sanz. Influence of cholesterol on the phase transition of lipid bilayers: a temperature-controlled force spectroscopy study. *Langmuir*, 28(35):12851–12860, 2012.
- [99] Gerald W Stockton and Ian CP Smith. A deuterium nuclear magnetic resonance study of the condensing effect of cholesterol on egg phosphatidylcholine bilayer membranes. i. perdeuterated fatty acid probes. *Chemistry and physics of lipids*, 17(2-3):251–263, 1976.
- [100] Xiaolian Xu and Erwin London. The effect of sterol structure on membrane lipid domains reveals how cholesterol can induce lipid domain formation. *Biochemistry*, 39(5):843–849, 2000.
- [101] C Canale, S Seghezza, S Vilasi, R Carrotta, D Bulone, A Diaspro, P L S Biagio, and S Dante. Different effects of Alzheimer’s peptide A beta(1-40) oligomers and fibrils on supported lipid membranes. *Biophys. Chem.*, 182:23–29, 2013.
- [102] Silvia Dante, T Hauss, Roland Steitz, Claudio Canale, Norbert A Dencher, Thomas Hauß, Roland Steitz, Claudio Canale, and Norbert A Dencher. Nanoscale structural and mechanical effects of beta-amyloid (142) on polymer cushioned membranes: A combined study by neutron reflectometry and AFM Force Spectroscopy. *Biochimica et Biophysica Acta (BBA) - Biomembranes*, 1808(11):2646–2655, nov 2011.
- [103] Fei Liu, Fernando Terán Arce, Srinivasan Ramachandran, and Ratnesh Lal. Nanomechanics of Hemichannel Conformations: CONNEXIN FLEXIBILITY UNDERLYING CHANNEL OPENING AND CLOSING. *Journal of Biological Chemistry*, 281(32):23207–23217, aug 2006.
- [104] C L Masters, G Simms, N A Weinman, G Multhaup, B L McDonald, and K Beyreuther. Amyloid plaque core protein in Alzheimer disease and Down syndrome. *Proc Natl Acad Sci USA*, 82:4245–4249, 1985.
- [105] Yifat Miller, Buyong Ma, and Ruth Nussinov. Polymorphism of Alzheimer’s A β 17-42 (p3) Oligomers: The Importance of the Turn Location and Its Conformation. *Biophysical Journal*, 97(4):1168–1177, aug 2009.
- [106] H. Jang, F. Teran Arce, S. Ramachandran, R. Capone, R. Lal, and R. Nussinov. Structural convergence among diverse, toxic beta-sheet ion channels. *J Phys Chem B*, 114(29):9445–51, 2010.
- [107] Cristian A Lasagna-Reeves, Charles G Glabe, and Rakez Kaye. Amyloid- β annular protofibrils evade fibrillar fate in Alzheimer disease brain. *The Journal of biological chemistry*, 286(25):22122–30, jun 2011.
- [108] R Bhatia, H Lin, and R Lal. Fresh and globular amyloid beta protein (1-42) induces rapid cellular degeneration: evidence for AbetaP channel-mediated cellular toxicity. *FASEB journal : official publication of the Federation of American Societies for Experimental Biology*, 14(9):1233–43, jun 2000.

- [109] Ilya Bezprozvanny and Mark P Mattson. Neuronal calcium mishandling and the pathogenesis of Alzheimer's disease. *Trends in neurosciences*, 31(9):454–63, sep 2008.
- [110] Masahiro Kawahara and Yoichiro Kuroda. Intracellular Calcium Changes in Neuronal Cells Induced by Alzheimer's β -Amyloid Protein Are Blocked by Estradiol and Cholesterol. *Cellular and Molecular Neurobiology*, 21(1):1–13, 2001.
- [111] Angelo Demuro, Martin Smith, and Ian Parker. Single-channel Ca(2+) imaging implicates A β 1-42 amyloid pores in Alzheimer's disease pathology. *The Journal of cell biology*, 195(3):515–24, oct 2011.
- [112] Wanli Wei. A β 17-42 in Alzheimer's disease activates JNK and caspase-8 leading to neuronal apoptosis. *Brain*, 125(9):2036–2043, sep 2002.
- [113] Coralie Di Scala, Jean-Denis Troadec, Clément Lelièvre, Nicolas Garmy, Jacques Fantini, and Henri Chahinian. Mechanism of cholesterol-assisted oligomeric channel formation by a short Alzheimer β -amyloid peptide. *Journal of neurochemistry*, 128(1):186–95, jan 2014.
- [114] Daniel M Czajkowsky, Sitong Sheng, and Zhifeng Shao. Staphylococcal α -hemolysin can form hexamers in phospholipid bilayers¹. *Journal of Molecular Biology*, 276(2):325–330, feb 1998.
- [115] Joon Lee, Alan L Gillman, Hyunbum Jang, Srinivasan Ramachandran, Bruce L Kagan, Ruth Nussinov, and Fernando Teran Arce. Role of the Fast Kinetics of Pyroglutamate-Modified Amyloid- β Oligomers in Membrane Binding and Membrane Permeability. *Biochemistry*, 53(28):4704–4714, jun 2014.
- [116] N Arispe, H B Pollard, and E Rojas. Zn²⁺ interaction with Alzheimer amyloid beta protein calcium channels. *Proceedings of the National Academy of Sciences*, 93(4):1710–1715, feb 1996.
- [117] Yutaka Hirakura, Meng-Chin Lin, and Bruce L Kagan. Alzheimer amyloid a β 142 channels: Effects of solvent, pH, and congo red. *Journal of Neuroscience Research*, 57(4):458–466, aug 1999.
- [118] Lakshini H. S. Mendis, Angus C. Grey, Richard L. M. Faull, and Maurice A. Curtis. Hippocampal lipid differences in Alzheimer's disease: a human brain study using matrix-assisted laser desorption/ionization-imaging mass spectrometry. *Brain and Behavior*, (February):e00517, jul 2016.
- [119] Juan Marcos Alarcón, Julio A Brito, Tamara Hermosilla, Illani Atwater, David Mears, and Eduardo Rojas. Ion channel formation by Alzheimer's disease amyloid β -peptide (A β 40) in unilamellar liposomes is determined by anionic phospholipids. *Peptides*, 27(1):95–104, jan 2006.

- [120] Daniela Meleleo, Angela Galliani, and Gabriella Notarachille. A β P1-42 incorporation and channel formation in planar lipid membranes: the role of cholesterol and its oxidation products. *Journal of Bioenergetics and Biomembranes*, 45(4):369–381, aug 2013.
- [121] Marc-Antoine Sani, John D Gehman, and Frances Separovic. Lipid matrix plays a role in Abeta fibril kinetics and morphology. *FEBS letters*, 585(5):749–54, mar 2011.
- [122] Harry LeVine III. Quantification of β -sheet amyloid fibril structures with thioflavin T. In Ronald Wetzel B T *Methods in Enzymology*, editor, *Amyloid, Prions, and Other Protein Aggregates*, volume Volume 309, pages 274–284. Academic Press, 1999.
- [123] Matthew Biancalana and Shohei Koide. Molecular mechanism of Thioflavin-T binding to amyloid fibrils. *Biochimica et biophysica acta*, 1804(7):1405–12, jul 2010.
- [124] A Lomakin, D S Chung, G B Benedek, D A Kirschner, and D B Teplow. On the nucleation and growth of amyloid beta-protein fibrils: detection of nuclei and quantitation of rate constants. *Proceedings of the National Academy of Sciences of the United States of America*, 93(3):1125–1129, feb 1996.
- [125] Toshinori Shimanouchi, Ryo Onishi, Nachi Kitaura, Hiroshi Umakoshi, and Ryoichi Kuboi. Copper-mediated growth of amyloid β fibrils in the presence of oxidized and negatively charged liposomes. *Journal of Bioscience and Bioengineering*, 112(6):611–615, dec 2011.
- [126] Ashok Parbhu, Hai Lin, Julian Thimm, and Ratneshwar Lal. Imaging real-time aggregation of amyloid beta protein (142) by atomic force microscopy. *Peptides*, 23(7):1265–1270, jul 2002.
- [127] H Jang, F Teran Arce, S Ramachandran, B L Kagan, R Lal, and R Nussinov. Familial Alzheimer’s disease Osaka mutant (DeltaE22) beta-barrels suggest an explanation for the different Abeta1-40/42 preferred conformational states observed by experiment. *J Phys Chem B*, 117(39):11518–11529, 2013.
- [128] Ricardo Capone, Hyunbum Jang, Samuel a. Kotler, Bruce L. Kagan, Ruth Nussinov, and Ratnesh Lal. Probing Structural Features of Alzheimer’s Amyloid- β Pores in Bilayers Using Site-Specific Amino Acid Substitutions. *Biochemistry*, 51(3):776–785, jan 2012.
- [129] Hyunbum Jang, Fernando Teran Arce, Ricardo Capone, Srinivasan Ramachandran, Ratnesh Lal, and Ruth Nussinov. Misfolded Amyloid Ion Channels Present Mobile β -Sheet Subunits in Contrast to Conventional Ion Channels. *Biophysical Journal*, 97(11):3029–3037, dec 2009.
- [130] George Lee, Harvey B Pollard, and Nelson Arispe. Annexin 5 and apolipoprotein E2 protect against Alzheimer’s amyloid- β -peptide cytotoxicity by competitive inhibition at a common phosphatidylserine interaction site. *Peptides*, 23(7):1249–1263, jul 2002.

- [131] Nelson Arispe, Juan C Diaz, and Olga Simakova. A β ion channels. Prospects for treating Alzheimer's disease with A β channel blockers. *Biochimica et Biophysica Acta (BBA) - Biomembranes*, 1768(8):1952–1965, aug 2007.
- [132] Nelson ARISPE. Plasma membrane cholesterol controls the cytotoxicity of Alzheimer's disease AbetaP (1-40) and (1-42) peptides. *The FASEB Journal*, 16(12):1526–1536, oct 2002.
- [133] Ricardo Capone, Steven Blake, Marcela Rincon Restrepo, Jerry Yang, and Michael Mayer. Designing Nanosensors Based on Charged Derivatives of Gramicidin A. *Journal of the American Chemical Society*, 129(31):9737–9745, aug 2007.
- [134] L. L. Iversen, R. J. Mortishire-Smith, S. J. Pollack, and M. S. Shearman. The toxicity in vitro of beta-amyloid protein., Oct 1995.
- [135] R. E. Tanzi and L. Bertram. Twenty years of the alzheimer's disease amyloid hypothesis: A genetic perspective. *Cell*, 120(4):545–555, 2005.
- [136] R. Jakob-Roetne and H. Jacobsen. Alzheimer's disease: From pathology to therapeutic approaches. *Angew. Chem. Int. Ed.*, 48(17):3030–3059, 2009.
- [137] Christian Haass and Dennis J Selkoe. Soluble protein oligomers in neurodegeneration: lessons from the alzheimer's amyloid β -peptide. *Nature reviews Molecular cell biology*, 8(2):101–112, 2007.
- [138] Jeff Sevigny, Joyce Suhy, Ping Chiao, Tianle Chen, Gregory Klein, Derk Purcell, Joonmi Oh, Ajay Verma, Mehul Sampat, and Jerome Barakos. Amyloid pet screening for enrichment of early-stage alzheimer disease clinical trials: experience in a phase 1b clinical trial. *Alzheimer Disease & Associated Disorders*, 30(1):1–7, 2016.
- [139] Joanna L Jankowsky, Hilda H Slunt, Tamara Ratovitski, Nancy A Jenkins, Neal G Copeland, and David R Borchelt. Co-expression of multiple transgenes in mouse cns: a comparison of strategies. *Biomolecular Engineering*, 17(6):157 – 165, 2001.
- [140] R. Lalonde, H.D. Kim, J.A. Maxwell, and K. Fukuchi. Exploratory activity and spatial learning in 12-month-old app695swe/co + ps1/e9 mice with amyloid plaques. *Neuroscience Letters*, 390(2):87 – 92, 2005.
- [141] R. S. Reiserer, F. E. Harrison, D. C. Syverud, and M. P. McDonald. Impaired spatial learning in the appswe+psen1e9 bigenic mouse model of alzheimers disease. *Genes, Brain and Behavior*, 6(1):54–65, 2007.
- [142] Joanna L. Jankowsky, Daniel J. Fadale, Jeffrey Anderson, Guilian M. Xu, Victoria Gonzales, Nancy A. Jenkins, Neal G. Copeland, Michael K. Lee, Linda H. Younkin, Steven L. Wagner, Steven G. Younkin, and David R. Borchelt. Mutant presenilins specifically elevate the levels of the 42 residue -amyloid peptide in vivo: evidence for augmentation of a 42-specific secretase. *Human Molecular Genetics*, 13(2):159, 2004.

- [143] Richard Morris. Developments of a water-maze procedure for studying spatial learning in the rat. *Journal of Neuroscience Methods*, 11(1):47 – 60, 1984.
- [144] Andre Fischer. Epigenetic memory: the lamarckian brain. *The EMBO Journal*, 2014.
- [145] Eva Benito and Angel Barco. The neuronal activity-driven transcriptome. *Molecular Neurobiology*, 51(3):1071–1088, 2015.
- [146] Mar Matarin, DervisA. Salih, Marina Yasvoina, DamianM. Cummings, Sebastian Guelfi, Wenfei Liu, MuzammilA. NahabooSolim, ThomasG. Moens, RocioMoreno Paublete, ShabinahS. Ali, Marina Perona, Roshni Desai, KennethJ. Smith, Judy Latcham, Michael Fulleylove, JillC. Richardson, John Hardy, and FrancesA. Edwards. A genome-wide gene-expression analysis and database in transgenic mice during development of amyloid or tau pathology. *Cell Reports*, 10(4):633 – 644, 2015.
- [147] Jens Wagner, Sergey Ryazanov, Andrei Leonov, Johannes Levin, Song Shi, Felix Schmidt, Catharina Prix, Francisco Pan-Montojo, Uwe Bertsch, Gerda Mitteregger-Kretschmar, Markus Geissen, Martin Eiden, Fabienne Leidel, Thomas Hirschberger, Andreas A. Deeg, Julian J. Krauth, Wolfgang Zinth, Paul Tavan, Jens Pilger, Markus Zweckstetter, Tobias Frank, Mathias Bähr, Jochen H. Weishaupt, Manfred Uhr, Henning Urlaub, Ulrike Teichmann, Matthias Samwer, Kai Bötzel, Martin Groschup, Hans Kretschmar, Christian Griesinger, and Armin Giese. Anle138b: a novel oligomer modulator for disease-modifying therapy of neurodegenerative diseases such as prion and parkinson’s disease. *Acta Neuropathologica*, 125(6):795–813, 2013.
- [148] Jens Wagner, Sybille Krauss, Song Shi, Sergey Ryazanov, Julia Steffen, Carolin Miklitz, Andrei Leonov, Alexander Kleinknecht, Bettina Göricke, Jochen H. Weishaupt, Daniel Weckbecker, Anne M. Reiner, Wolfgang Zinth, Johannes Levin, Dan Ehninger, Stefan Remy, Hans A. Kretschmar, Christian Griesinger, Armin Giese, and Martin Fuhrmann. Reducing tau aggregates with anle138b delays disease progression in a mouse model of tauopathies. *Acta Neuropathologica*, 130(5):619–631, 2015.
- [149] Markus P. Kummer, Thea Hammerschmidt, Ana Martinez, Dick Terwel, Gregor Eichele, Anika Witten, Stefanie Figura, Monika Stoll, Stephanie Schwartz, Hans-Christian Pape, Joachim L. Schultze, David Weinshenker, and Michael T. Heneka. Ear2 deletion causes early memory and learning deficits in app/ps1 mice. *Journal of Neuroscience*, 34(26):8845–8854, 2014.
- [150] Dennis J Selkoe and John Hardy. The amyloid hypothesis of alzheimer’s disease at 25 years. *EMBO Molecular Medicine*, 8(6):595–608, 2016.
- [151] Eva Benito, Hendrik Urbanke, Binu Ramachandran, Jonas Barth, Rashi Halder, Ankit Awasthi, Gaurav Jain, Vincenzo Capece, Susanne Burkhardt, Magdalena Navarro-Sala, Sankari Nagarajan, Anna-Lena Schtz, Steven A. Johnsen, Stefan Bonn, Reinhardt Lhrmann, Camin Dean, and Andr Fischer. Hdac inhibitordependent

- transcriptome and memory reinstatement in cognitive decline models. *The Journal of Clinical Investigation*, 125(9):3572–3584, 9 2015.
- [152] Riqiang Yan and Robert Vassar. Targeting the β secretase BACE1 for Alzheimer's disease therapy. *Lancet neurology*, 13(3):319–329, mar 2014.
- [153] Andrew J Doig and Philippe Derreumaux. Inhibition of protein aggregation and amyloid formation by small molecules. *Current Opinion in Structural Biology*, 30:50–56, 2015. Folding and binding/Nucleic acids and their protein complexes.
- [154] Dagmar E Ehrnhoefer, Jan Bieschke, Annett Boeddrich, Martin Herbst, Laura Masino, Rudi Lurz, Sabine Engemann, Annalisa Pastore, and Erich E Wanker. Egcg redirects amyloidogenic polypeptides into unstructured, off-pathway oligomers. *Nature structural & molecular biology*, 15(6):558–566, 2008.
- [155] Jan Bieschke, Jenny Russ, Ralf P. Friedrich, Dagmar E. Ehrnhoefer, Heike Wobst, Katja Neugebauer, and Erich E. Wanker. Egcg remodels mature α -synuclein and amyloid- fibrils and reduces cellular toxicity. *Proceedings of the National Academy of Sciences*, 107(17):7710–7715, 2010.
- [156] Xiu-Lian Wang, Ji Zeng, Jin Feng, Yi-Tao Tian, Yu-Jian Liu, Mei Qiu, Xiong Yan, Yang Yang, Yan Xiong, Zhi-Hua Zhang, Qun Wang, Jian-Zhi Wang, and Rong Liu. Helicobacter pylori filtrate impairs spatial learning and memory in rats and increases α -amyloid by enhancing expression of presenilin-2. *Frontiers in Aging Neuroscience*, 6:66, 2014.
- [157] Ganesh M Shankar, Brenda L Bloodgood, Matthew Townsend, Dominic M Walsh, Dennis J Selkoe, and Bernardo L Sabatini. Natural oligomers of the alzheimer amyloid- β protein induce reversible synapse loss by modulating an nmda-type glutamate receptor-dependent signaling pathway. *Journal of Neuroscience*, 27(11):2866–2875, 2007.
- [158] Yun Wang, Hongwei Zhou, Amey Barakat, and Henry Querfurth. Differential effects of beta-amyloid on synaptic connectivity in pfc. *Alzheimer's & Dementia*, 6(4):S408–S409, 2010.
- [159] Juan Carlos Diaz, Olga Simakova, Kenneth A Jacobson, Nelson Arispe, and Harvey B Pollard. Small molecule blockers of the alzheimer $\alpha\beta$ calcium channel potentially protect neurons from $\alpha\beta$ cytotoxicity. *Proceedings of the National Academy of Sciences*, 106(9):3348–3353, 2009.
- [160] Rasmus Linser, Riddhiman Sarkar, Alexey Krushelnitzky, Andi Mainz, and Bernd Reif. Dynamics in the solid-state: perspectives for the investigation of amyloid aggregates, membrane proteins and soluble protein complexes. *Journal of biomolecular NMR*, 59(1):1–14, 2014.

- [161] Alexander Dobin, Carrie A. Davis, Felix Schlesinger, Jorg Drenkow, Chris Zaleski, Sonali Jha, Philippe Batut, Mark Chaisson, and Thomas R. Gingeras. Star: ultrafast universal rna-seq aligner, Jan 2013.
- [162] Michael I. Love, Wolfgang Huber, and Simon Anders. Moderated estimation of fold change and dispersion for rna-seq data with *deseq2*. *Genome Biology*, 15(12):550, 2014.
- [163] Roland Guntern, Constantin Bouras, PR Hof, and PG Vallet. An improved thioflavine s method for staining neurofibrillary tangles and senile plaques in alzheimer’s disease. *Cellular and Molecular Life Sciences*, 48(1):8–10, 1992.
- [164] Anyang Sun, Xuan V Nguyen, and Guoying Bing. Comparative analysis of an improved thioflavin-s stain, gallyas silver stain, and immunohistochemistry for neurofibrillary tangle demonstration on the same sections. *Journal of Histochemistry & Cytochemistry*, 50(4):463–472, 2002.
- [165] Stephen H. White. Analysis of the torus surrounding planar lipid bilayer membranes. *Biophysical Journal*, 12(4):432–445, 1972.
- [166] J. Zlatanova, S. M. Lindsay, and S. H. Leuba. Single molecule force spectroscopy in biology using the atomic force microscope. *Progress in Biophysics and Molecular biology*, 74(1-2):37–61, 2000.
- [167] Keir C. Neuman and Attila Nagy. Single-molecule force spectroscopy: optical tweezers, magnetic tweezers and atomic force microscopy. *Nature Methods*, 5(6):491–505, 2008.
- [168] H. Clausen-Schaumann, M. Rief, C. Tolksdorf, and H. E. Gaub. Mechanical stability of single dna molecules. *Biophysical Journal*, 78(4):1997–2007, 2000.
- [169] T. T. Perkins. Optical traps for single molecule biophysics: a primer. *Laser Photonics Reviews*, 3(1-2):203–220, 2009.
- [170] Jeffrey R. Moffitt, Yann R. Chemla, Steven B. Smith, and Carlos Bustamante. Recent advances in optical tweezers. *Annual Review of Biochemistry*, 77:205–228, 2008.
- [171] T. R. Strick, J. F. Allemand, D. Bensimon, A. Bensimon, and V. Croquette. The elasticity of a single supercoiled dna molecule. *Science*, 271(5257):1835–1837, 1996.
- [172] M. D. Wang, M. J. Schnitzer, H. Yin, R. Landick, J. Gelles, and S. M. Block. Force and velocity measured for single molecules of rna polymerase. *Science*, 282(5390):902–907, 1998.
- [173] Donald J. Sirbuly, Raymond W. Friddle, Joshua Villanueva, and Qian Huang. Nanomechanical force transducers for biomolecular and intracellular measurements: is there room to shrink and why do it? *Reports on Progress in Physics*, 78(2):024101, 2015.

- [174] Charles R. Hickenboth, Jeffrey S. Moore, Scott R. White, Nancy R. Sottos, Jerome Baudry, and Scott R. Wilson. Biasing reaction pathways with mechanical force. *Nature*, 446(7134):423–427, 2007.
- [175] Charina L. Choi, Kristie J. Koski, Andrew C. K. Olson, and A. Paul Alivisatos. Luminescent nanocrystal stress gauge. *Proceedings of the National Academy of Sciences of the United States of America*, 107(50):21306–21310, 2010.
- [176] Carsten Grashoff, Brenton D. Hoffman, Michael D. Brenner, Ruobo Zhou, Maddy Parsons, Michael T. Yang, Mark A. McLean, Stephen G. Sligar, Christopher S. Chen, Taekjip Ha, and Martin A. Schwartz. Measuring mechanical tension across vinculin reveals regulation of focal adhesion dynamics. *Nature*, 466(7303):263–267, 2010.
- [177] Fanjie Meng, Thomas M. Suchyna, and Frederick Sachs. A fluorescence energy transfer-based mechanical stress sensor for specific proteins in situ. *Febs Journal*, 275(12):3072–3087, 2008.
- [178] T. Iio, S. Takahashi, and S. Sawada. Fluorescent molecular rotor binding to actin. *Journal of Biochemistry*, 113(2):196–199, 1993.
- [179] C. E. Kung and J. K. Reed. Microviscosity measurements of phospholipid-bilayers using fluorescent dyes that undergo torsional relaxation. *Biochemistry*, 25(20):6114–6121, 1986.
- [180] Marina K. Kuimova, Stanley W. Botchway, Anthony W. Parker, Milan Balaz, Hazel A. Collins, Harry L. Anderson, Klaus Suhling, and Peter R. Ogilby. Imaging intracellular viscosity of a single cell during photoinduced cell death. *Nature Chemistry*, 1(1):69–73, 2009.
- [181] M. Law, D. J. Sirbuly, J. C. Johnson, J. Goldberger, R. J. Saykally, and P. D. Yang. Nanoribbon waveguides for subwavelength photonics integration. *Science*, 305(5688):1269–1273, 2004.
- [182] Ilsun Yoon, Sarah E. Baker, Kanguk Kim, Nicholas O. Fischer, Daniel Heineck, Yinmin Wang, Sadik C. Esener, and Donald J. Sirbuly. Nanofiber near-field light-matter interactions for enhanced detection of molecular level displacements and dynamics. *Nano Letters*, 13(4):1440–1445, 2013.
- [183] F. Gittes and C. F. Schmidt. Thermal noise limitations on micromechanical experiments. *European Biophysics Journal with Biophysics Letters*, 27(1):75–81, 1998.
- [184] L. L. Liu, S. Kheifets, V. Gini, and F. Capasso. Subfemtonewton force spectroscopy at the thermal limit in liquids. *Physical Review Letters*, 116(22):228001, 2016.
- [185] Q. Huang, F. T. Arce, J. Lee, I. Yoon, J. Villanueva, R. Lal, and D. J. Sirbuly. Gap controlled plasmon-dielectric coupling effects investigated with single nanoparticle-terminated atomic force microscope probes. *Nanoscale*, 8(39):17102–17107, 2016.

- [186] B. Bhushan. Nanotribology, nanomechanics and nanomaterials characterization. *Philosophical Transactions of the Royal Society a-Mathematical Physical and Engineering Sciences*, 366(1869):1351–1381, 2008.
- [187] P. G. Degennes. Polymers at an interface - a simplified view. *Advances in Colloid and Interface Science*, 27(3-4):189–209, 1987.
- [188] S. R. Kirchner, S. Nedev, S. Carretero-Palacios, A. Mader, M. Opitz, T. Lohmuller, and J. Feldmann. Direct optical monitoring of flow generated by bacterial flagellar rotation. *Applied Physics Letters*, 104(9):093701, 2014.
- [189] S. Chattopadhyay, R. Moldovan, C. Yeung, and X. L. Wu. Swimming efficiency of bacterium escherichia coli. *Proceedings of the National Academy of Sciences of the United States of America*, 103(37):13712–13717, 2006.
- [190] F. Gittes and C. F. Schmidt. Signals and noise in micromechanical measurements. *Methods in Cell Biology*, 55:129–156, 1998.
- [191] Alexander Ohlinger, Andras Deak, Andrey A. Lutich, and Jochen Feldmann. Optically trapped gold nanoparticle enables listening at the microscale. *Physical Review Letters*, 108(1), 2012.
- [192] S. G. Shroff, D. R. Saner, and R. Lal. Dynamic micromechanical properties of cultured rat atrial myocytes measured by atomic-force microscopy. *American Journal of Physiology-Cell Physiology*, 269(1):C286–C292, 1995.
- [193] A. E. Pelling, S. Sehati, E. B. Gralla, J. S. Valentine, and J. K. Gimzewski. Local nanomechanical motion of the cell wall of saccharomyces cerevisiae. *Science*, 305(5687):1147–1150, 2004.
- [194] Hans-Jürgen Butt, Michael Kappl, Henning Mueller, Roberto Raiteri, Wolfgang Meyer, and Jürgen Rühle. Steric forces measured with the atomic force microscope at various temperatures. *Langmuir*, 15(7):2559–2565, 1999.
- [195] Marygorret Obonyo, Mojgan Sabet, Sheri P Cole, Joerg Ebmeyer, Satoshi Uematsu, Shizuo Akira, and Donald G Guiney. Deficiencies of myeloid differentiation factor 88, toll-like receptor 2 (tlr2), or tlr4 produce specific defects in macrophage cytokine secretion induced by helicobacter pylori. *Infection and immunity*, 75(5):2408–2414, 2007.
- [196] Weijuan Song, Yalong Wang, Liyan Zhang, Shengnan Fu, Ying Zeng, and Haiyan Hu. Preparation and evaluation of polysaccharide sulfates for inhibiting helicobacter pylori adhesion. *Carbohydrate polymers*, 103:398–404, 2014.
- [197] N. Tsutsui, I. Taneike, T. Ohara, S. Goshi, S. Kojio, N. Iwakura, H. Matsumaru, N. Wakisaka-Saito, H. M. Zhang, and T. Yamamoto. A novel action of the proton pump inhibitor rabeprazole and its thioether derivative against the motility of

- helicobacter pylori. *Antimicrobial Agents and Chemotherapy*, 44(11):3069–3073, 2000.
- [198] Y. Magariyama, S. Sugiyama, and S. Kudo. Bacterial swimming speed and rotation rate of bundled flagella. *Fems Microbiology Letters*, 199(1):125–129, 2001.
- [199] Warren Clarence Young and Richard Gordon Budynas. *Roark's formulas for stress and strain*, volume 7. McGraw-Hill New York, 2002.
- [200] FP Beer, ER Johnston, and J DeWolf. *Mechanics of Materials, 2009*. 2009.
- [201] Michael S Howe. *Hydrodynamics and sound*. Cambridge University Press, 2006.
- [202] Xuanyi Ma, Xin Qu, Wei Zhu, Yi-Shuan Li, Suli Yuan, Hong Zhang, Justin Liu, Pengrui Wang, Cheuk Sun Edwin Lai, Fabian Zanella, Gen-Sheng Feng, Farah Sheikhe, Shu Chiena, and Shaochen Chen. Deterministically patterned biomimetic human ipsc-derived hepatic model via rapid 3d bioprinting. *Proceedings of the National Academy of Sciences*, 113(8):2206–2211, 2016.
- [203] Benjamin D Fairbanks, Michael P Schwartz, Christopher N Bowman, and Kristi S Anseth. Photoinitiated polymerization of peg-diacrylate with lithium phenyl-2, 4, 6-trimethylbenzoylphosphinate: polymerization rate and cytocompatibility. *Biomaterials*, 30(35):6702–6707, 2009.